ABSTRACT

Title of Dissertation: **DEVELOPMENT OF MOIRÉ INTERFEROMETRY FOR REAL-TIME OBSERVATION OF NONLINEAR THERMAL DEFORMATIONS OF SOLDER AND SOLDER ASSEMBLY**

Seungmin Cho, Doctor of Philosophy, 2005

Dissertation Directed By: **Associate Professor Bongtae Han, Department of Mechanical Engineering**

An experimental apparatus using moiré interferometry is developed to characterize the thermo-mechanical behavior of solder joints. A compact moiré interferometer is combined with an environmental chamber to allow real-time observation of non-linear and time-dependent solder and solder assemblies.

The first apparatus is based on convection heating and cooling to simulate an accelerated thermal cycling (ATC) condition. Vibrations caused by an environmental chamber are circumvented by unique rigid links that connect the specimen to the moiré interferometer. Displacement fields are documented while the chamber is being operated. The system is utilized to analyze thermo-mechanical behavior of a ceramic ball grid array package assembly and a plastic ball grid array package assembly. The effect of thermal cycling on the accumulated permanent deformation is documented, which reveals the temperature-dependent non-linearity of solder joints.

The second apparatus is based on conduction heating and cooling to achieve a high ramp rate. A special chamber is designed and fabricated using a high power

thermoelectric cooler to achieve the desired ramp rate. The system is utilized to investigate the time-dependent behavior of solder joints.

A new solder joint configuration is designed and fabricated to be tested with the conduction based apparatus. The specimen is an extension of the conventional bi-material joint configuration but the unique design offers two important features; it negates the inherent shortcoming from cross sectioning required in moiré interferometry and produces a virtually uniform shear strain field at the solder joint. The deformation of solder joint is documented at a controlled ramp rate over several thermal cycles. The experimental results are analyzed and compared with those of Finite Element analysis to investigate the validity of solder constitutive models available in the literatures.

DEVELOPMENT OF MOIRÉ INTERFEROMETRY FOR REAL-TIME OBSERVATION OF NONLINEAR BEHAVIOR OF SOLDER AND SOLDER ASSEMBLY

By

Seungmin Cho

Dissertation submitted to the Faculty of the Graduate School of the
University of Maryland, College Park, in partial fulfillment
of the requirements for the degree of
Doctor of Philosophy
2005

Advisory Committee:
Associate Professor Bongtae Han, Chair
Prof. Abhijit Dasgupta
Prof. Sung Lee
Associate Professor Patrick McClusky
Associate Professor Peter Sandborn

Dedication

In memories of my Mother

Acknowledgements

First, I would like to express the deepest gratitude to my advisor, Dr. Bongtae Han for his continuous support and encouragement. Without his efforts, this work might not be possible. I would also like to thank all the members of my thesis committee, Dr. Abhijit Dasgupta, Dr. Peter Sandborn, Dr. Patrick McCluskey and Dr. Sung Lee for taking their time off their busy schedule to evaluate my work. I would like to thank Dr. Dasgupta for his invaluable suggestions and advices on my work and future research.

As a member of LOMS lab, I am indebted to many people in my group. John Dugan was always willing to help me designing and implementing an apparatus. Austin Cox, John Dugan and Arindam Goswami proofread this material painstakingly, which made it thousand times easier to read. Chris Hartsough provided all the gratings used in the experiments. Yuri Lee spent countless nights helping me running experiments and setting an experimental setup. Hongbo Bi was ready to answer my questions regarding image processing. Dr. Samson Yoon provided detailed knowledge on constitutive equations and ingenuous ideas for the latter half of this research. I would like to thank Dr. Zhaoyang Wang at Catholic University of America for customizing the analysis software so that the experimental results were analyzed in a much short time. I also express my gratitude to Sungyeol Cho for his help when I joined LOMS. Without his help, it would have been much harder. I would like to thank Changwoon Han for his help on FEA. All their help was essential to finish this work.

Special thanks to all my friends and colleagues, Joseph Varghese, Prachi Mehta, Daniel Farley, Kaushik Ghosh, Gayatri Cuddalorepatta, Karumbu Meyyappan, Kyungjun Kim, Daewhan Kim, Yuchul Hwang, Jonghee Lee for their help and support.

Last but not to the least, I would like to thank my brothers and sister for their support all through these years. They provided help and comfort whenever I needed them most.

Table of Contents

List of Tables

List of Figures

Chapter 1: Background and Objective

1.1 Basic Principles of Moiré Interferometry

Moiré interferometry can map the deformations of structures with extremely high resolution. The data are output as contour maps of in-plane displacements. A detailed description of moiré interferometry can be found in [5].

In moiré interferometry, a high-frequency cross-line grating on the specimen, initially of frequency f_s, deforms together with the specimen. A pair of parallel (collimated) beams of laser light strike the specimen with a prescribed incidence angle and a portion of the light is diffracted back, nominally perpendicular to the specimen, in the +1 and –1 diffraction order of the specimen grating. After the specimen grating is deformed as a result of the applied loads, these diffracted beams are no longer collimated. Instead, they are beams with warped wave fronts, where the warpages are related to the deformation of the grating. These two coherent beams interfere in the image plane of the camera lens, producing an interference pattern of dark and light bands, which is the moiré pattern.

These moiré patterns are contour maps of the U and V displacement fields, i.e., the displacements in the *x* and *y* directions, respectively, of each point in the specimen grating. The displacement of every *x,y* point in the field of view can be related to the fringes and their mathematical relationships are shown in Eq. 1-1.

$$U(x,y) = \frac{1}{2f_s} N_x(x,y) \qquad \text{1-1}$$

$$V(x,y) = \frac{1}{2f_s} N_y(x,y)$$

If the displacements fields are determined, linear strains can be obtained by employing the relationships between displacements and engineering strains as shown in Eq. 1-2.

$$\varepsilon_{xx} = \frac{\partial U}{\partial x} = \frac{1}{2f_S}\frac{\partial N_x}{\partial x},\ \varepsilon_{yy} = \frac{\partial V}{\partial y} = \frac{1}{2f_S}\frac{\partial N_y}{\partial y} \qquad \text{1-2}$$

$$\gamma_{xy} = \frac{\partial U}{\partial y} + \frac{\partial V}{\partial x} = \frac{1}{2f_S}\left[\frac{\partial N_x}{\partial y} + \frac{\partial N_y}{\partial x}\right]$$

In routine practice of moiré interferometry, f_s = 1200 lines/mm (30,480 lines/in.). In the fringe patterns, the contour interval is $1/2f_s$, which is 0.417 μm displacement per fringe order. The sensitivity is its reciprocal, or 2.4 fringes per μm displacement [5].

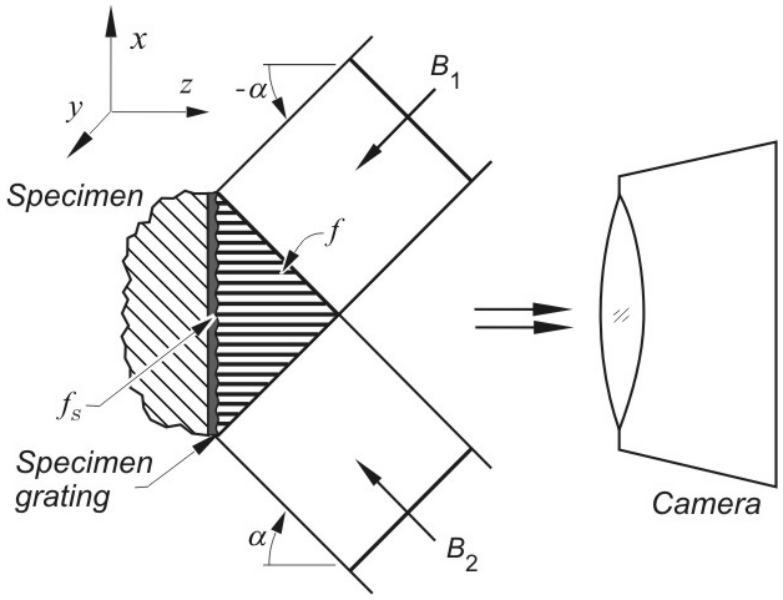

Figure 1-1 Schematic Diagram of moiré interferometry [5].

1.2 Application of Moiré Interferometry to Electronic Packaging

1.2.1 Introduction

Microelectronics devices contain many electronic components within an active silicon chip, such as transistors, capacitors, resistors, etc. To form a usable device, a silicon chip requires protection from the environment as well as both electrical and mechanical connections to the surrounding components. The technology dealing with these requirements is called *electronic packaging* [Ref.]. The physical design of an electronic package starts from the functions of the integrated circuits on the semiconductor chips and components. The design must provide access to all the terminals on the chips for input power and signal transmission. Secondly the design must provide the electrical wiring for interconnection. In addition, thermal energy transformed from electrical energy must be dissipated, and all the circuits must be protected from damage during next level assembly and its service life.

An electronic package is comprised of various conducting and insulating materials, which have different coefficients of thermal expansions (CTE). This non-uniform CTE distribution produces thermally induced mechanical stresses within the package assembly, especially solder interconnects.

The thermal stresses in microelectronics devices are one of the major causes for early product failure. Ideally, one would like to monitor the deformations under actual operating conditions when reliability assessment is sought. However, this is not practical

because of the relatively long life cycle. The microelectronics industry has been employing accelerated testing methods to cope with this problem, where the electronic devices are tested in much more severe environments, and the results are used to predict the number of cycles to failure at the actual operating conditions by employing a test acceleration parameter.

The most widely used test for reliability assessment is called the *Accelerated Thermal Cycling* (ATC) test. In the ATC test, the whole assembly is subjected to heating and cooling cycles in an environmental chamber. The electrical resistance of interconnections is monitored during thermal cycling to detect fatigue failure.

Finite element analysis (FEA) has been used extensively to estimate stresses and strains in electronic packaging structures under thermal cycling. Although one can model almost any kind of microelectronics device, simplifications and uncertainties are inevitable due to (1) simplified geometry, (2) limitations of constitutive properties, (3) uncertainties of material property, (4) complex loading, and (5) boundary conditions. The models require verification by other means before they are used for fatigue life prediction. Accordingly, advanced experimental techniques are in high demand to provide accurate results for deformation studies of microelectronics devices.

Moiré interferometry is a full-field optical method that has high displacement, strain and spatial resolution [5,6]. In recent years, the method has been used extensively in the electronics industry to determine thermal strains—strains caused by temperature changes—in microelectronics devices [14-38]. In the early papers on real-time observation [14-16], convection heating was used but the applications were limited to specimens with a simple geometry. The applicability of the method was extended to

specimens with complex geometry by Guo et al. [17, 18]. In the technique used in Refs. [17] and [18], called *bithermal loading* [6], only one elevated temperature condition could be investigated per test. Numerous applications of bithermal loading can be found in literature [17-23]. The bithermal loading approach was extended later to document inelastic deformations accumulated during thermal cycles [26]. The real-time observation was also extended for specimens with more complex geometry. Ham and et al. used thermoelectric modules and tape-type heaters to apply thermal loading on the specimen [30]. Wang and et al. also applied a conduction heating mechanism in the experiment [31,32]. However, heating/cooling rates and temperature ranges were limited in their experiments and they could not simulate an (ATC) condition because of the materials with poor thermal conductivity used in the packages.

1.2.2 Specimen Preparation

Moiré interferometry requires a plane of interest to be revealed and ground flat before specimen grating replication. A single package or assembly is typically trimmed from a fully populated board by using a medium speed diamond saw with a high concentration blade and a low speed high precision diamond saw. The trimmed package is inserted in a precision vise. The position of the package was adjusted under a low magnification stereo microscope until a desired cross section is aligned with the side of the vice under a stereo microscope. Then, the specimen is ground by setting the vise onto a variable speed grinding wheel with a fine grit grinding paper (typically 600 to 1200 grit) until a solder row along the edge of chip is exposed.

1.2.3 Specimen Grating Replication

The bar-and-space gratings of geometrical moiré cannot be printed with very high frequencies. Instead, phase gratings are used; the grating surface consists of a regular array of hills and valleys. For most analyses, the specimen grating is applied by the replication process illustrated by the cross-sectional views shown in Figure 1-2 [5]. This process uses a special mold, which is a plate with a cross-line phase grating on its surface. The grating is coated with a highly reflective metallic film, usually evaporated aluminum. A small pool of liquid adhesive is poured on the mold, and the specimen is pressed into the pool to spread the adhesive into a thin film. Excess adhesive is cleaned off repeatedly as it flows out. The mold is pried off after the adhesive has hardened. The weakest interface is between the metallic film and the cross-line grating, so the film is transferred to the specimen. Thus, a thin, highly reflective cross-line grating is firmly attached to the specimen surface, such that it deforms together with the specimen surface.

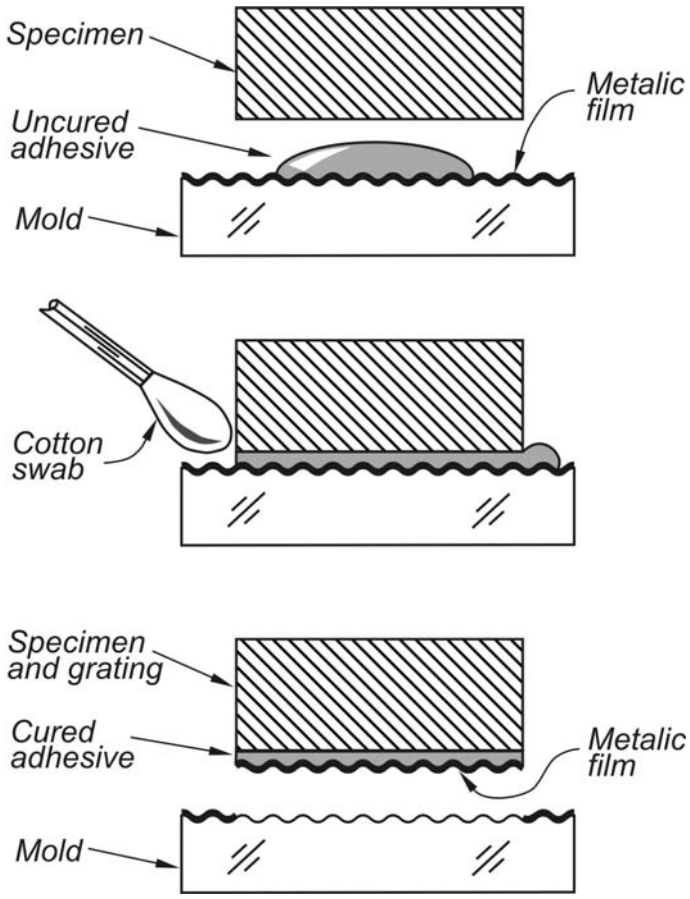

Figure 1-2 Steps in producing the specimen grating by a casting or replication process [5].

The adhesive thickness is typically about 25 μm (0.001 in.) for larger specimens– greater than 300 mm^2. For most analyses the thickness and stiffness of the grating is negligible. Various room temperature curing adhesives can be used, including epoxies, acrylics, urethanes, and silicone rubbers. Recent reports of success with instant cyanoacrylate cements have been circulated. Adhesives that cure by exposure to ultraviolet light have been used successfully. Techniques described below for replicating specimen gratings on electronic packages, to cope with the small complex structures, yield gratings about 2 μm thickness.

A special technique is required for replicating a specimen grating on the cross sections of microelectronic devices because they usually have such tiny and complex geometries that the excess adhesive produced by the grating replication procedure shown in Figure 1-2 cannot be swabbed away. The excess adhesive is critical since it could reinforce the specimen and change the local strain distribution.

An effective replication technique was developed to circumvent the problem [18,20,21]. First, a tiny amount of liquid adhesive, usually a small amount of epoxy is dropped onto the grating mold; the viscosity of the epoxy should be extremely low at the replication temperature. Then, a lintless optical tissue (a lens tissue) is dragged over the surface of the mold, as illustrated in Figure 1-3. The tissue spreads the liquid to produce a very thin layer of epoxy on the mold. The specimen is pressed gently into the epoxy, and it is pried off after the epoxy has polymerized. Before polymerization, the surface tension of the epoxy pulls the excess epoxy away from the edges of the specimen. The result is a specimen grating with a very clean edge. The specimen must be made very flat and smooth to be compatible with the thin film of epoxy.

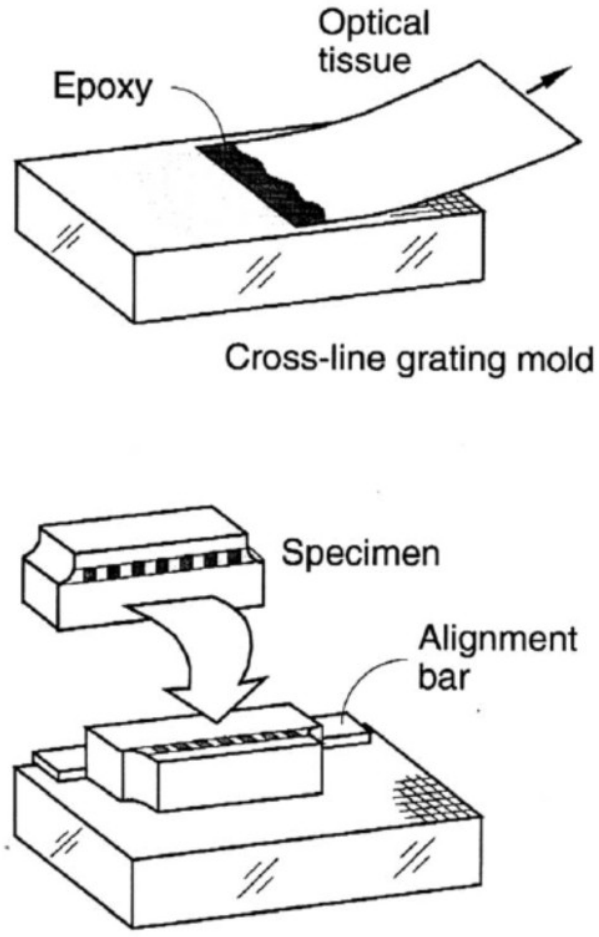

Figure 1-3 Procedure to replicate a specimen grating on a specimen with a complex geometry [5].

1.3 Research objective

The objective of this dissertation is to develop innovative schemes of moiré interferometry for real-time observation to study the time and temperature dependent thermo-mechanical material behavior. Two types of temperature control mechanisms are

considered to achieve the goal; convection based-temperature control and conduction-based temperature control.

The convection-based scheme is needed to simulate the ATC conditions, where the convectional heating/cooling with vigorous airflow around the specimen is desired to apply a uniform temperature. Vibrations caused by the environmental chamber are to be circumvented while the chamber is being operated.

Although effective for reliability assessment of actual package assemblies, the convection-based scheme simulating the ATC condition do not provide extreme ramp rates and accurate temperature controls that the more controlled experiments for fundamental studies require. A different scheme using conduction heating/cooling is designed to achieve the level of ramp rates and the accuracy.

The convection scheme is utilized to characterize the thermo-mechanical behavior of ball grid package assemblies and the conduction scheme is implemented with an idealized solder specimen configuration to verify validity of the existing constitutive properties.

1.4 Nomenclature and Terminology

f = Frequency of virtual reference grating, with 2400 lines/mm

U, V= Displacements in the x and y dimensions, respectively

α= The coefficient of thermal expansion

ν = Poisson's ratio

E= Young's Modulus

G= Shear modulus of elasticity

ε= Normal strains

γ= Shear strains

Chapter 2: Development of Convection-Based System

2.1 Introduction

In order to document thermal deformations of electronic packages under ATC tests, it is necessary to implement moiré interferometry for a convection-based environmental chamber. This chapter presents a unique implementation of moiré interferometry, which copes with the vibrations caused by the convection chamber and thus allows real-time observation of thermal deformations. The system is based on a portable moiré interferometer and a computer controlled convection oven. In spite of the high amplitude of vibration produced by the oven, which is considerably higher than the submicron displacement sensitivity of moiré interferometry, the proposed approach produces exceptionally stable fringes.

2.2 Development of Optical/mechanical Setup for Real-time Observation

2.2.1 Mechanical Configurations

When deformation measurements are required during accelerated thermal cycling, it is necessary to implement moiré interferometry with an environmental chamber that provides convection heating and cooling. The air inside the chamber must be circulated vigorously to achieve the heating/cooling rate required for a typical ATC condition. Consequently, the environmental chamber experiences vibrations, which are normally

transmitted to t

inadvertent vibr

Howeve

specimen and t

to cope with th

portable moiré

environmental

and the port. The glass cloth blocks the air currents effectively, without transferring vibrations of the chamber to the rod and the interferometer.

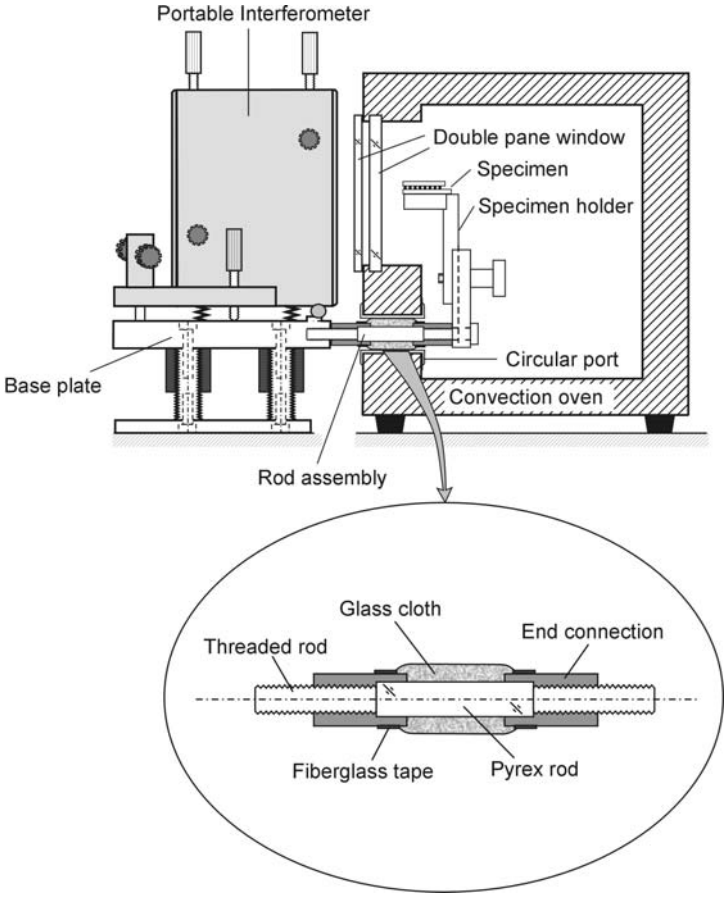

Figure 2-1 Schematic illustration of the real-time moiré setup. The insert shows the detailed rod assembly.

2.2.2 Optical Configurations

For the large temperature excursion during thermal cycling of –40 °C to 120 °C, a double-pane window was used to prevent heat from transmitting to the moiré system.

More importantly in practice, it was needed to avoid moisture condensation at cryogenic temperatures.

The moiré system uses a coherent light and any undesired reflections can cause ghost patterns. Furthermore, there will be 4 glass/air interfaces and the light intensity can be reduced significantly due to reflection. The following analysis was conducted to optimize the optical configuration.

The incidence angle of the moiré interferometry can be determined from

$$\sin\alpha = f\lambda/2 \qquad \text{2-1}$$

Considering a He-Ne laser with λ = 632.8 nm and the virtual reference grating with a frequency of 2400 lines/mm, the angle of incidence becomes 49.4°.

As light travels through media with different refraction indexes, some portion of the light transmits and the rest is either absorbed by the material or reflected at the boundaries. Absorption is usually is small and ignored. Then transmission and reflection of the light can be determined by using Eq. 2-2 [1].

$$R_{\perp} = \left(\frac{n_i \cos\theta_i - n_t \cos\theta_t}{n_i \cos\theta_i + n_t \cos\theta_t} \right)^2, \quad R_{\square} = \left(\frac{n_t \cos\theta_i - n_i \cos\theta_t}{n_i \cos\theta_t + n_t \cos\theta_i} \right)^2 \qquad \text{2-2}$$

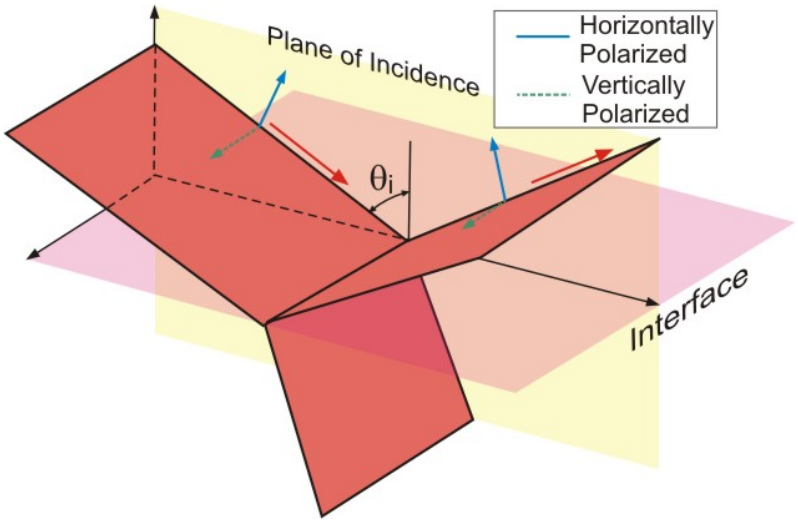

Figure 2-2 Light propagation at the interface and the definition of polarization of light

In the Eq. 2-2, $\perp$ and $\parallel$ indicate the direction of polarization. The reflectance of the light depends on the refraction indices, the incidence angles, and the direction of polarization. Figure 2-2 illustrates light propagation at the interface as well as the definition of the polarization. If light is polarized parallel (vertical) to the plane of incidence, it is defined as horizontally (vertically) polarized.

Figure 2-3 shows the reflectance with respect to the polarization vs. incidence angle. The reflectance at the incident angle of 49.4° is $R_\alpha = 0.11$ for a vertically polarized beam and $R_\alpha = 0.002$ for a horizontally polarized beam. The corresponding transmittance is $T_\alpha = 0.89$ and 0.998 for the vertically and horizontally polarized beams, respectively.

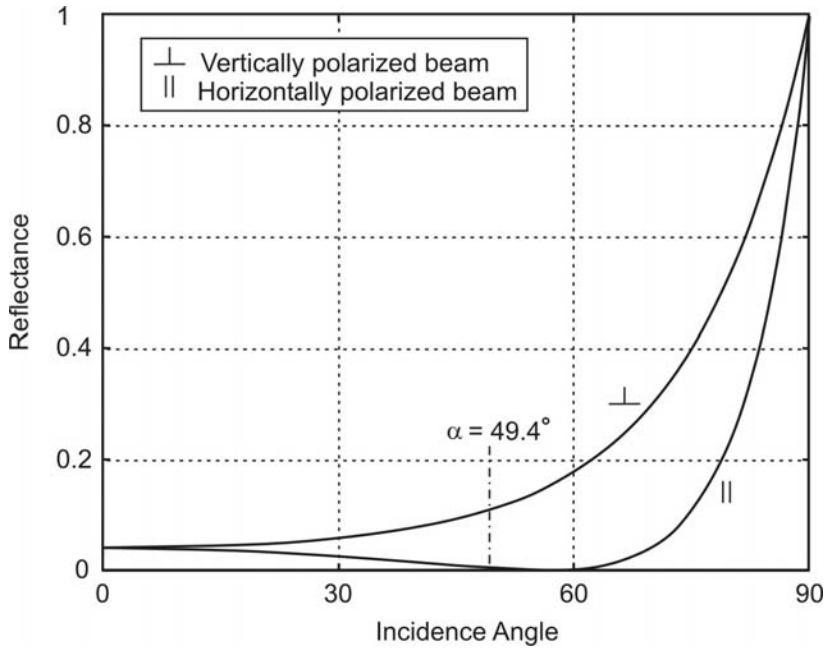

Figure 2-3 Reflectance of light with polarization

The beam experiences reflections four times before it reaches the specimen and the fraction of the initial intensity on the specimen can be calculated as

$$I_0 = T_\alpha^4 I_i = \begin{cases} 0.63 I_i & \text{(For vertically polarized beam)} \\ 0.98 I_i & \text{(For horizontally polarized beam)} \end{cases} \quad 2\text{-}3$$

As can be seen from Eq. 2-3, significant intensity loss will be resulted if the direction of polarization is chosen properly. In order utilize the light intensity most effectively, the polarization of the beam should be kept parallel to the plane of incidence. Figure 2-4 shows the polarization direction of the four beams used for the real time moiré interferometry.

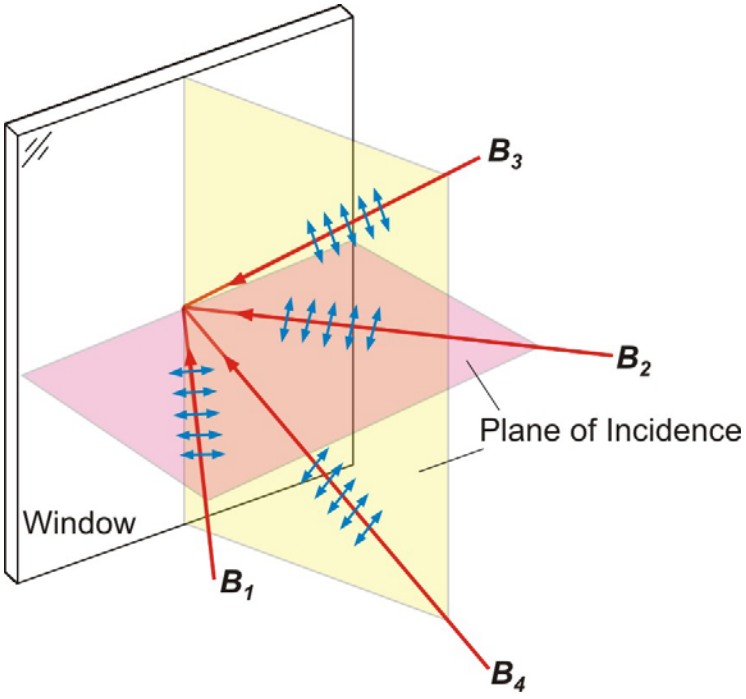

Figure 2-4 Polarization for the optimal use of light

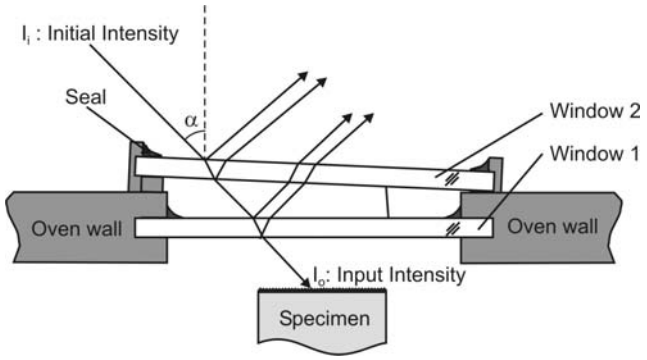

Figure 2-5 Light transmitted and reflected from double pane window

Undesired interference patterns with high visibility can result from the multiple reflections. Two major sources of the undesired interface patterns are identified as illustrated in Fig. 2-6: (1) the patterns associated with the specimen surface and windows (2) the patterns associated with the gap between two windows. They were nullified by making an appropriate angle among them.

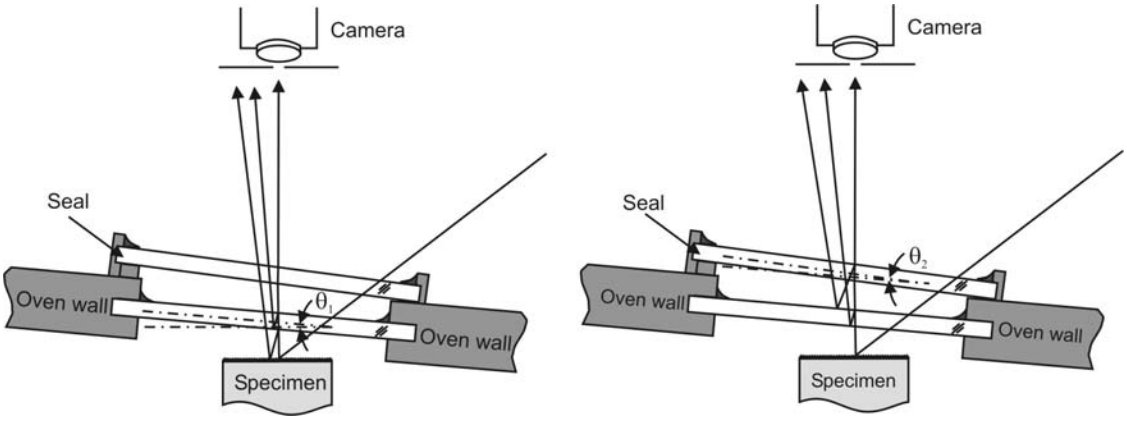

Figure 2-6 Undesired interference patterns

2.2.3 Environmental Chamber Control

Two K-type thermal probes–a chamber probe that documents air temperature at the inlet, and a user probe that documents specimen temperature–control the temperature of the chamber. The user probe is attached to a specimen and its output controls the thermal cycle of the chamber by means of a PIDA (proportional, integral, derivative, and advanced) control system.

A window-based program was written to control and log the temperatures during the experiment. Extreme care was exercised in writing the control routine in order not to exceed the target temperatures during the thermal cycle since inelastic deformations produced at the higher temperatures cannot be recovered by cooling the specimen back to the target temperature. Figure 2-7 shows representative specimen temperatures as a function of time. In spite of the additional thermal mass inside the chamber, a heating/cooling rate of 10°C/min. was achieved while effectively keeping the

temperatures below the target values. Temperature histories from the chamber were collected by computer in every 5 seconds.

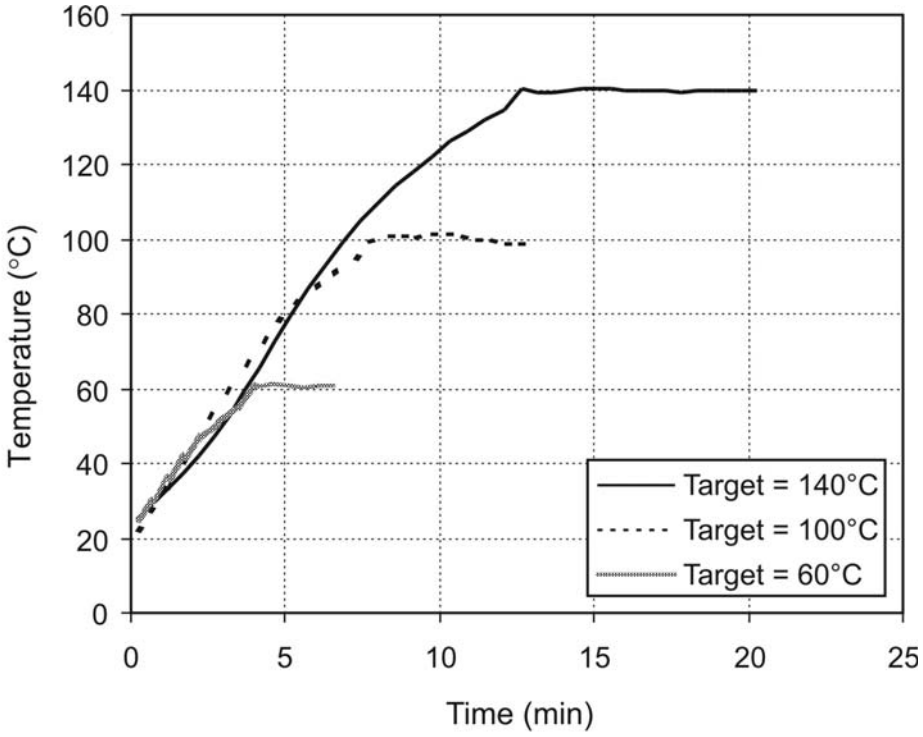

Figure 2-7 Illustration of temperature profile obtained from PIDA control

Figure 2-8 shows the specimen temperature history obtained from the environmental chamber [73]. During the temperature excursion from –20°C to 120 °C, an average ramp rate of 10ºC/minute was achieved and the maximum overshoot of less than 2 °C was observed at the peak temperature.

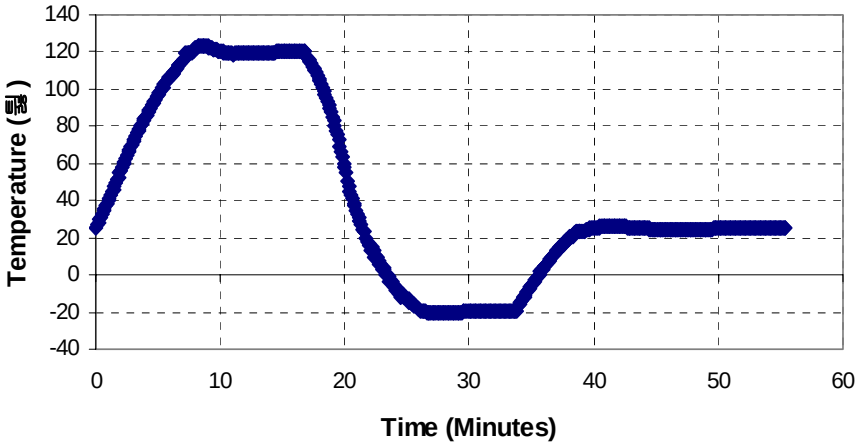

Figure 2-8 Illustration of temperature profile obtained from PIDA control [73]

2.2.4 Characterization of Testing Apparatus

A preliminary experiment was conducted to investigate the stability and repeatability of the proposed scheme. The specimen was a block fabricated from Carpenter Stainless Steel. The fringe patterns were recorded at intervals of 40°C while heating and cooling the specimen. Two representative fringe patterns are shown in Figure 2-9 (a). The coefficient of thermal expansion (CTE) over each temperature interval can be calculated from the fringe patterns by

$$\mathrm{CTE\,(ppm/°C)} = \frac{1}{f}\frac{\Delta N}{L\Delta T}\times 10^{6} \qquad 2\text{-}4$$

where L is the gage length (10mm), ΔN is the change in fringe orders over L, ΔT is the temperature change, and f is the virtual reference frequency (2400 lines/mm). The results are plotted in Figure 2-9 (b). A nearly constant CTE value (15.9 ± 0.1 ppm/°C)

was obtained over the temperature range of 0°C to 120°C, which confirms the stability and accuracy of the measurement scheme.

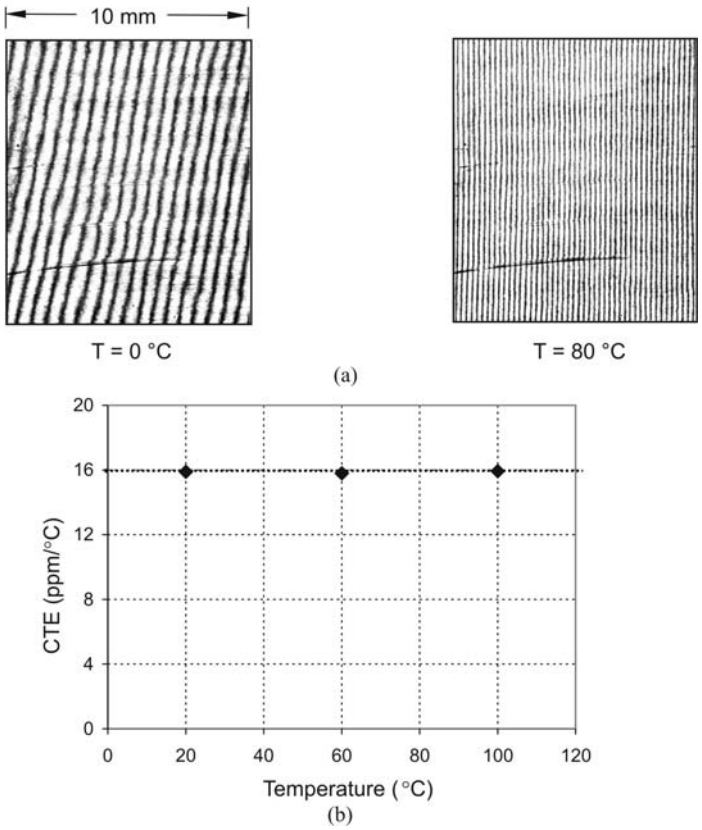

Figure 2-9 (a) Fringe patterns obtained from a stainless steel block and (b) CTE obtained from the fringe patterns.

If tuned properly, moiré interferometry is essentially insensitive to the out-of-plane displacement. If an accidental out-of-plane rigid-body rotation occurs during application of the loads, the out-of-plane slope resulting from the rotation about an axis parallel to the grating lines is seen as a foreshortening of the specimen grating. The foreshortening produces a uniform apparent compressive strain throughout the specimen [5]. Usually the apparent strain is small and can be neglected when the load-induced

strain is large. However, when small strain is crucial, such as measurement of the effective CTE, the apparent strain cannot be neglected.

In order to prevent the rigid-body rotation, the specimen was glued to the specimen holder using a silicon rubber (RTV 736), as illustrated in Figure 2-10. The silicone rubber provided desired position stability while its low modulus decoupled the mechanical constraints from the specimen holder.

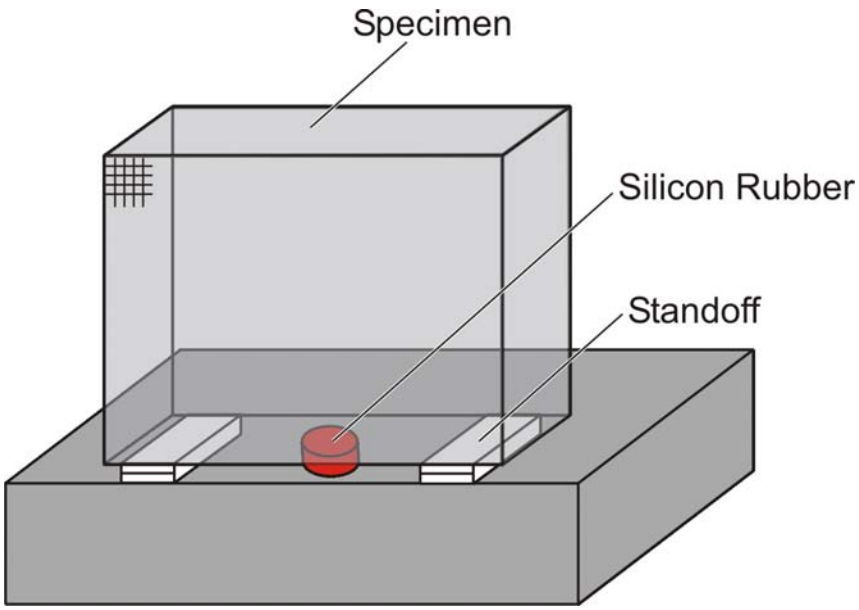

Figure 2-10 Specimen holding mechanism for the specimen with a high profile

2.2.5 Implementation: Plastic Ball Grid Array Package Assembly

In this investigation, a central strip was cut from a plastic ball grid array (PBGA) package. The schematic drawing and component materials are shown in Figure 2-11. A thin grating was applied by the method of Figure 1-3, and experimental analysis was

conducted with the real-time apparatus. The specimen was subjected to a thermal cycle ranging from -20°C to +125°C. The *U* and *V* fields were recorded at several temperatures during the heating and cooling stages of the cycle and are shown in Figure 2-12. The fringe patterns show the quality of the data recorded at elevated temperatures. The fringes are clearly resolved in the homogeneous materials; they are resolved, too, in the printed circuit boards, but the heterogeneous nature of those composite materials caused locally irregular deformations and very complex fringes. Without a detailed analysis, visual inspection of the *V* field shows opposite directions of curvature in the chip region before and after the 125°C temperature; this behavior results from creep of the solder and molding compound. Whereas extensive computational analysis is undertaken for the mechanical design of electronic packages, the complexities of geometry and materials necessitate experimental guidance and verification.

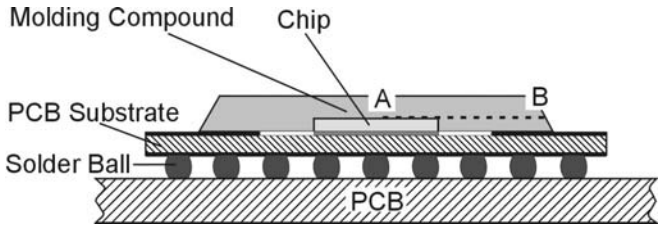

Figure 2-11 Schematic diagram of PBGA package assembly.

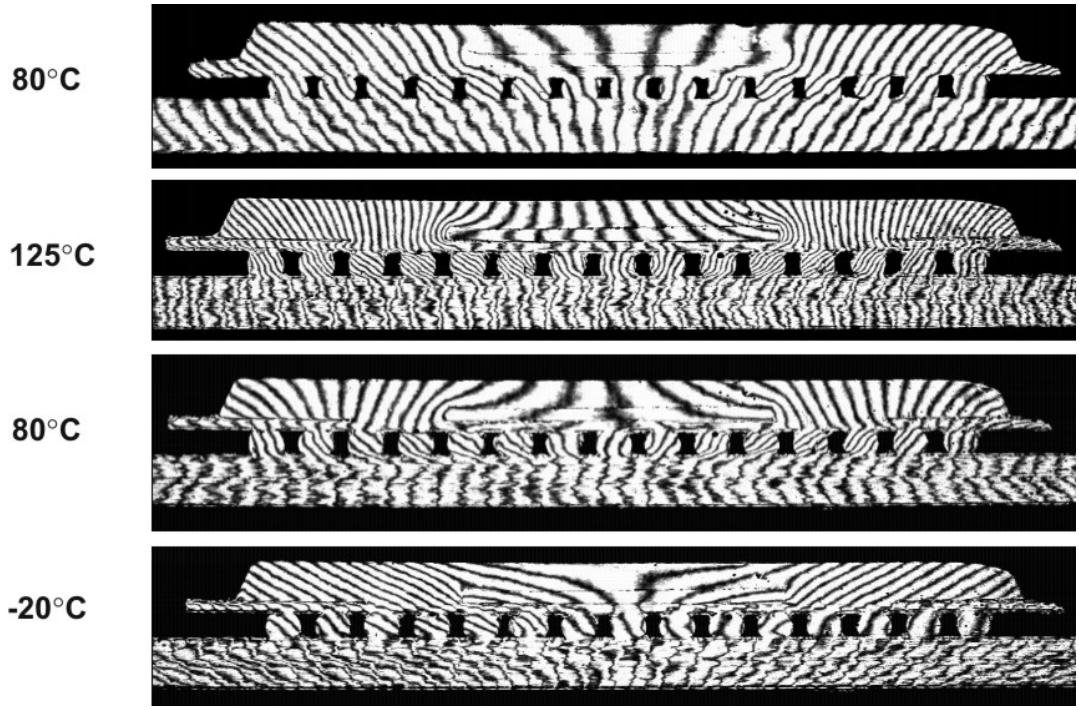

(a)

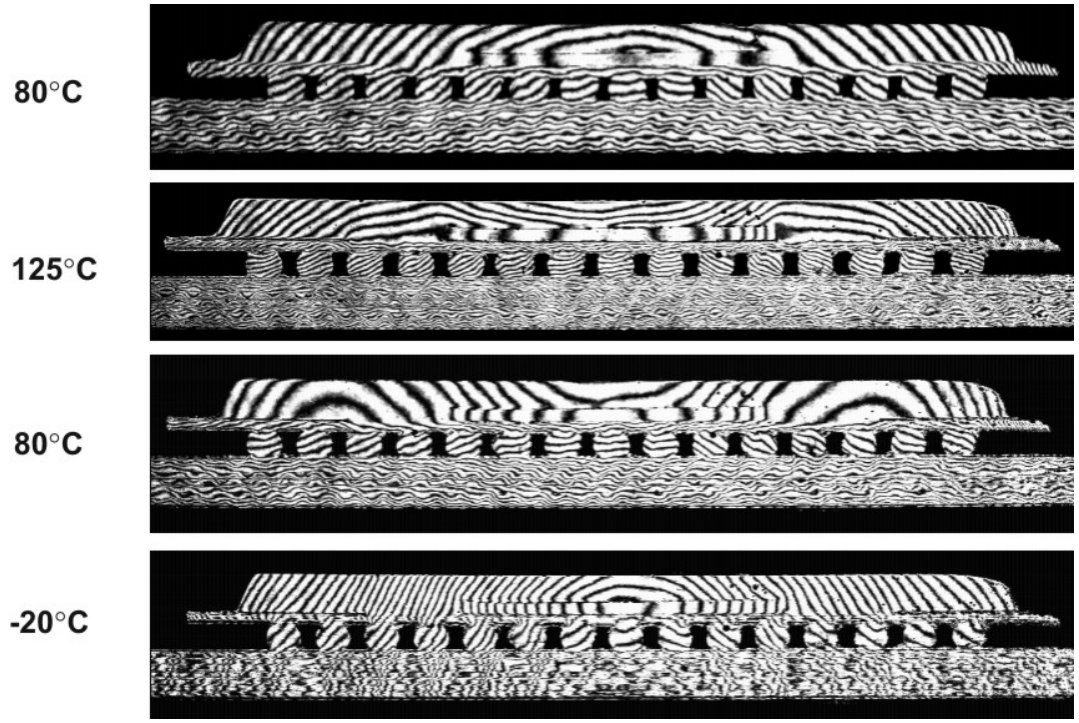

Figure 2-12 (a) Representative (a) U field pattern (b) V field pattern.

Chapter 3: Application of Convection-Based System

3.1 Temperature Dependent Deformation Analysis of Ceramic Ball Grid Array Package Assembly under Accelerated Thermal Cycling Condition

3.1.1 Introduction

Ceramic area array package technology allows attachment of high I/O multilayer ceramic modules directly to an industry standard epoxy/glass printed circuit board (PCB) [39, 40]. The technology has been used successfully for various flip chip applications. The solder interconnection of the package assembly consists of a high melting point solder ball (90%Pb/10%Sn) and a eutectic solder fillet (63%Pb/37%Sn). The high melting point solder ball does not reflow during the assembly process, which provides a consistent and reproducible standoff between the ceramic package and the PCB.

The dominant mode of deformation of the solder interconnection is shear deformation, which is caused by the CTE mismatch of the ceramic module and the PCB [18, 41]. Consequently, the shear strains at the interconnection increase as the distance from the neutral point (DNP) increases.

The temperature and time dependent thermo-mechanical behavior of a CBGA package assembly subjected to an accelerated thermal cycling (ATC) condition was investigated. Due to the stability of real time moiré setup, displacement fields are documented while the chamber is being operated. The results corroborate the trends found in earlier observations [17, 20, 26], but they reveal the behavior in greater detail.

3.1.2 Specim

The ass

(19 x 19 solde

strip array conf

solder interconn

solder ball was

Sp

3.1.3 Global Deformation

Representative vertical displacement fields of the assembly are shown in Figure 3-2. Relative vertical displacements with respect to the axis of symmetry (referred to as *bending displacements*) along the middle line of the ceramic module were determined by Eq. (1) using the fringe orders, N_y, assigned in the fringe patterns. The results obtained from the right half of the ceramic module are plotted Figure 3-3. When the assembly was heated to 55°C (B), the PCB expanded more than the module, which produced an upward bending of the module ($\cup$). The bending displacement increased as the temperature increased to 75°C (C). However, the bending displacement decreased when the temperature further increased to 100°C. During the dwell period at 100°C, the bending displacement decreased to nearly zero. When the assembly was cooled to 55°C (E), the module bent downward ($\cap$). The magnitude of downward bending increased continuously throughout the entire cooling process.

This significant non-linear behavior is described schematically in Figure 3-4. The initial heating produced the upward bending of the assembly, consistent with the CTE mismatch between the module and the PCB, and the coupling through the solder interconnections. At temperatures higher than 75°C, creep of the solder became a dominant effect. As a result, deformation of the module decreased while the temperature increased. At 100°C, the coupling between the module and the PCB diminished until the assembly was in a nearly stress-free state. The solder interconnection experienced large inelastic deformations. During cooling, the CTE mismatch produced downward bending of the assembly since the reference temperature of zero bending displacement changed

from room temperature to 100°C. There was virtually no stress relaxation during cooling below 75°C. The magnitude of the bending displacement increased as the temperature decreased.

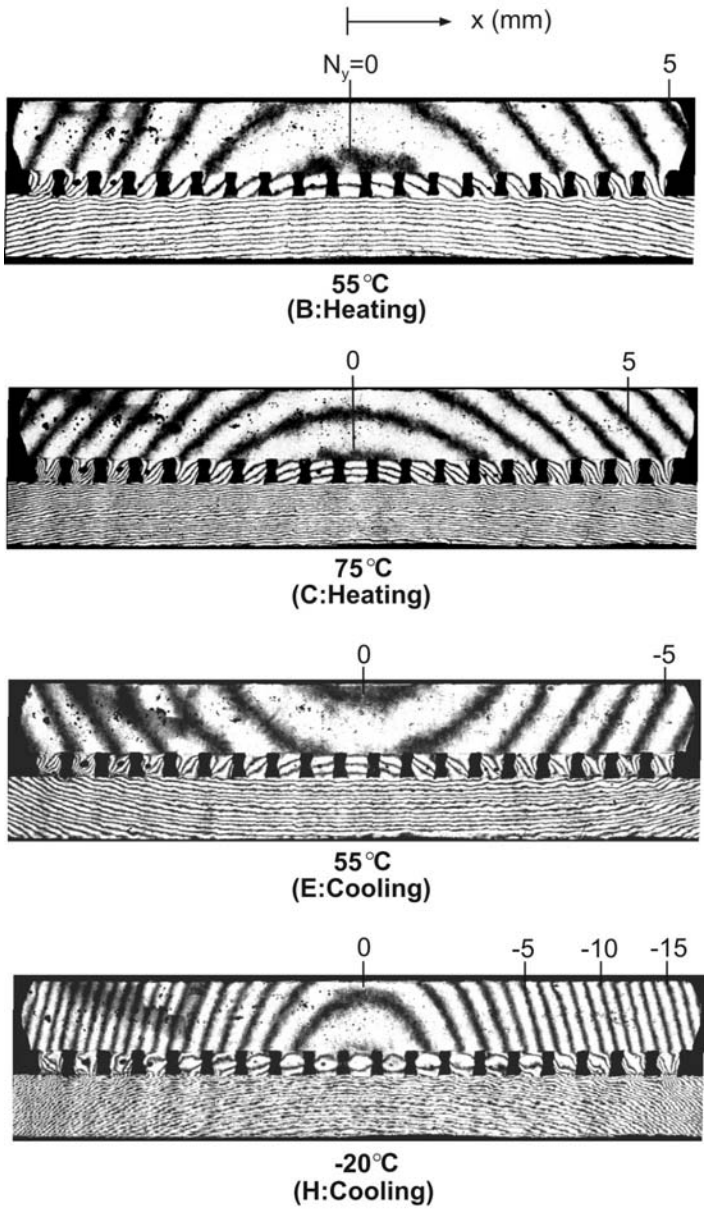

Figure 3-2 Representative V field fringe patterns

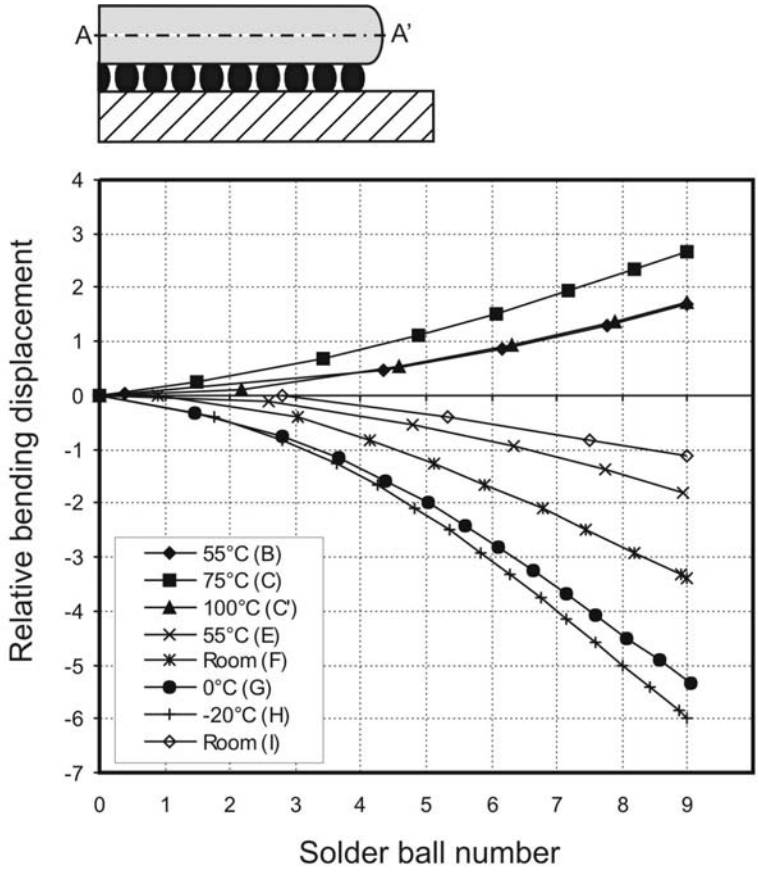

Figure 3-3 Relative bending displacement

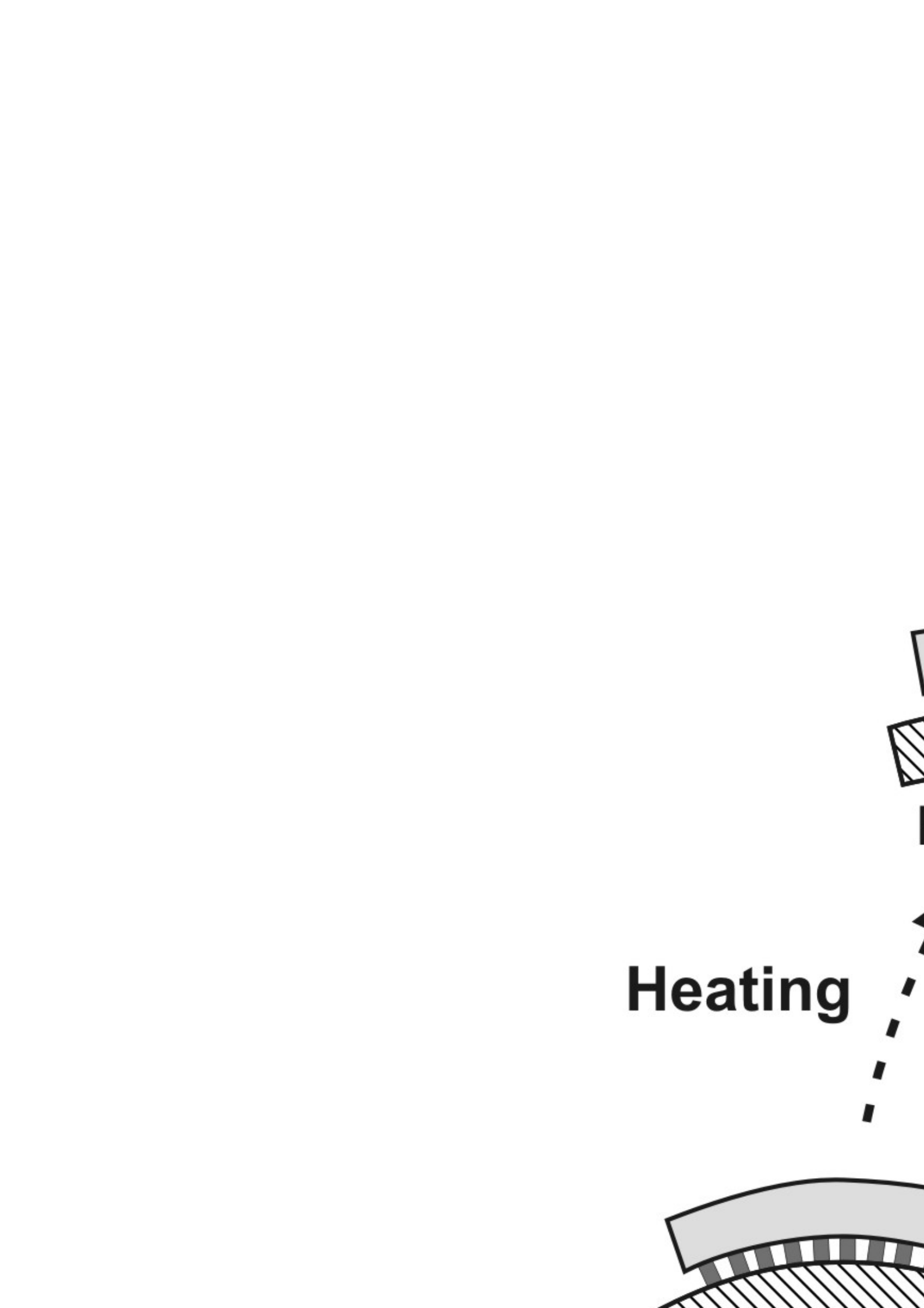
Heating

shear deformat

bottom eutectic

bottom fillet is

The dev

Figure 3-6, whi

corresponding

various stages i

shear strain in t

maximum temp

cooled down to

recovered comp

was cooled to

horizontal disp

displacement ir

3.1.5 Discuss

It was

unchanged whi

the modulus o

(E_{hm}); at 100°C

E_{hm} becomes m

observed in this

the maximum t

than the minim

maximum temp

and its magnitu

models also do

cycle although

The def

125°C for 15 m

did not occur

assembly, whi

displacements

the eutectic fill

CBGA package

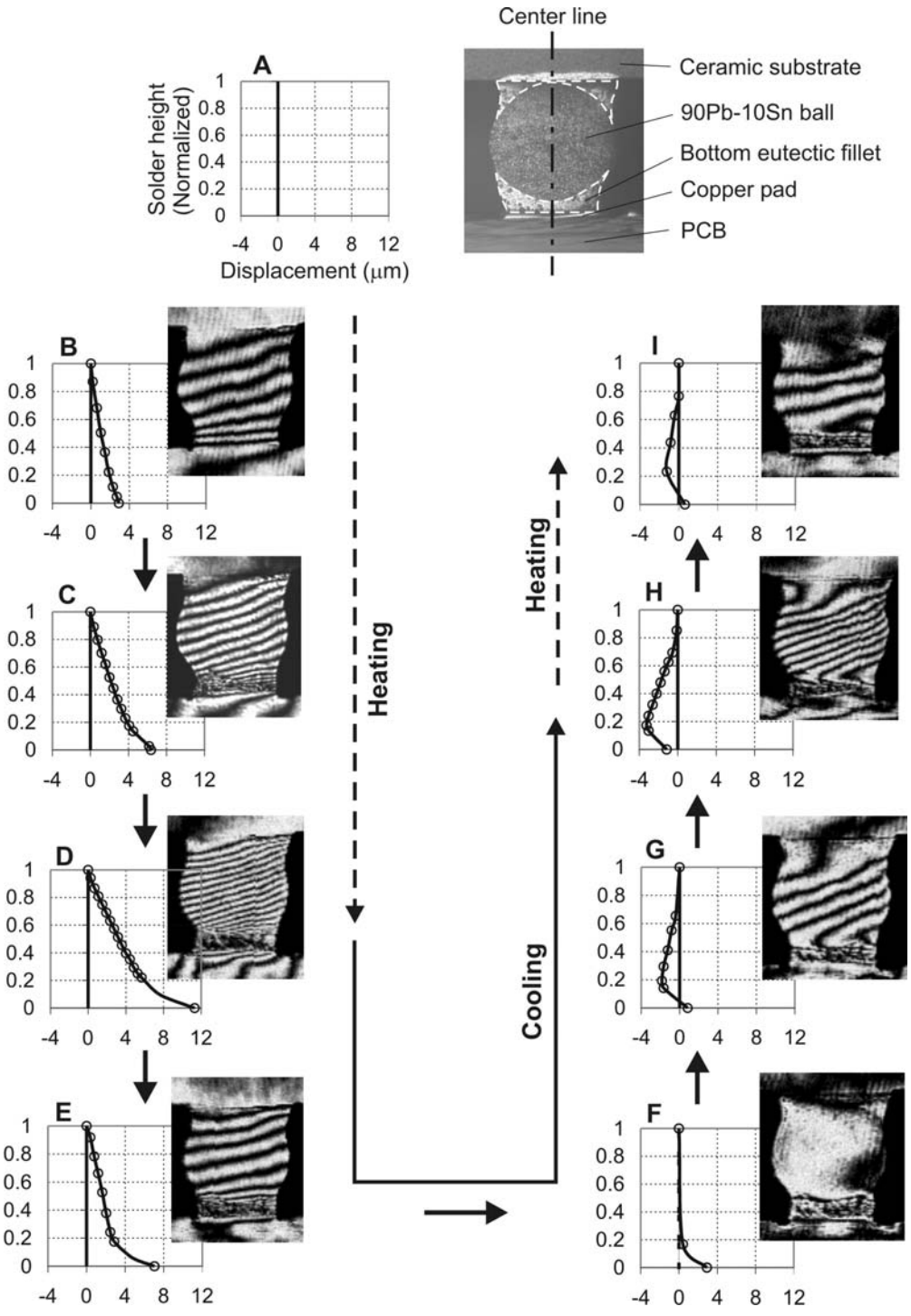

Figure 3-6 U field fringe patterns of the rightmost solder interconnection and the corresponding horizontal displacements determined along the vertical centerline

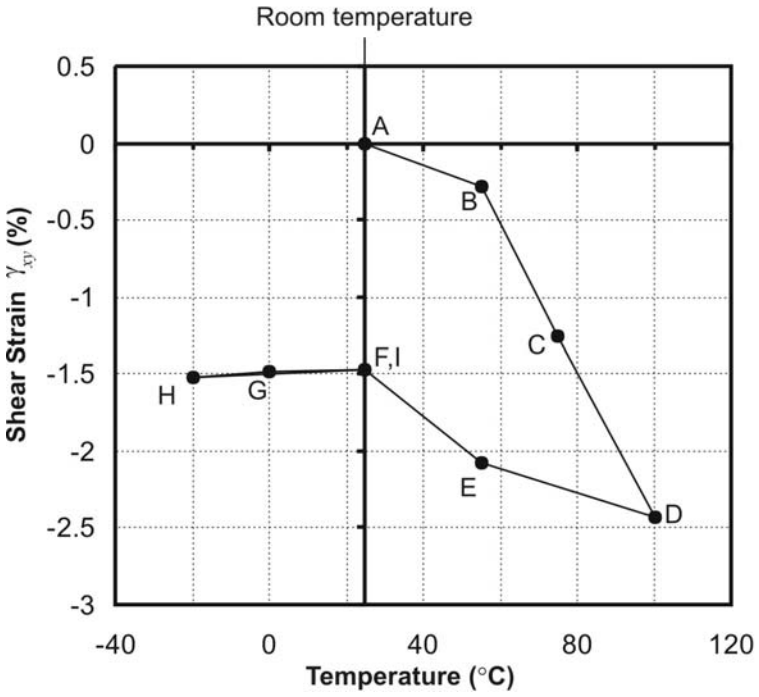

Figure 3-7 Average shear strain of eutectic fillet

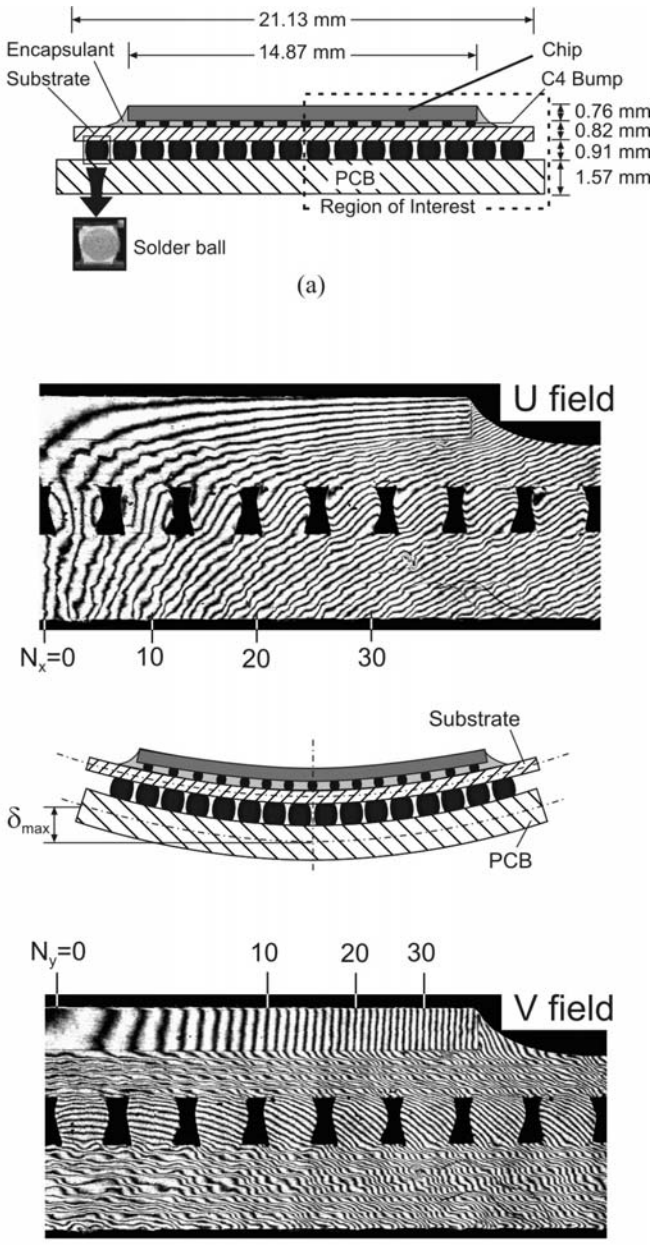

Figure 3-8 (a) Schematic diagram of FC-PBGA package assembly and (b) U and V field fringe patterns recorded at 125°C

3.2 Characterization of Flexural and Thermo-mechanical and Mechanical Behavior of PBGA Package Assembly

3.2.1 Introduction

A plastic ball grid array (PBGA) package assembly is comprised of various materials that have different thermo-mechanical properties. These dissimilar properties of silicon die, molding compound, and printed circuit board (PCB) produce complex deformation fields in the assembly when it is subjected to cyclic thermal and/or mechanical loadings. As demand for the PBGA package in portable electronics products increases, understanding of its flexural and thermo-mechanical behavior becomes important for an optimum design for enhanced reliability.

Both flexural and thermo-mechanical behavior of an overmold type PBGA package assembly is characterized by moiré interferometry. Fringe patterns are recorded and analyzed for several bending loads and temperatures. Detailed global and local deformations of the assembly by the two loadings are presented and the results are compared to identify the most dominant deformation modes.

3.2.2 Specimen Configuration and Preparation

The package assembly used in the experiment was a 27 mm Wire-Bond PBGA package with 225 I/Os (15 x 15 solder interconnection array) mounted on an FR-4 PCB with eutectic solder balls. In the package, an active chip is first bonded to an organic substrate, and the integrated circuits are connected electrically to the bond fingers on the

substrate by thermo-sonic gold wire bonding. The device is then overmolded to form a PBGA package. For the final assembly, the package is connected mechanically and electrically to a PCB using a uniform array of solder balls.

The specimen with a strip array configuration was prepared from the assembly, containing several central rows of solder interconnections. The cross-section of the PBGA package assembly is shown in Figure 3-9 with relevant dimensions. The solder balls were 0.97 mm high and the largest diameter was 1.10 mm. The pitch between solder balls was 1.50 mm.

One side of the specimen was ground flat to expose the largest cross-section of the solder balls. The drag method was utilized to replicate a specimen grating. The specimen was kept at 100°C in the environmental chamber for about 2 hours before specimen grating replication. This procedure ensured removal of any preexisting moisture in the assembly.

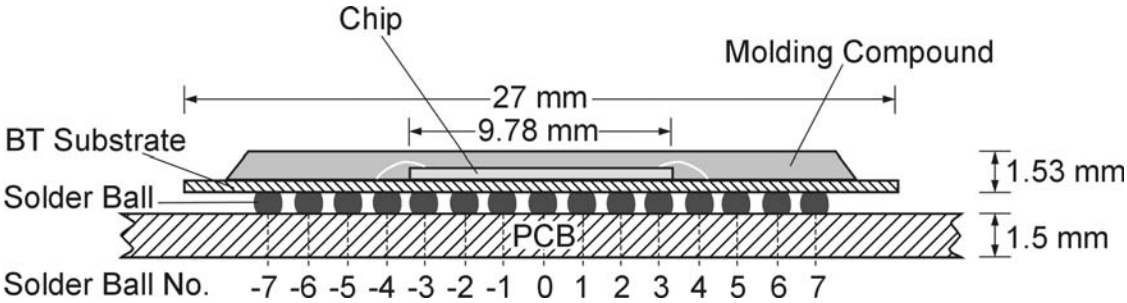

Figure 3-9 Schematic diagram of a sectioned WB-PBGA package assembly.

3.2.3 Experi

3.2.3.1 Flex

A flexu

to one introduc

loadcell, upper

displacements are applied. The load was measured with an accuracy of 0.4 N by the electrical load cell.

For accurate assessment of the applied bending moment, the two bending platens had a saw tooth profile and the bending moment was applied through pins positioned in the grooves. As shown in the insert, the specimen with an undeformed grating was placed between the platens in such a way that two upper pins were positioned between solder balls -7 and -6, and 6 and 7. Two lower pins were positioned on the PCB. The pins were wrapped with a Teflon tape to negate the friction between the fixture, the pins, and the specimen.

With this loading configuration, a uniform bending moment is applied between the balls –6 and 6. The package assembly was loaded and the fringe patterns were recorded at the uniform bending moments of 14.1, 28.2, 42.3, 56.4 and 70.6 N·mm. The specimen was then unloaded, and the fringe patterns representing permanent deformations were recorded.

The representative fringe patterns are shown in Figure 3-11. Due to excessive displacements, only a portion of the specimen (the region marked by a dashed box in the fringe pattern of 28.2 N·mm) is shown for the higher bending moments and residual deformations (after unloading).

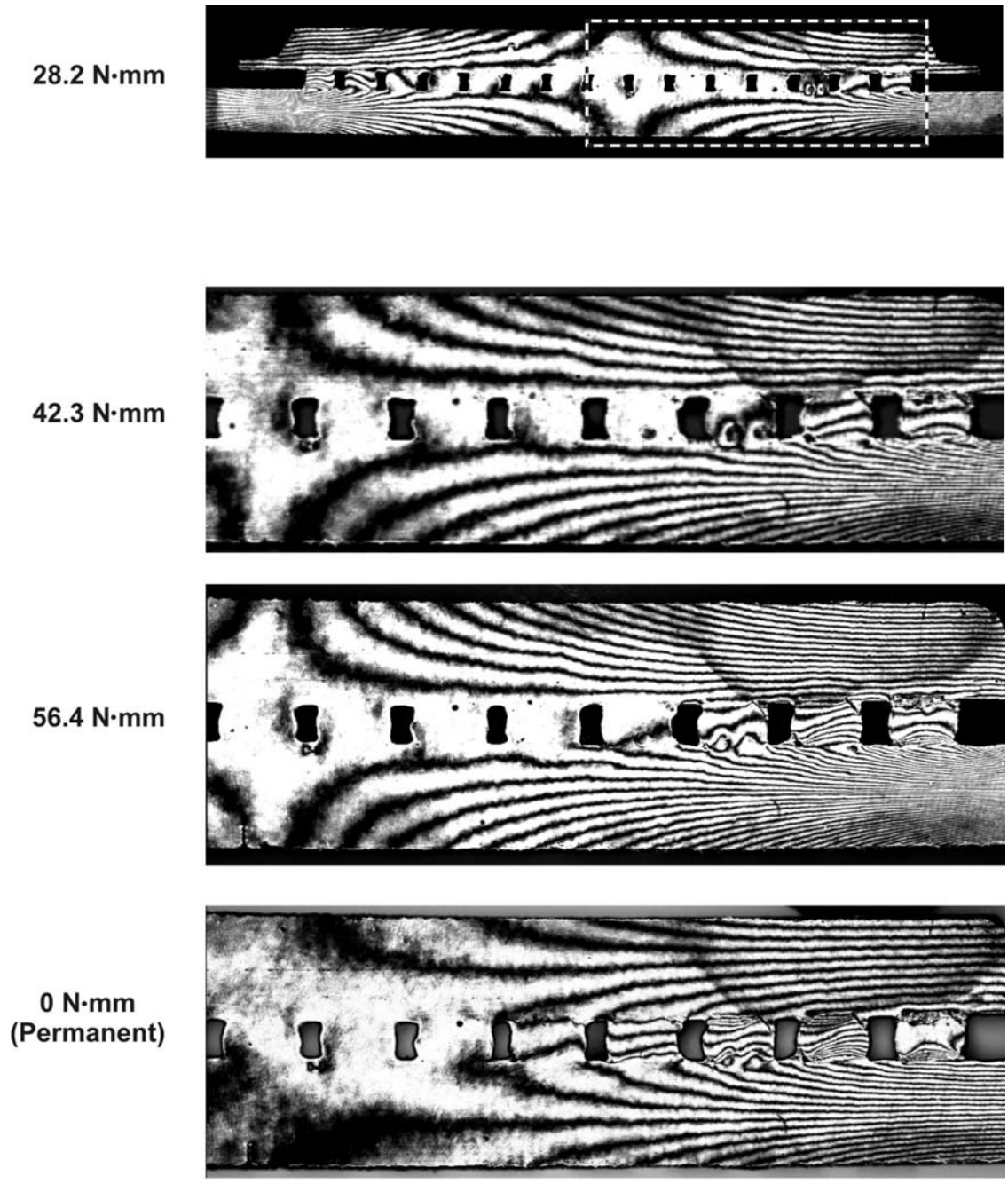

(a)

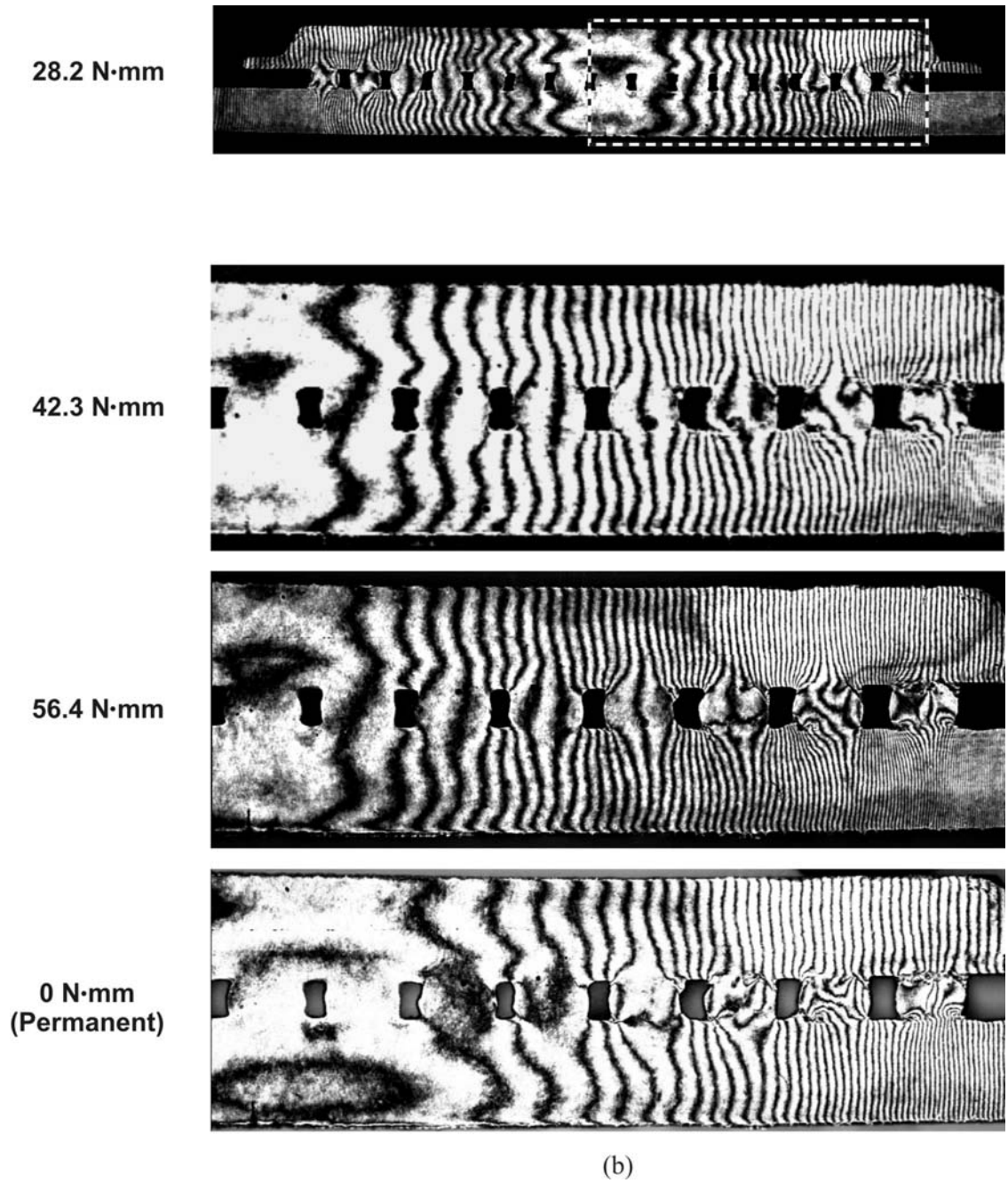

Figure 3-11 Representative (a) U and (b) V field fringe patterns produced by mechanical bending

3.2.3.2 Thermal Loading

The package assembly with a configuration identical to that used in the mechanical test was prepared and installed in the environmental chamber at room temperature. The specimen was then subjected to a thermal cycle, where the maximum and minimum temperatures were 125°C and -40°C, respectively. The fringe patterns were recorded at several temperatures during the thermal cycle. A complete thermal loading history is shown in Figure 3-12.

The representative fringe patterns obtained at 80°C (heating), 125°C (heating), 80°C (cooling) and -20°C (cooling) are shown in Figure 3-13. The fringe patterns induced by the temperature excursion were quite different from those induced by mechanical bending. The difference was ascribed to the superposition of thermal expansion in all directions onto the global bending caused by the mismatch of CTE. The difference between the fringes at 80°C (heating) and 80°C (cooling) highlights the temperature-dependent nonlinear behavior of the package assembly.

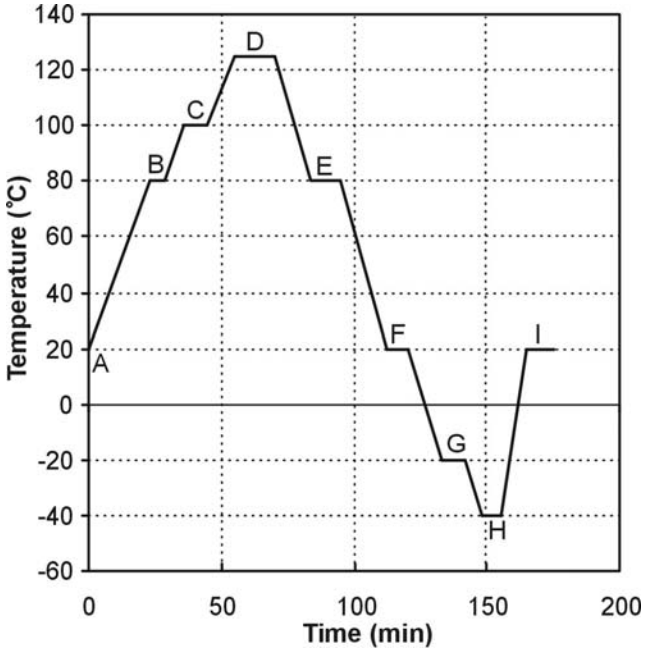

Figure 3-12 Temperature profile

80°C (B)

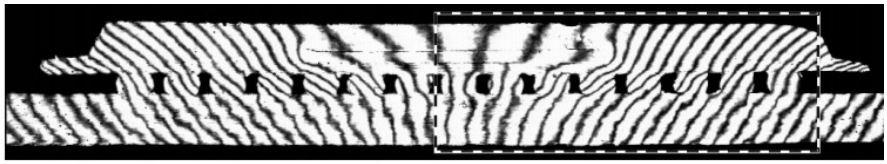

125°C (D)

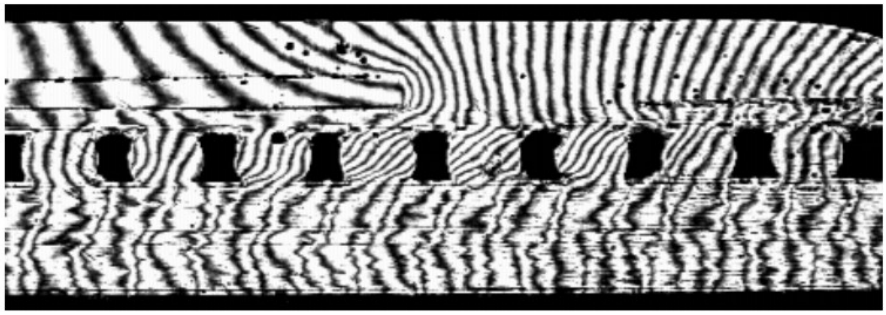

80°C (E)

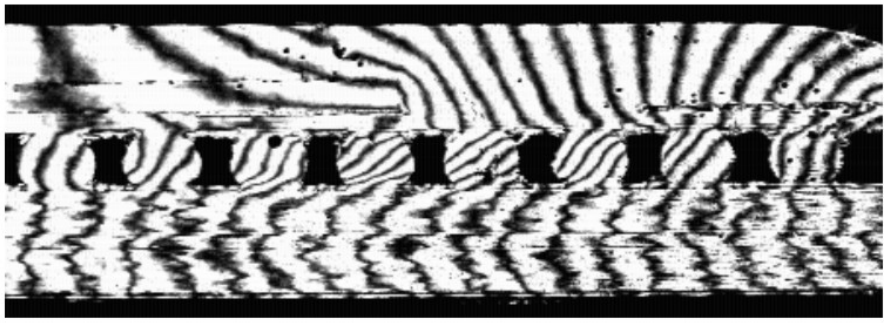

-20°C (G)

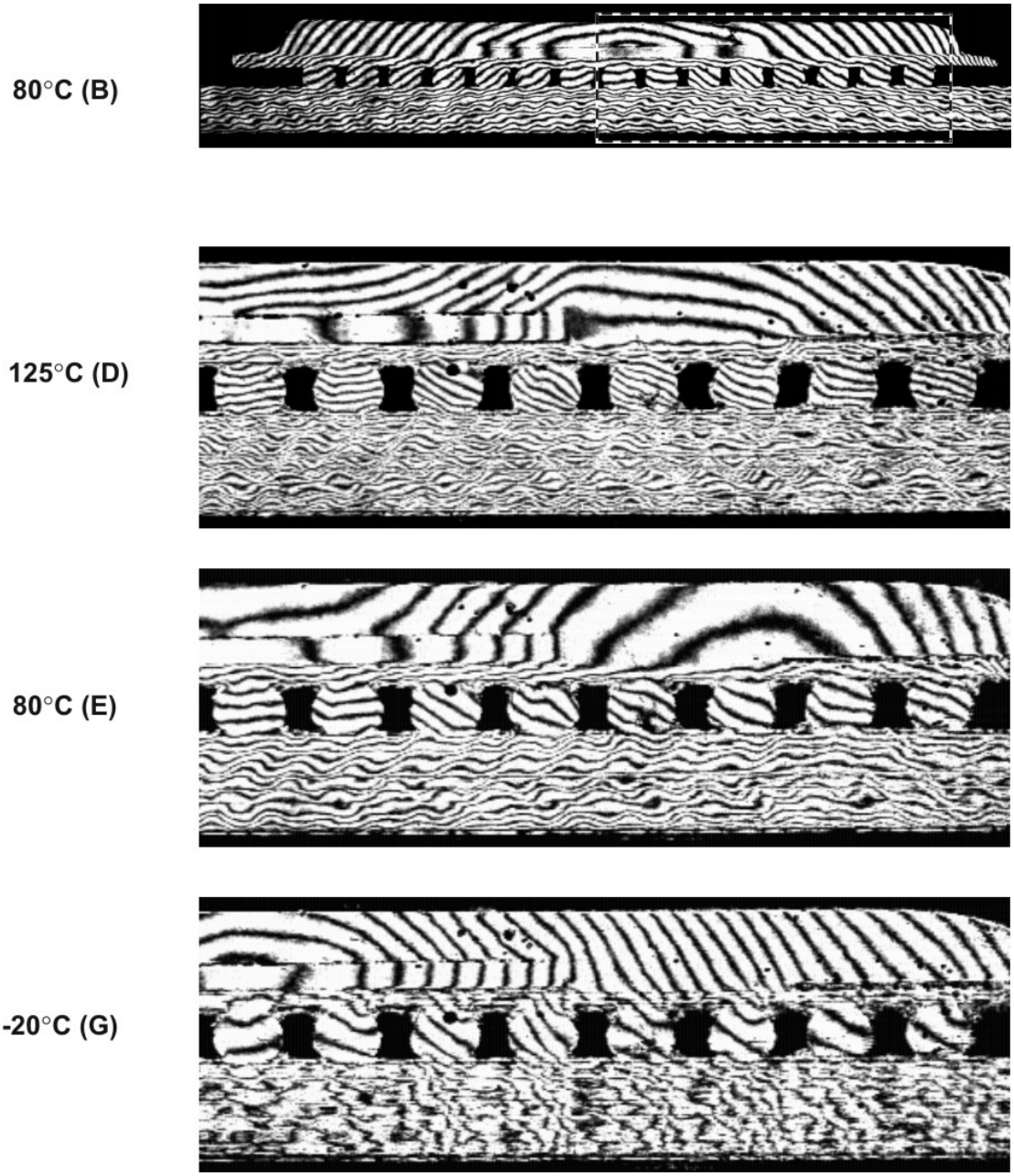

Figure 3-13 Representative (a) U and (b) V field fringe patterns produced by thermal loading

3.2.4 Results

3.2.4.1 Ben

The ben

line A-A’ in th

results are plott

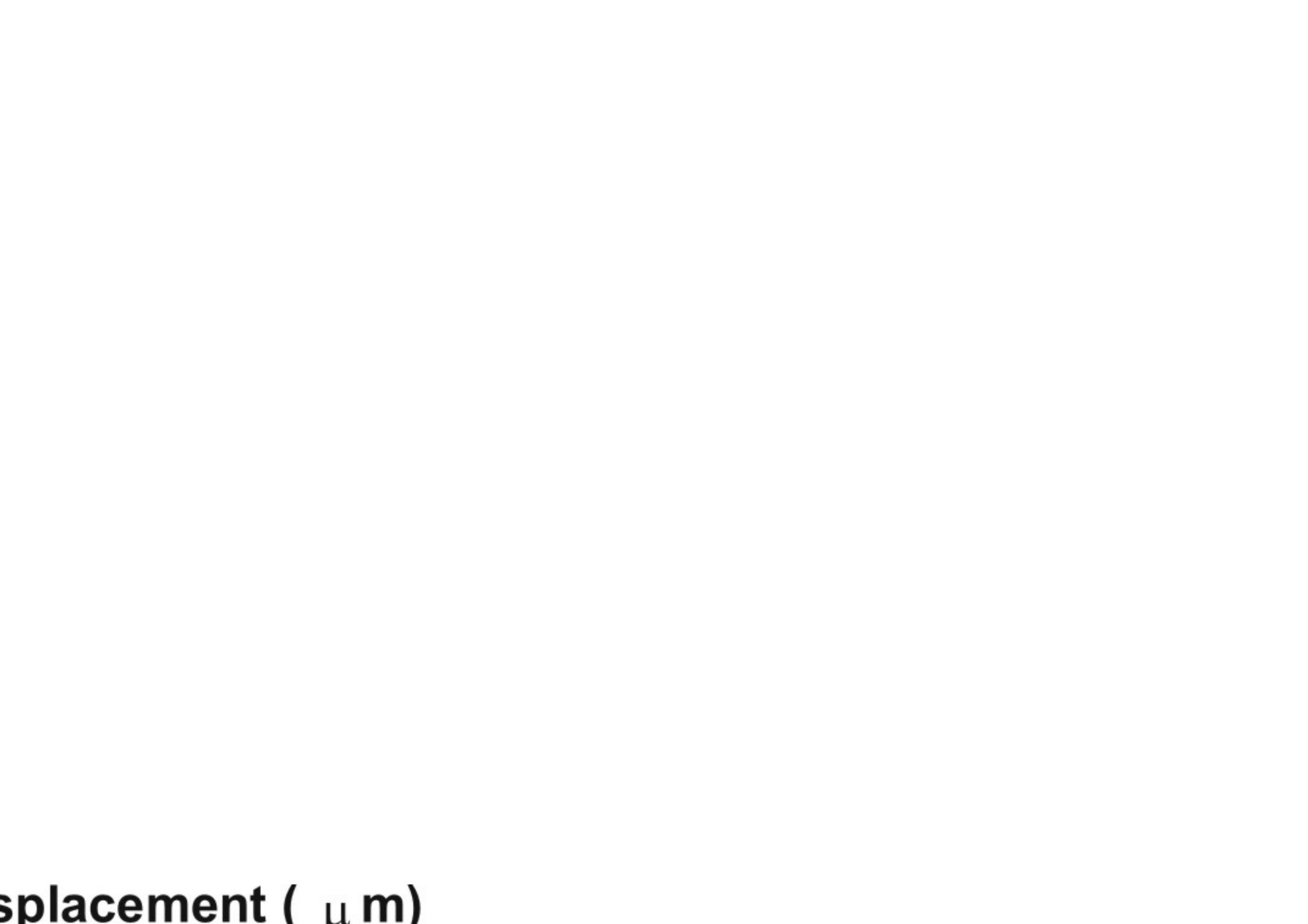
splacement (μm)

The molding co

downward afte

the bending di

effect of the chi

at 125°C chan

deformation o

conditions. These were calculated at the location between solder balls 6 and 7 (x = 9.75 mm from the center). In the case of mechanical loading, the tip displacement increased linearly until the bending moment reached 42.3 N·mm, and then increased at a much higher rate as the moment increased further.

In the case of thermal loading, however, the tip displacement increased linearly until the temperature reached 100°C, but decreased at 125°C. The bending displacement of the package increased at a rate of approximately 0.220 N·mm per 1°C before the solder balls relaxed, which was slightly less than that of 28.2 N·mm. During unloading (or cooling), the tip displacement decreased linearly at the same rate of the linear loading (or heating) region. As a result, the thermal cycle produced a permanent downward bending ($\cap$), while the mechanical loading cycle produced a permanent upward bending ($\cup$).

inal Strain, $\frac{\varepsilon_x}{|\varepsilon^{max}|}$

deformations re

were obtained

then calculated

The the

from the mecha

the chip and the

$|u_y|_{max}$

0.5

balls produced

opposite signs (

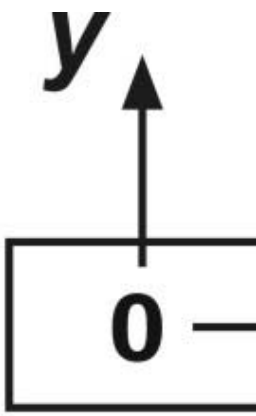

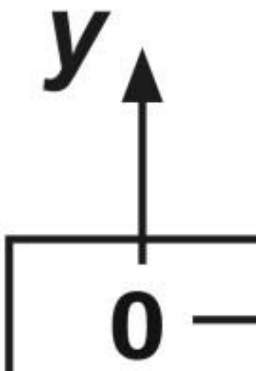

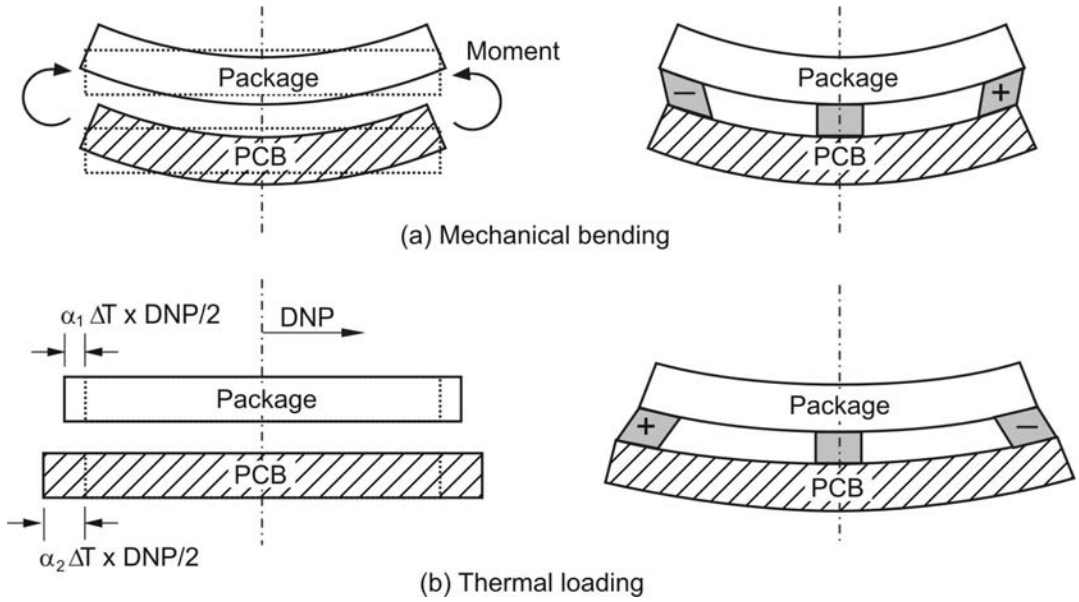

Figure 3-20 Schematic illustrations of the deformation mechanism of the package assembly

Chapter 4: Development of Conduction-based System

4.1 Introduction

The convection-based scheme presented in the previous chapter simulates the ATC condition and it has been employed to measure the *temperature-dependent* thermal deformations of real package assemblies subjected to various ATC conditions. With the convection oven, the ramp rate is limited and most of stresses usually relax during heating/cooling before the dwell begins at the maximum temperature as it happens during the actual ATC testing. For the fundamental study of *time-dependent* solder deformation, however, a system must provide a heating/cooling capacity with a much higher ramp rate and more accurate temperature control. A different scheme using thermal conduction is developed and implemented to achieve the necessary level of ramp rates and the required accuracy.

4.2 Mechanical/optical Configuration

A conduction-based environmental chamber is designed and implemented. Two distinct improvements over the conduction chambers in the literature [30-32], are (1) a wider temperature range and a faster ramp rate using a high power thermo-electric cooler (TEC) and (2) a uniform temperature distribution by using a vacuum environment and, thus, minimizing the convection heat loss.

The conduction-based system is shown in Figure 4-1 (a). A two-stage, high power thermoelectric cooler (TEC: TH200-2, Silicon Thermal) with a maximum power of 30 W is used as a heating/cooling device. The Silicon Thermal LB320 thermal controller was used to control the thermal head. The thermal head can provide temperatures ranging from –40 °C to 125 °C with a maximum ramp rate of 1.5 °C/s.

Since conduction is used to heat/cool the specimen, uneven temperature distributions can result from air circulation inside the chamber. More important, at cryogenic temperatures, humidity in the air can cause moisture to condense on the optical window and the specimen, which can reduce fringe visibility significantly. This undesirable effect was eliminated by creating a vacuum state inside the chamber. A mechanical pump was utilized to remove air from the chamber, which reduced the pressure of the chamber to 60 mm Hg (0.08 atm). This reduced pressure was maintained during the experiment.

Two fluid pipelines were needed to circulate a coolant (water) over the thermal head. If a small amount of water were to leak accidentally, it would evaporate instantly and condense on the specimen at low temperatures due to the low pressure of the chamber. Therefore, all water lines are secured with hose clamps to prevent possible water leakage. Six electric lines were needed for the low and high stages of the thermal head. All the lines were secured again by hoses, which were made airtight with an RTV sealant (Dow Corning 736).

The configurations of the water lines and electric lines are shown in Figure 4-1 (a). All the electric lines and water lines are delivered to the TEC through the back plate. An

air outlet was made on the back plate, which was connected to the mechanical vacuum pump during the experiment.

The configuration of the assembled environmental chamber is shown in Figure 4-1 (b). The front plate has a circular 4-inch diameter window for light illumination as well as observation of the specimen deformation. A silicon rubber gasket was inserted between the glass and the front plate to prevent air leakage. The pressure difference between the chamber and the outside was sufficient to hold the glass in place. All the surfaces of the chamber were sandblasted to eliminate undesirable specular reflections.

Unlike the convection-based scheme, the heating/cooling system did not create any vibration. Consequently, the rigid link between the specimen and the interferometer used in the convection-based system was not required. Instead, the interferometer and the chamber were fastened to the optical table to minimize relative motions between them.

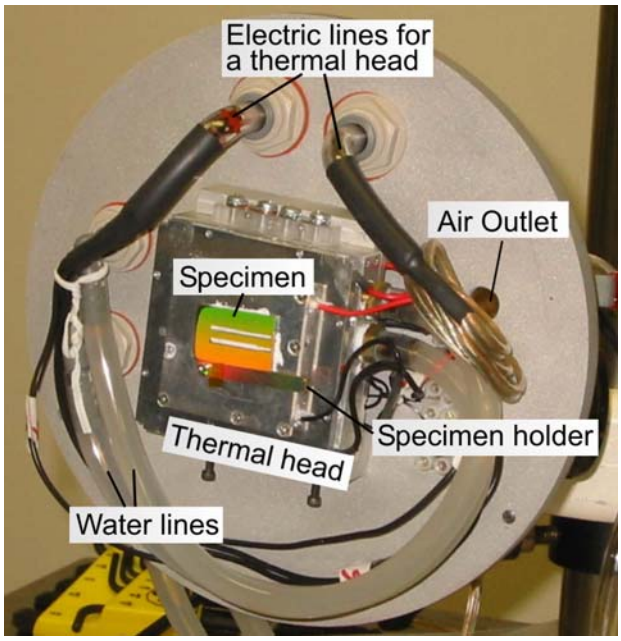

(a)

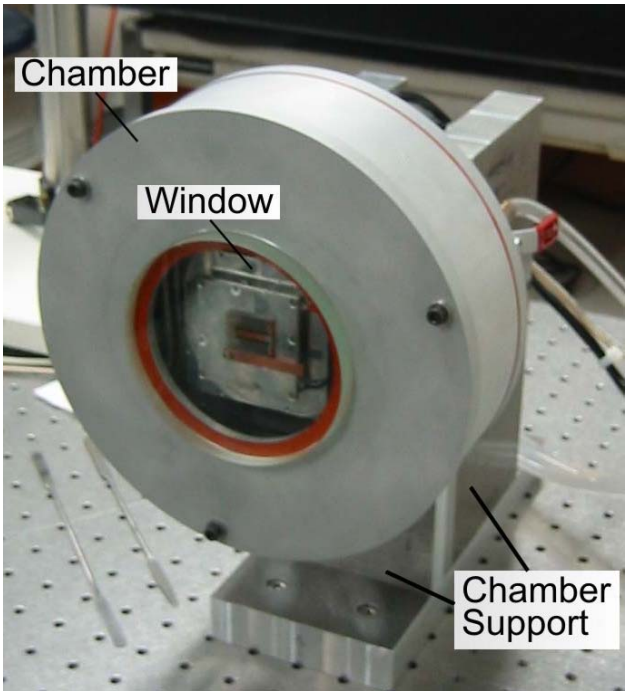

(b)

Figure 4-1 (a) Configuration of the chamber (b) Assembled chamber with a chamber support

4.3 Environmental Chamber Control

A T-type thermocouple was placed inside a small hole below the surface of the thermal head. The Silicon Thermal LB320 thermal controller changed the power of thermal head to achieve the target temperature. Commercial control software was employed to provide complex temperature profiles to the controller. The control panel is illustrated in Figure 4-2 (a). With the software, users can input multiple temperature cycles with diverse target temperatures, ramp rates, and dwell times.

In addition to temperature control thermocouples provided by the TEC manufacturer, two E-type thermal couples (5TC-TT-E-36-72, Omega Engineering, Inc.) were installed in the chamber to measure the temperature distribution of the specimen. They were connected to a data logger (34970A, Agilent Technologies, Inc) to record the temperature profiles during the experiment.

The air gap between the thermal head and the specimen reduces heat transfer from the thermal head to the specimen. Thermal compounds/greases were used to fill the gap. Two thermal compounds were tested: (1) thermal compound 120-2 from Wakefield Engineering, Inc., and (2) thermal grease G751 from Shin-Etsu, Inc. Their thermal conductivity were of 0.735 W/(m·K) and 4.5 W/(m·K), respectively. Although the grease had a much higher thermal conductivity, no apparent temperature differences on the specimens were observed as long as the layer of thermal interface was kept thin (~0.2 mm).

Figure 4-2 (b) shows the temperature profiles measured from the top of the thermal head and the specimen. The input temperature profile was (room temperature) to (100°C) to (–20°C) to (room temperature). The ramp rate was 1°C/s and the dwell time at the maximum and minimum temperature was 60 seconds. The temperature profile obtained from the experiment matches the input temperature profile extremely well in spite of the high ramp rate. The maximum temperature difference between two thermocouples was less than 1°C, which ensured temperature uniformity through the thickness of the specimen. A maximum ramp rate of 1.5 °C/sec was achieved, which was essential to observe the creep/relaxation behavior of the solder joint.

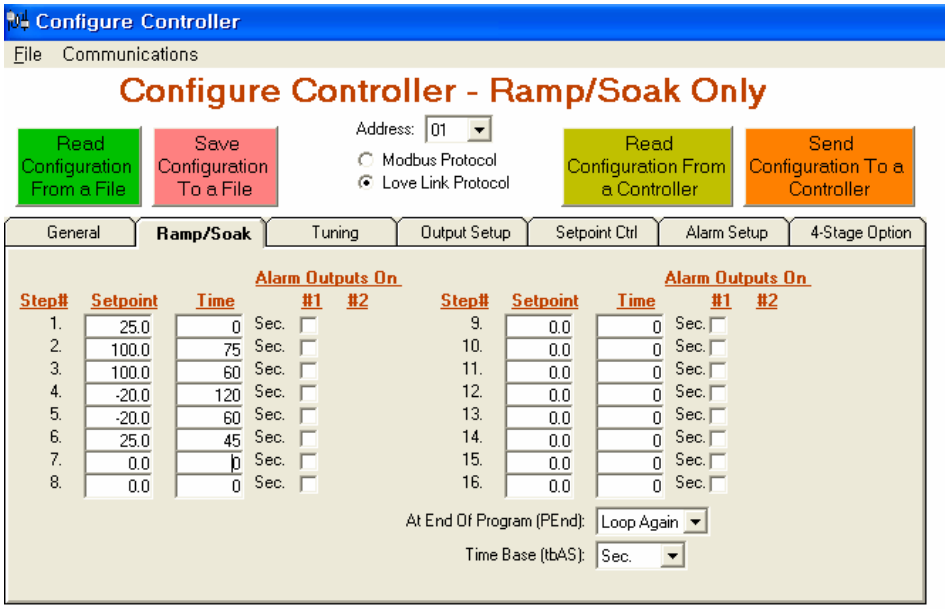

(a)

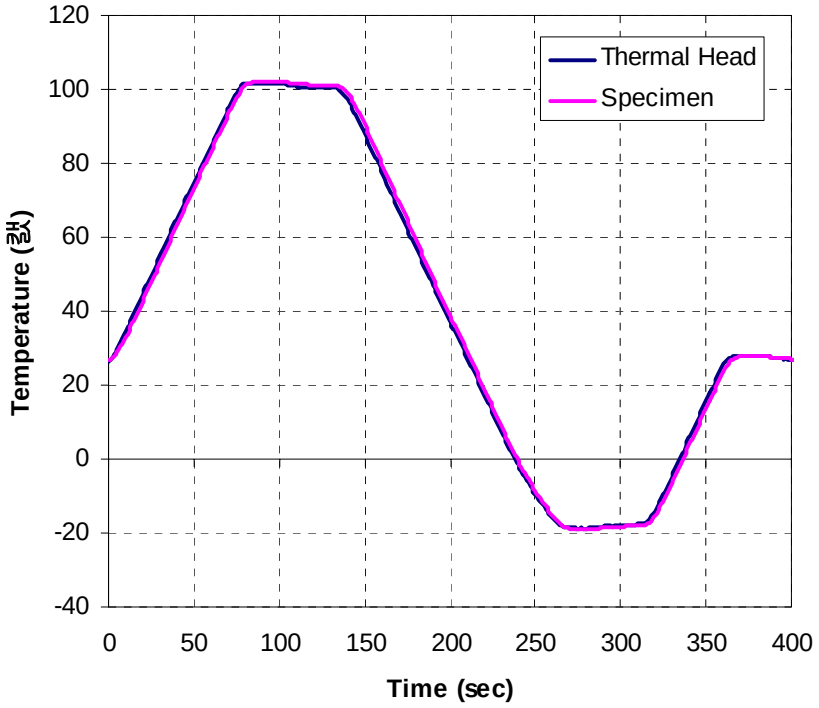

(b)

Figure 4-2 (a) Software for temperature control (b) Temperature profile measured from the top of the thermal head and the top of the specimen

4.4 Specimen Fixture

Four threaded holes were located on the top of the thermal head. A copper strip was installed with a screw on the thermal head, as shown in Figure 4-1 (a). The copper strip prevented the specimen from sliding downward. The high viscosity of the thermal compound/grease applied to the back of the specimen provided a sufficient friction force to hold the specimen during the experiment. Preliminary tests were conducted to ensure no accidental out of plane motion of the specimen during the thermal cycle.

4.5 Characterization of Testing Apparatus

Figure 4-3 shows the complete system combining the conduction-based chamber and the portable interferometer.

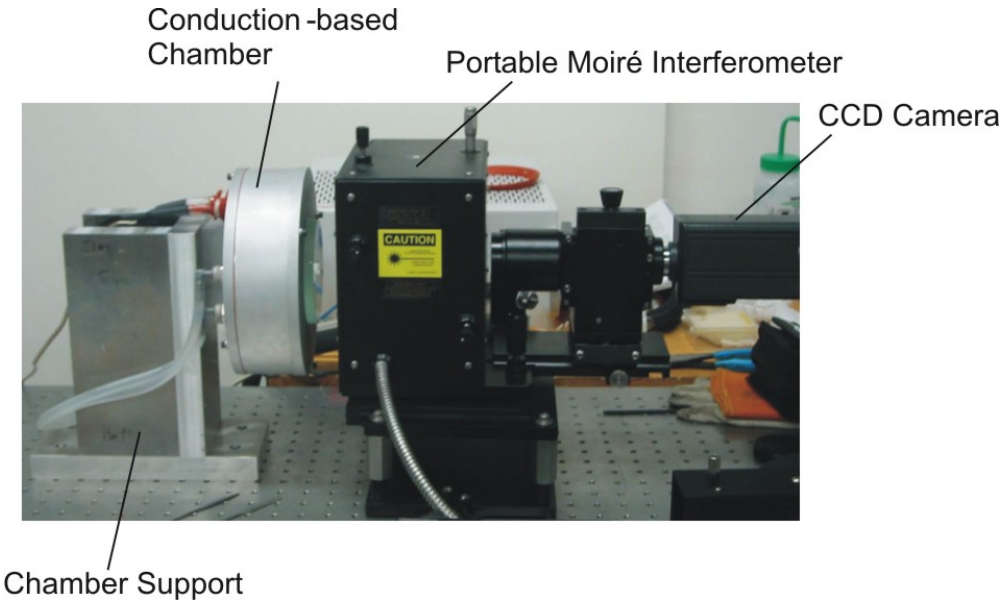

Figure 4-3 Configuration of test setup.

A preliminary experiment was conducted to investigate the stability and repeatability of the conduction-based system. The specimen was a copper strip fabricated from oxygen free copper (OFC 101). The fringe patterns were recorded continuously every five seconds. Temperature excursions varying from –20°C to 100°C with a ramp rate of 0.1 °C/sec and a 20 minute dwell time were used to measure the thermal expansion of copper. Figure 4-4 shows the temperature input to the controller and the temperature profile measured on the specimen throughout the temperature cycle. There is an excellent match between the two profiles.

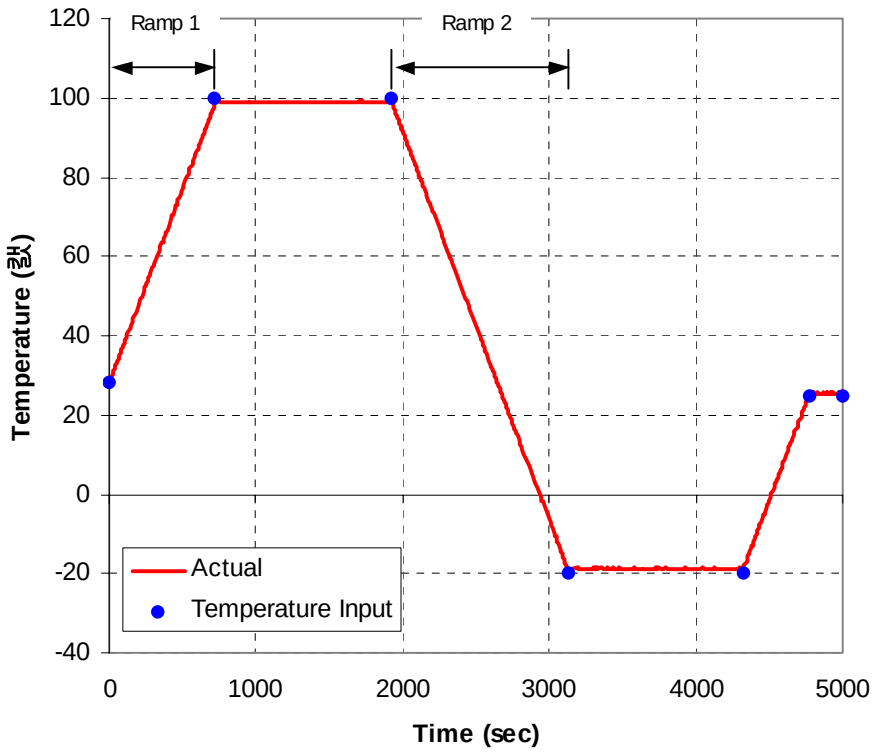

Figure 4-4 Comparison of temperature input to the controller and actual temperature of the specimen

The temperature stability of the experimental setup was investigated at the maximum temperature dwell. Figure 4-7 shows the temperature profile at the maximum temperature dwell. The average temperature during the span was 98.9 °C, which was 1 °C lower than the target temperature. The standard deviation was 0.09 °C and 95 percent of the temperature measurements were within two times of the standard deviation from the average temperature.

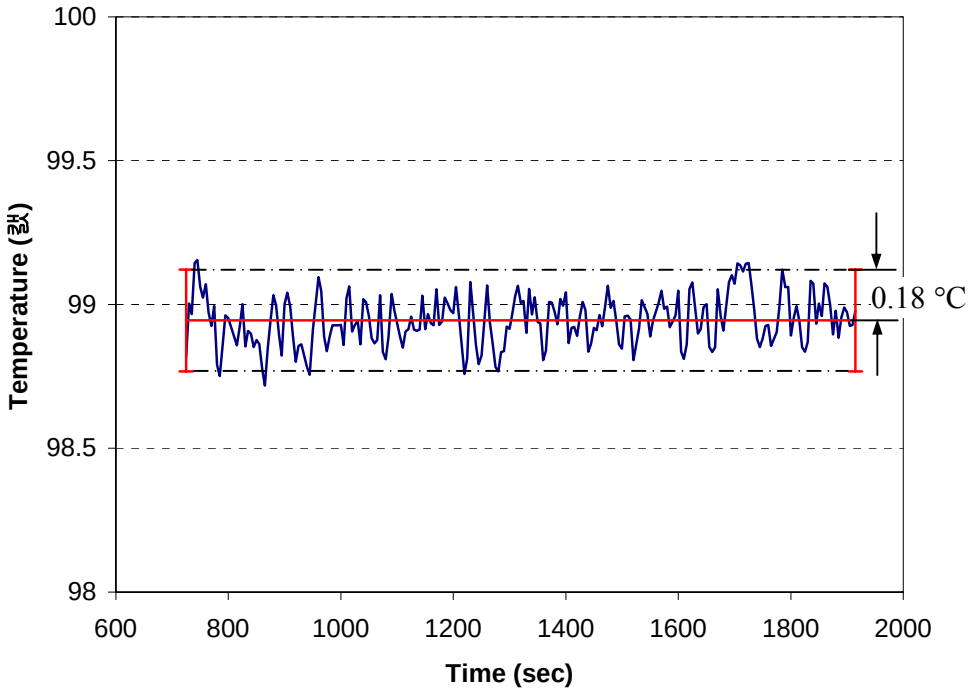

Figure 4-5 Temperature history at the maximum temperature dwell

Representative U field fringe patterns are shown in Figure 4-6. A time history of the thermal expansion of the copper strip is shown in Figure 4-7, which represents a free thermal strain. The CTE of the copper strip was determined from Eq. 2-4. The CTE

from 25°C to 100°C was determined to be 16.4 ppm/°C, which matched well with the values from the literature [72].

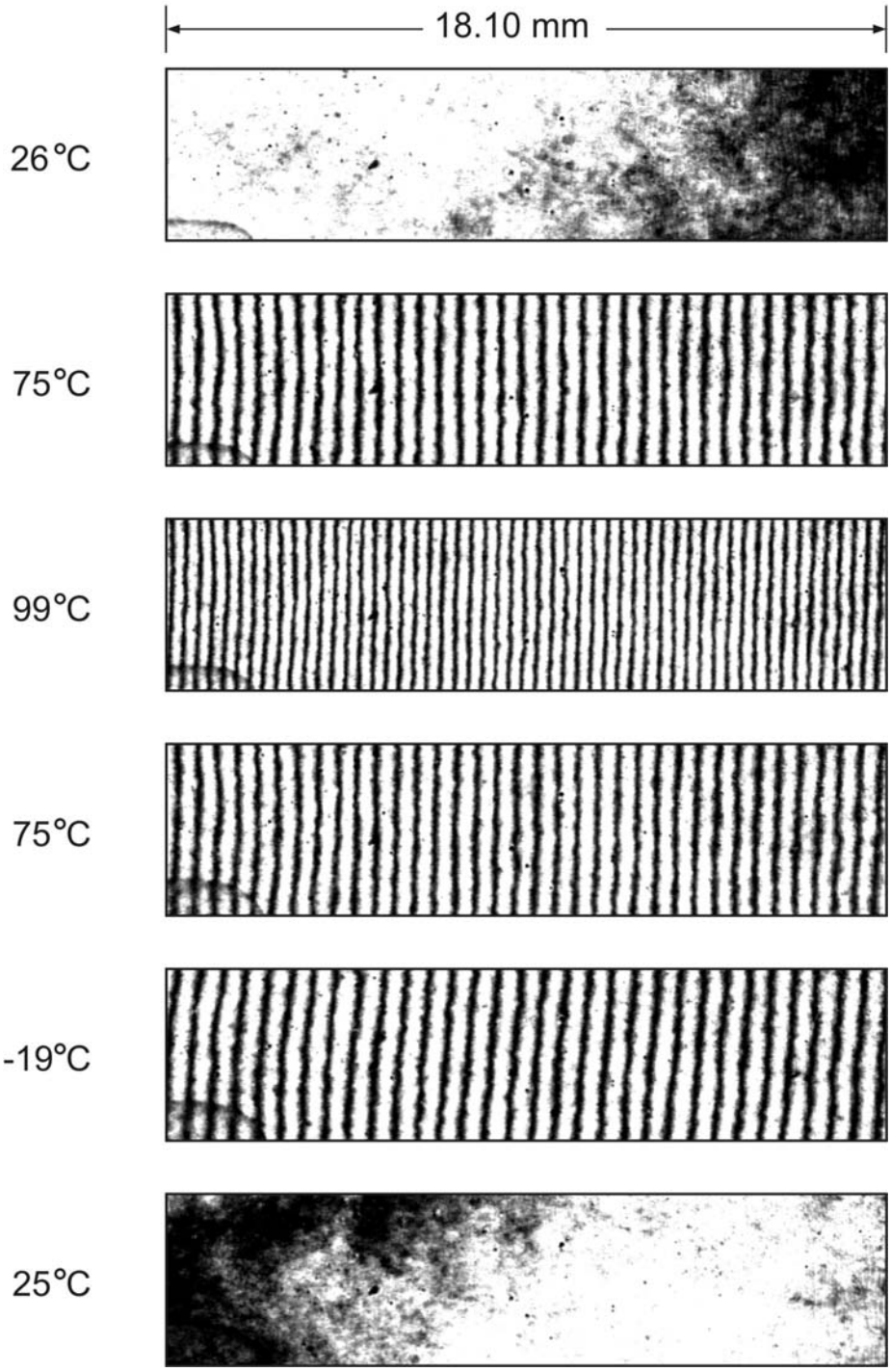

Figure 4-6 Representative U field fringe patterns

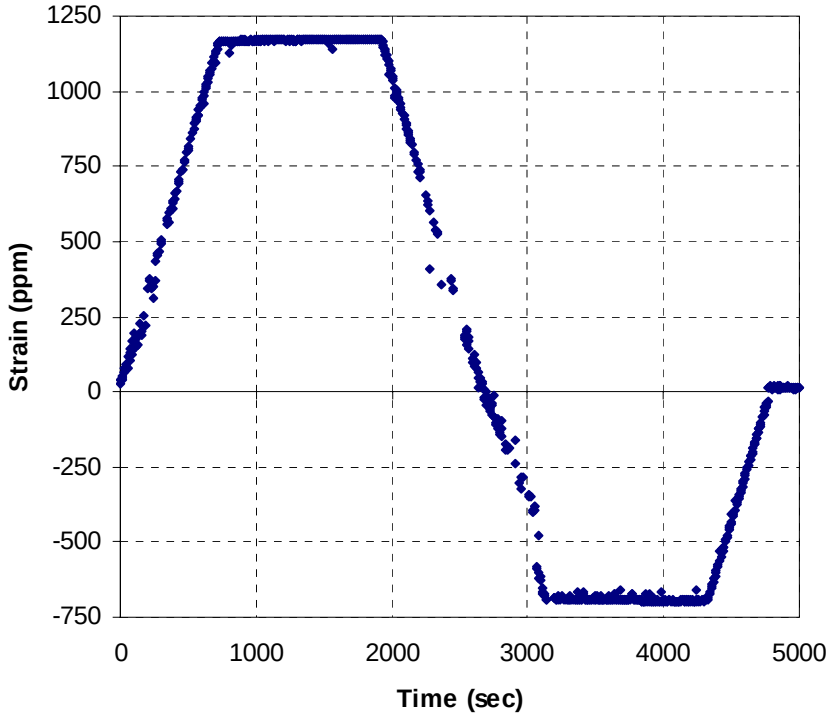

Figure 4-7 Time history of thermal expansion of the copper strip

4.6 Implementation: Illustration of ramp rate-dependent deformation

The conduction-based system was implemented to investigate the ramp rate dependent deformation of a Chip on Flex (COF) package. As shown in Figure 4-8 (a), the specimen was ground flat to expose the chip on both sides. It is to be noted that the package is attached to an Aluminum plate to simulate the actual operating condition. Temperature profiles used in the experiments are shown in Figure 4-8 (b). Two different ramp rates were applied; 1°C/sec and 0.01°C/sec. The temperature range was 0 to 100 °C.

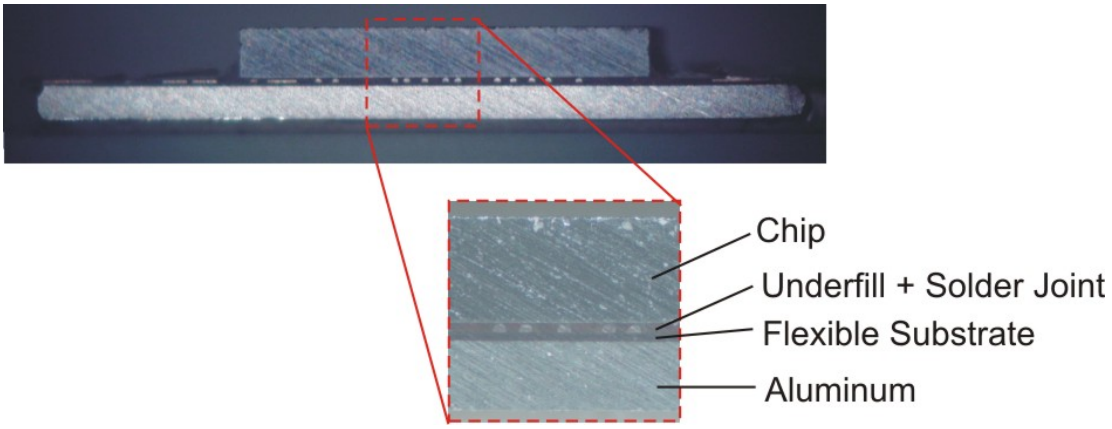

(a)

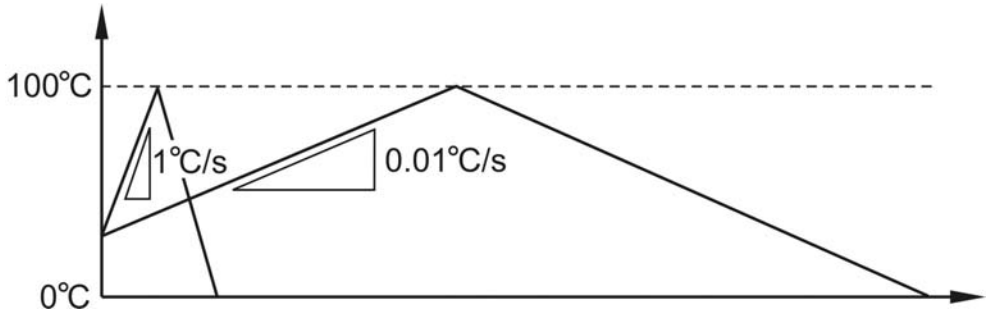

(b)

Figure 4-8 (a) Specimen Configuration (b) Temperature profile used for the experiments

The V field fringe patterns obtained from the experiments are shown in Figure 4-9. The chip bending displacements were calculated from the patterns and the results are plotted in Figure 4-10. When the assembly was heated to 100 °C, the aluminum expanded more than the chip, which produced an upward bending of the module (∪) and when the assembly was cooled down to 0 °C, the module bent downward (∩). The deformations were not much different at the maximum temperature (at 100 °C). However, the bending at the minimum temperature (at 0 °C) decreased approximately

25% when the slow ramp rate was used. The reduction of the bending displacement was caused by stress relaxation within the flex substrate and the underfill layer during cooling.

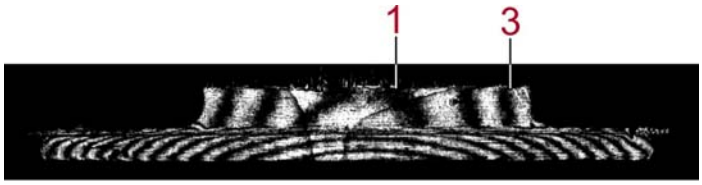

Ramp rate = 1°C/s

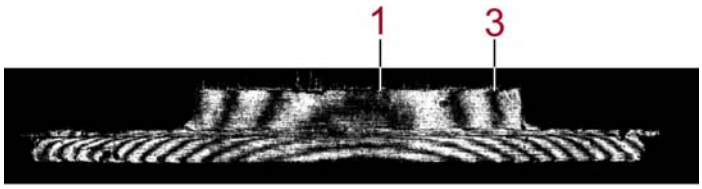

Ramp rate = 0.01°C/s

(a)

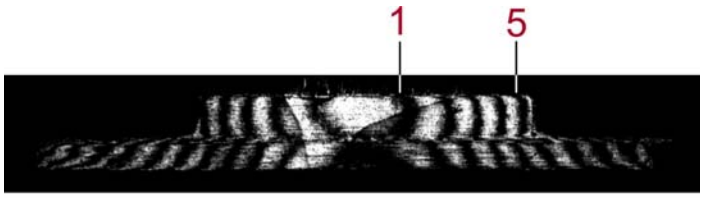

Ramp rate = 1°C/s

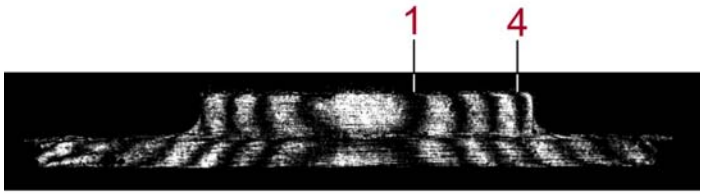

Ramp rate = 0.01°C/s

(b)

Figure 4-9 (a) V field fringe patterns at 100 °C (b) V field fringe patterns at 0 °C

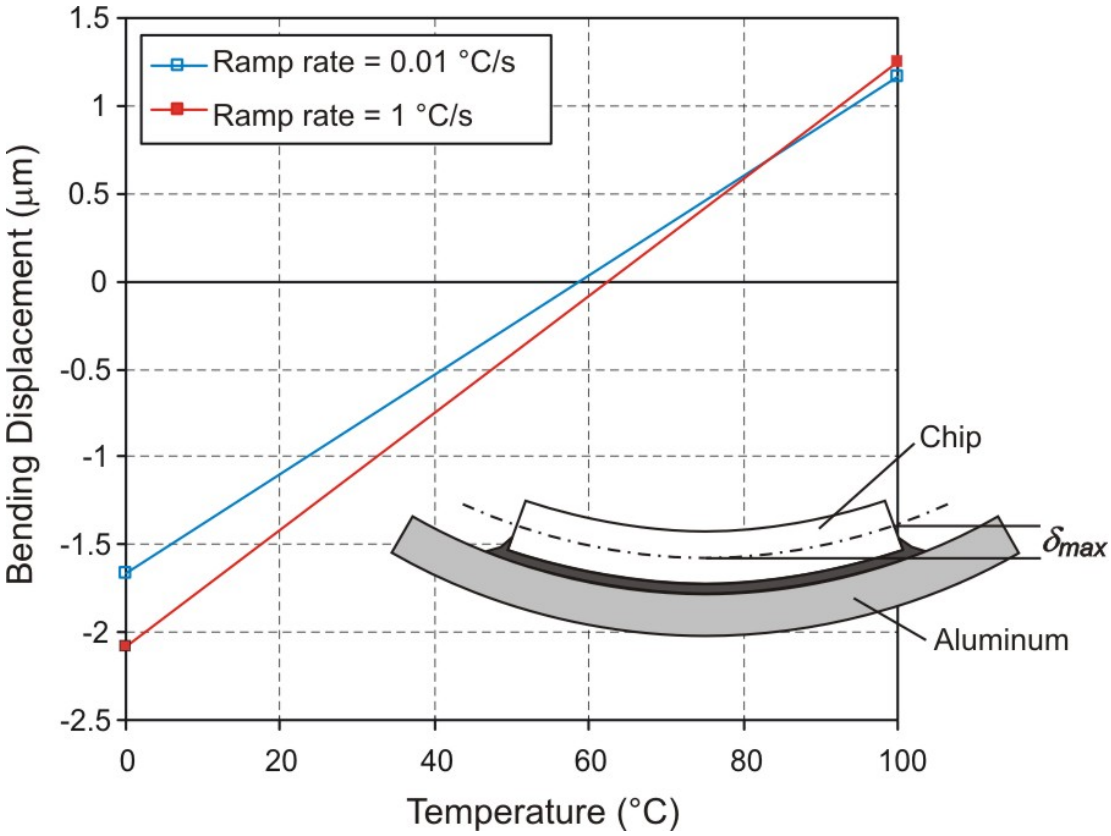

Figure 4-10 Bending displacements along the chip.

Chapter 5: Application of Conduction-based System

5.1 Introduction

Eutectic and near eutectic Pb/Sn solder alloys are most commonly used interconnect materials in microelectronic packaging. Thermal cycling causes thermo-mechanical deformations in electronic assemblies, resulting in fatigue damage of surface mount interconnects. In recent years, numerous fatigue damage models have been proposed. They include strain-based approaches such as the modified Coffin-Manson model, and energy-based approaches such as the energy-partitioning model and the total energy based model (or the unified model).

The fatigue life predictions are typically calibrated using failure data obtained from thermal cycling tests, where the results from the stress models are used in the damage models to predict the fatigue life. In this calibration process, uncertainties in the stress model are often compensated in the damage models and vice-versa. This interdependency of the two models has limited the applicability of the stress models within the scope of the actual accelerated thermal cycling test, i.e., specific package architectures and specific test conditions. As a result, expensive and lengthy failure tests are required when the models are to be used for new package assemblies.

This chapter proposes a novel specimen configuration that produces a virtually *pure shear* condition for a solder joint subjected to a thermal cyclic loading. The deformation of the joint is measured quantitatively using moiré interferometry while heating and cooling it by the setup implemented in the last chapter. The results are used

to verify the validity of the constitutive properties of solders, and subsequently to improve the accuracy and generality of the properties.

5.2 Design and Implementation of the New Specimen

5.2.1 Review of Previous Research

The relationship between stress and strain for solder is a very complex one and is dependent on many parameters; temperature, deformation rate, strain history and microstructural condition being the most prominent. Many experiments are conducted under isothermal conditions to determine the properties of solder. As compared to the constitutive equations of the solder joint in isothermal conditions, a limited number of experimental results from thermal cycling conditions are reported. The experimental results under thermal cycling conditions can be categorized in two types: thermal cycling of actual components and thermal cycling of simplified test specimens.

Hall determined shear strain hysteresis loop in actual solder joints for leadless ceramic carriers (LCCs) soldered to printed-wiring boards (PWBs) [47]. In his experiments, strain gauges were employed to measure the mechanical strains in both the components and PWBs and the shear stress and strain of the solder joint were determined from these strains. A difficulty associated with this testing method is that the strain and stress states in the actual solder joints are quite complex. Lau, et al. used two- and three-dimensional nonlinear finite element analysis for surface-mounted joints and found that even in a single joint, for any given displacement, there was a complex state of tension, compression, and shear [68]. The thermal cycling of actual components does not permit

the meaningful measurement of solder joint mechanical properties. Even if mechanical properties were measured, the complex strain nature of the joints would make the analysis very difficult.

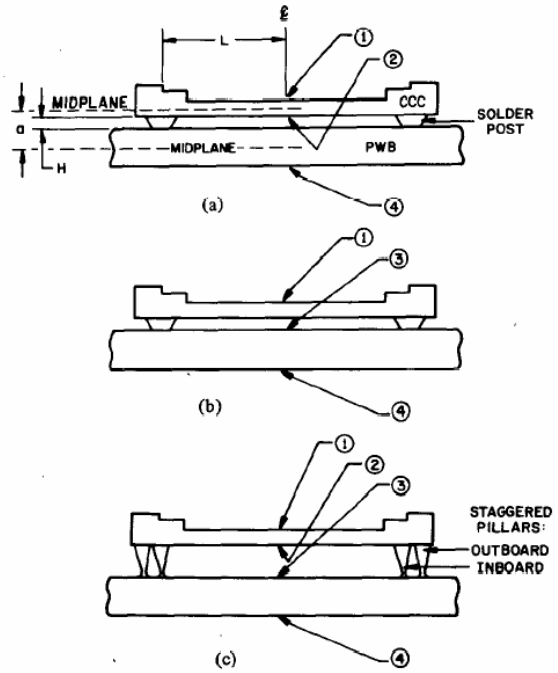

Figure 5-1 The specimen used in Hall's experiment. Numbers indicate the positions where strain gauges were applied [47].

Several experiments were conducted to measure inelastic strain accumulation at the solder joints in actual plastic package assemblies subjected to thermal cycling [65,66]. Actual plastic packages are composed of many dissimilar materials with temperature and time dependent properties. Their material properties depend on the temperature profile applied to the packages and accurate temperature profiles are difficult to achieve with convection oven. In addition, the geometry of the solder joints is changed destructively by cross sectioning the specimen, which changes the deformation of the solder joints drastically. Thus, it is extremely challenging to estimate the forces acting on the solder joint in actual package assemblies by means of analytical or finite element analysis.

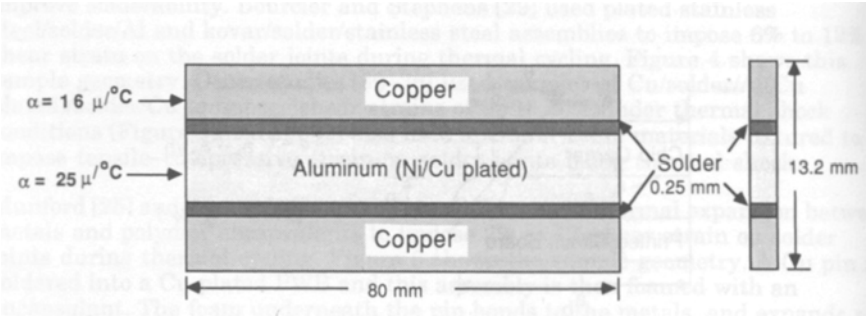

(a)

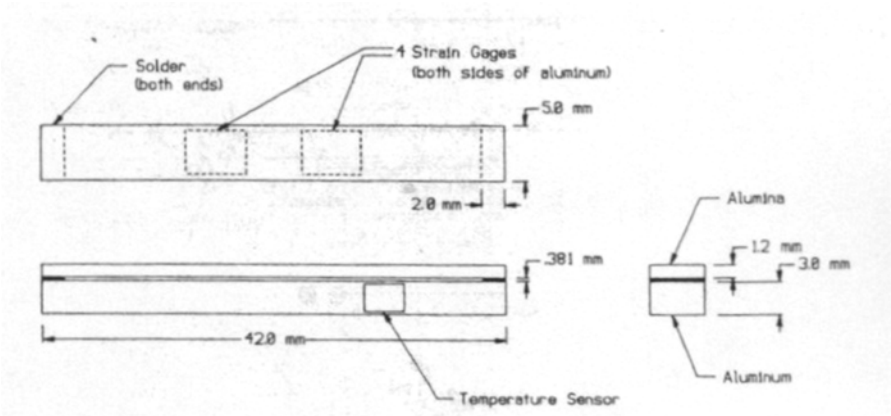

(b)

Figure 5-2 Schematic configurations of (a) Frear's specimen [50, 51] (b) Pao's specimen [11,12]

To overcome the limitations on the testing of actual packages, simplified test specimens were used to avoid the problem of complex strain distributions in actual component assemblies. The state of strain in the solder joints was simplified. Frear used an aluminum plate sandwiched between two copper plates by solder layers, as shown in Figure 5-2 (a) [50, 51]. Thermal loading ranging from –55 °C to 125 °C was applied to the specimen. However, his main interest was to investigate how the microstructures of

the solder evolved during thermal cycle instead of characterizing the mechanical behavior of solder joint during thermal cycling [50,51].

Pao and et al. also conducted an experiment with a simple geometry specimen made of alumina (Al_2O_3) and aluminum (Al2024-T4) as shown in Figure 5-2 (b) [11, 12]. The stress/strain hysteresis response of the solder joints was determined. Four strain gauges were attached to the aluminum beam and the strain at the solder joint was estimated from the strains measured by the gages. It was assumed that the magnitude of the solder joint rotation was small compared to the magnitude of the shear strain at the solder joint. Due to this limitation, the shear stress at the solder joint could not be determined accurately, since the joint became much stiffer at the cryogenic temperatures. In addition, due to the large local CTE mismatch between solder and alumina, the uniform strain at the solder joint could not be achieved, either.

A new specimen configuration is required to verify and validate the existing constitutive equations of solder. A new specimen must consist of well-characterized materials and should be able to apply a uniform loading on the solder joint. An accurately controlled temperature profiles were needed to characterize thermomechanical behavior of the solder joint, but the ramp rate and accuracy of the temperature profile were limited by the inherent limitations of the convection-based heating/cooling mechanism. Previously, the deformation at the solder joint was estimated from the strains measured at the joined structures [11, 12, 47]. However, the strain at the solder joint is not uniform due to the local CTE mismatch between the solder joint and joined materials. In addition, an off the mark prediction can result from the large rotation of the solder joint. A more direct and accurate measurement technique is required.

5.2.2 Configuration of the Specimen

A new specimen was designed and implemented to investigate the thermo-mechanical behavior of the solder joint. The configuration of the new specimen is shown in Figure 5-3. It is similar to the double lap shear configuration. A symmetric configuration was employed to minimize the bending of the specimen and to apply a uniform loading on the solder joints.

Copper (OFC 101) and Steel (AISI 1018) were used to fabricate the specimen. The material properties of the two materials are well known and their properties can be found in Ref. [69]. The copper part and the steel part were brazed together by very thin silver braze alloy (BAg-3, 50Ag15.5Cu15.5Zn16Cd3Ni). The melting temperature and flow temperature of the silver braze alloy are 1170 °F (632 °C) and 1270 °F (688 °C), respectively. Proper silver-brazed joints have the strength of the adjoined materials up to the temperature of 300 °F (150 °C) [61], which ensures the integrity of the specimen during the thermal loading. The size of the solder joint is 1 mm (width) x 1 mm (height) x 2 mm (depth).

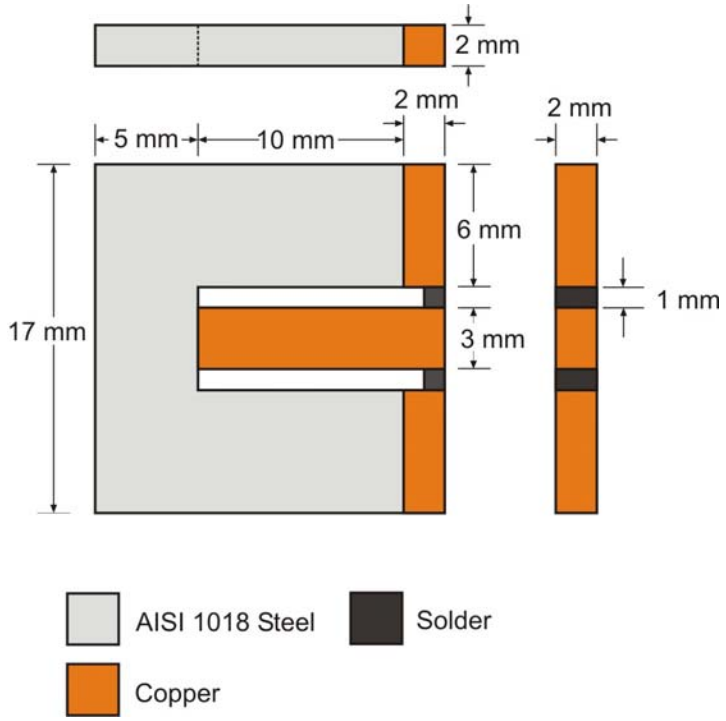

Figure 5-3 Specimen schematic

The CTE difference between copper and steel produces deformations at the solder joint when the specimen is subjected to temperature cycling. As illustrated in Figure 5-4, a negative shear strain was resulted at the upper solder joint when the specimen was heated. The local CTE mismatch between the solder joint and other components was minimized by using copper at the top and bottom of the solder joint. The conduction-based system was ideal to heat/cool the specimen because of the high thermal conductivity of the constituent materials. The CTE difference between the solder and the copper is small (5~7 ppm) and the fringe patterns at the interface were clearly visible.

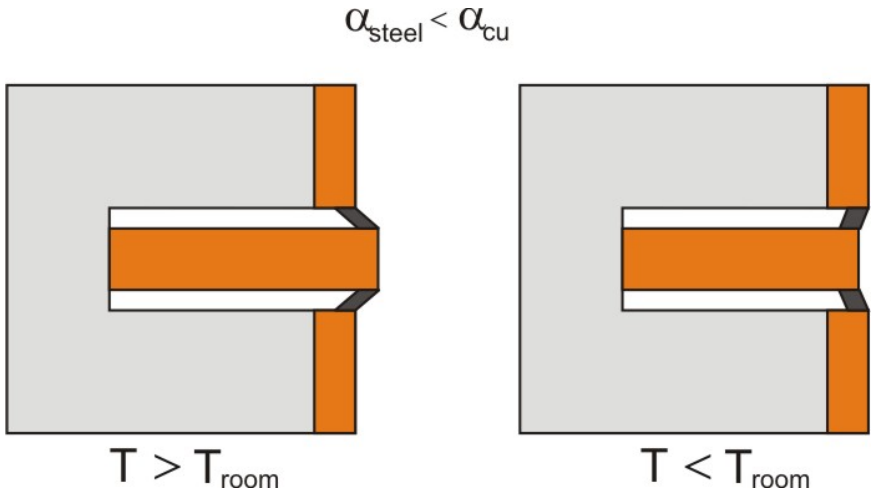

Figure 5-4 Solder deformation during the thermal cycle

The features of the proposed specimen configuration are summarized in Table 1.

Previous specimens configuration (Pao, Hall)	New specimen configuration
Bending dominant • Large peeling stress results from the curvature difference. • Complex stress state exists.	Shear dominant • Other stresses are minimized by incorporating a symmetric configuration. • Resistance to bending is maximized by increasing the height of the steel beam.
Large local CTE mismatch at the top and bottom of the solder joint.	Local CTE mismatch was minimized by using copper at the top and bottom of the solder joint.
Complex geometry of the solder joint.	Controlled (rectangular) geometry of the solder joint

Table 1 Advantages of new specimen configuration over previous specimen configuration

5.2.3 Fabrication

The fabrication process of the specimen is shown in Figure 5-5. High accuracy in fabricating the specimen was necessary to apply symmetric loading at the top and bottom solder joint during the temperature cycling. In order to maintain the required accuracy for the experiment, wire electro-discharge machining (wire EDM) was used extensively.

A steel block and a copper block were brazed together with a silver braze. After the two blocks were joined, the boundaries were trimmed and slots were cut with a wire EDM machine. The brazed structure was sliced every 2 mm to make a thin specimen. Microstructures of solder are important factors in determining mechanical properties and they vary with temperature profiles used in the reflow process [62]. An actual reflow temperature profile used in the industry was applied using the Quad ZCR reflow oven (Precision Placement Machines, Inc.) shown in Figure 5-6 (a). Easy Profile 256 solder paste (Kester) was used with a temperature profile shown in Figure 5-6 (b). After solder reflow, the specimen was ground to remove protruding solder. Finally, the excess solder was trimmed by the wire EDM machine to make a square solder joint of 1 mm by 1 mm. Since the wire EDM machine can be used only for electrically conductive materials, fluxes had to be cleaned with a flux cleaner before the final trimming process to prevent accidental chipping of the specimen.

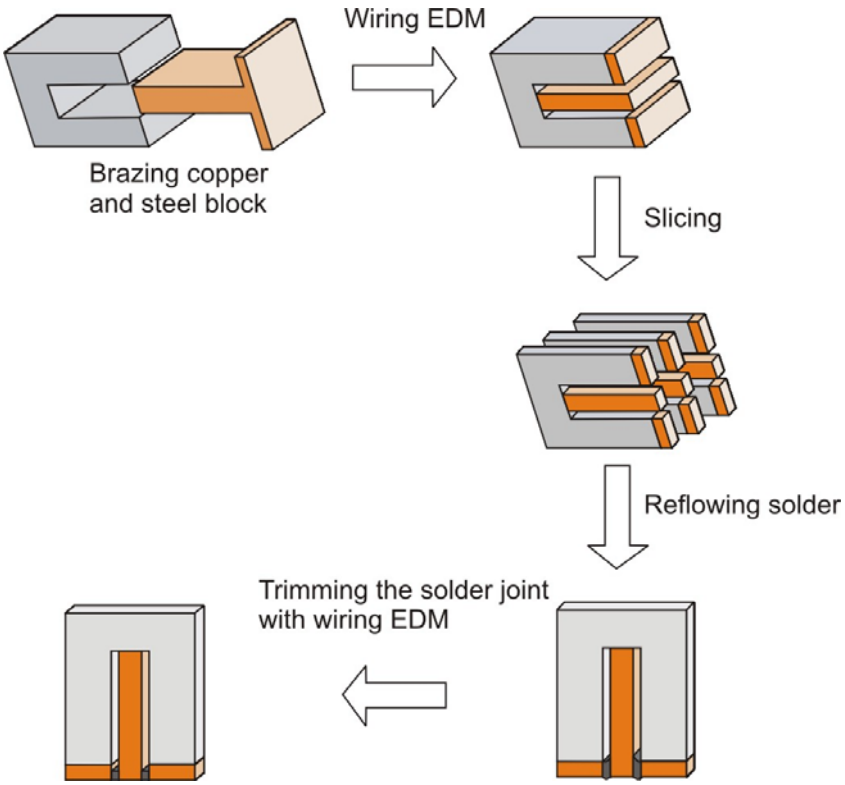

Figure 5-5 Specimen Fabrication Process

The specimen before and after the reflow process is shown in Figure 5-7. The controlled geometry of the solder joint is evident.

(a)

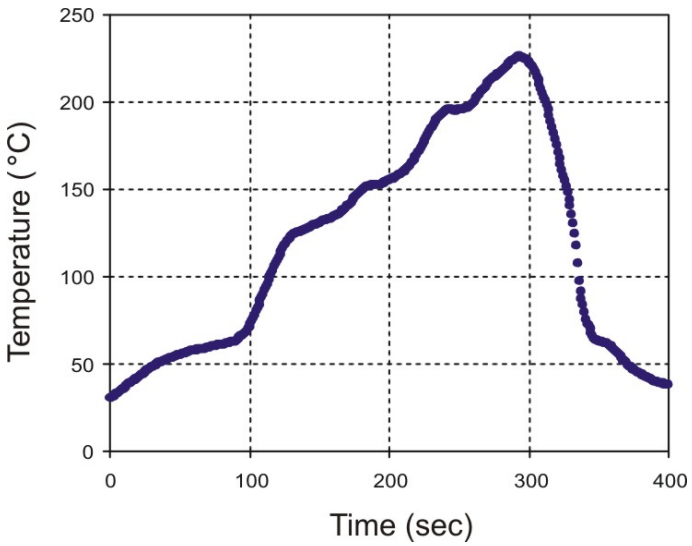

(b)

Figure 5-6 (a) Reflow machine used to fabricate the specimen (b) Reflow temperature profile

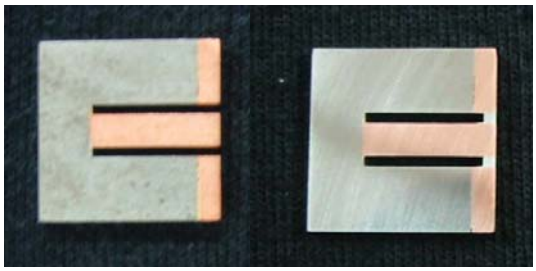

Figure 5-7 Specimen configuration before and after reflow of solder

5.3 Experiments

The test setup discussed in the previous chapter was used to document thermomechanical behavior of the solder joint. The advantages of this experimental technique are shown in Table 2.

Previous test setup (Pao, Hall)	New test setup
Strain measurement on the constituent materials • Deformation at the solder joints was estimated from the measured strains at the constituent materials. • Rotation at the solder joint was assumed small.	Direct measurement of the deformation at the solder joint • Rotation of the solder joint is structurally minimized. • The effect of rotation is removed by taking U and V field fringe patterns together.
Convection heating/cooling • Accurate temperature profile was not achieved • Ramp rate was limited.	Conduction heating/cooling • Accurate temperature profile is achieved. • A temperature profile with a much higher ramp rate (1 ºC/s) is achieved.
Point measurement • The effect of the local CTE mismatch on the solder joint with the constituent material was not determined.	Whole field measurement • The deformation of the whole specimen is determined. • The deformation of the solder joint at the interface is determined.

Table 2 Advantages of new test setup over previous test setup

The specimen was ground flat with 800-grit sand paper and replicated with a 1200 lines/mm diffraction grating. The initial null fields obtained at the room temperature are shown in Figure 5-8 (a). The temperature input and temperature profile obtained from the experiment are shown in Figure 5-8 (b). The input temperature profile was (room temperature) to (100 °C) to (–20 °C) to (room temperature). The ramp rate was 1 °C/s and the dwell time at the maximum and minimum temperature was 20 minutes. It took about 45 minutes for one complete temperature cycle. Multiple temperature cycles were applied to investigate the accumulated inelastic deformation at the solder joint. Four phase-shifted images were taken at every five seconds for analysis. At the maximum and minimum temperatures, both U and V field fringe patterns were recorded to obtain deformations at the solder joint.

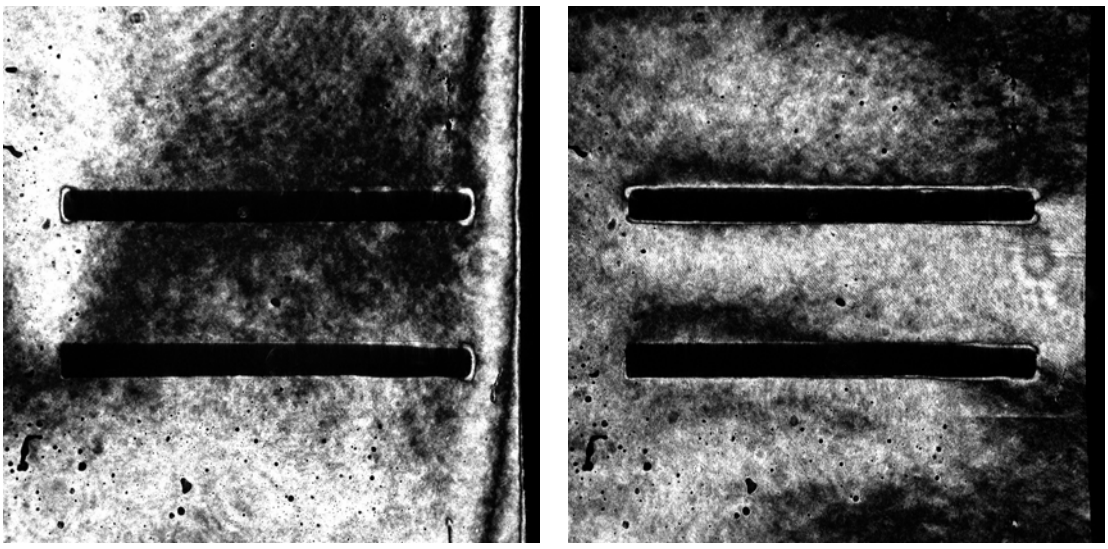

U field **V field**

(a)

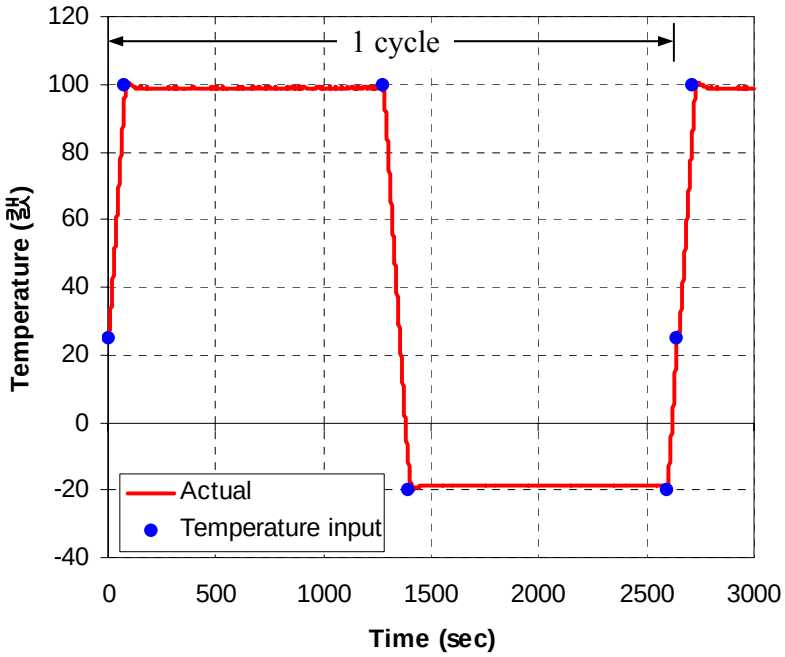

(b)

Figure 5-8 (a) Initial null field obtained at room temperature (b) Temperature input and actual temperature of the specimen.

Figure 5-9 shows U and V field fringe patterns at the start of dwell at 100 °C. Symmetric fringe patterns about the center of the specimen were obtained. Even at the interface between the solder joint and the copper beam, well-defined fringe patterns were obtained. All fringe patterns at the start and end of dwell can be found in the appendix.

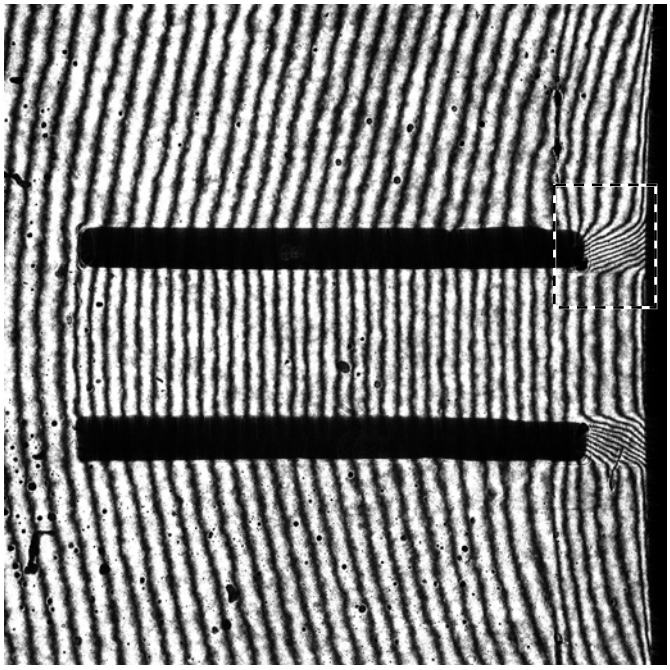

U field

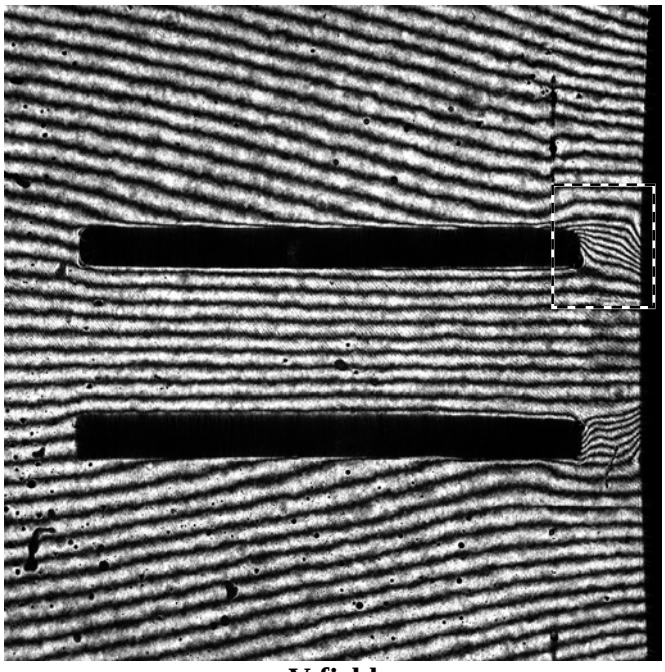

V field

Figure 5-9 U and V field fringe patterns at the start of 100 ºC dwell

Fringe patterns were analyzed using the software developed by the LOMS lab of UMD [58]. Four phase-shifted images are used to calculate the displacements. Figure

5-10 shows the displacement contours in the rectangular region marked in Figure 5-9. Since the displacements were determined with high accuracy, the shear strain at the solder joint was calculated with the software. Figure 5-11 shows the shear strain distribution at the solder joint. It is interesting that the maximum shear strain at the solder is located at the center of solder joint not at the interface. This is distinctively different from the strain distribution at the solder joint of actual electronic packages, where maximum strain occurs at the interface of a solder joint with a substrate or a PCB.

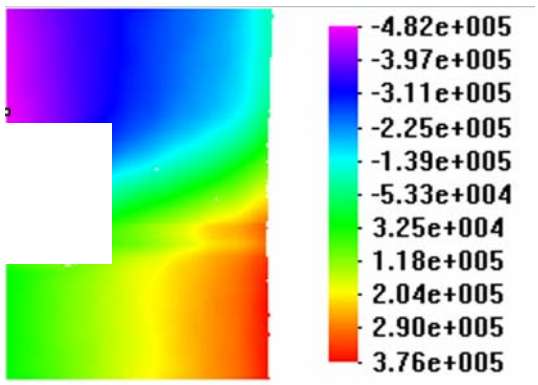

U displacement (unit: nanometer)

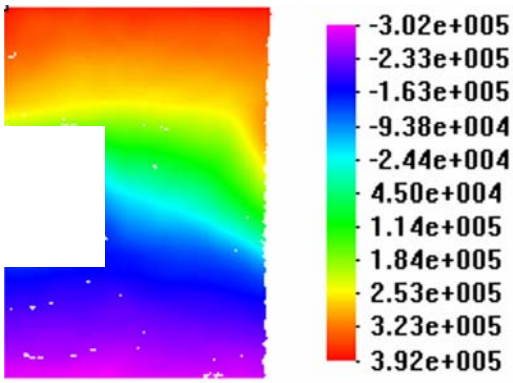

V displacement (unit: nanometer)

Figure 5-10 U and V displacement plot of the region shown in Figure 5-9

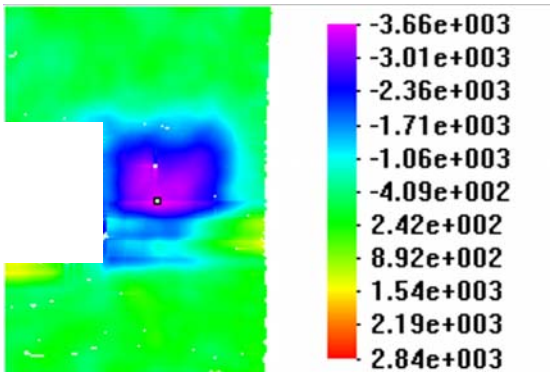

Figure 5-11 Shear strain distribution of the region shown in Figure 5-9

5.4 Constitutive Properties of Solder

5.4.1 Unified Constitutive Model: Anand Model

The deformation behavior of solder is dependent on temperature and time. Therefore, the deformation of solder can be described by time-dependent constitutive laws of viscoplasticity or time-dependent creep combined with time-independent plasticity. In viscoplastic deformation, the elastic region is bounded by a static yield surface in a stress space, and all inelastic deformations are time-dependent. The inelastic deformations occur at all non-zero stress values. The viscoplastic constitutive law does not distinguish plastic strains from strains caused by creep. Unlike the time-independent plasticity law, the viscoplastic constitutive law does not rely on an explicit yield surface and the loading and unloading criterion. Instead, it utilizes an internal state variable, representing the resistance of the material to inelastic deformations. Creep deformation

is time and temperature dependent, and the time-independent plastic deformation results in plastic strains depending on the yield surface and loading and unloading criterion.

There is no commonly accepted constitutive law for describing the behavior of solder. Furthermore, published material data vary significantly in various sources. Among the various time-dependent constitutive laws for solder joints, the viscoplastic constitutive law introduced by Anand [70] is frequently used due to its easy implementation.

Anand's model consists of two coupled differential equations that relate the inelastic strain rate to the rate of deformation resistance. The following form of the flow equation was selected to accommodate the strain rate dependence on the stress

$$\dot{\varepsilon}_P = A\exp\left(-\frac{Q}{RT}\right)\left[\sinh\left(\xi\frac{\sigma}{s}\right)\right]^{1/m} \tag{5-1}$$

In addition, the evolution equation for the internal variable s is given as

$$\dot{s} = \left\{h_0\left|1-\frac{s}{s^*}\right|^a \cdot sign\left(1-\frac{s}{s^*}\right)\right\}\cdot\dot{\varepsilon}_P \tag{5-2}$$

Where

$$s^* = \hat{s}\left[\frac{\dot{\varepsilon}_P}{A}\exp\left(\frac{Q}{RT}\right)\right]^n \tag{5-3}$$

The descriptions of the nine parameters used in Anand model are shown in Table 3. The numerical values of these parameters for eutectic solder alloy were determined by Darveaux [42], Ye et al [45,46] and Wang, et al [43,44]. These values are shown in Table 4.

Parameter	Description	Units
s_o	Initial deformation resistance	Stress
Q/R	Ratio of activation energy to universal gas constant	1/temperature
A	Pre-exponential factor	1/time
ξ	Stress multiplier	Dimensionless
m	Strain rate sensitivity of stress	Dimensionless
h_o	Hardening/softening constant	Stress
$\hat{s}$	Coefficient for deformation resistance saturation value	Stress
n	Strain rate sensitivity of saturation value	Dimensionless
a	Strain rate sensitivity of hardening or softening	Dimensionless

Table 3 Material Parameters for Anand Model [72]

Parameter	Darveaux [42]	Ye, et al [45,46]	Wang, et al [43,44]
S_o (MPa)	1 (dimensionless)	50.40	56.33
Q/R (K^{-1})	8110	6966	10830
A (s^{-1})	9.62e4	3.862e4	1.49e7
ξ	8.7023e-2 (1/Mpa)	5.0	11
M4	.303	.2845	.303
h_o (MPa)	1e-9 (dimensionless)	30.11e3	2640.75
$\hat{s}$ (MPa)	1 (dimensionless)	122.7	80.42
N	1e-9 (dimensionless)	.002	0.0231
A	1 (dimensionless)	1.8	1.34

Table 4 Anand constants used in the finite element analysis

5.4.2 Partitioned Model

In this model, the total strain ε is the sum of an elastic strain, time-independent plastic strain, and time dependent plastic strain (creep) as

$$\varepsilon = \varepsilon_e + \varepsilon_p + \varepsilon_c \tag{5-4}$$

where

$$\varepsilon_e = \frac{\sigma}{E} \tag{5-5}$$
$$\varepsilon_p = C_p \sigma^m$$
$$\dot{\varepsilon}_c = C_1 \left[\sinh \cdot \left(C_2 \sigma \right) \right]^{C_3} e^{\frac{-C_4}{T}}$$

The time independent elasto-plastic material properties were taken from Ref. [35,36]. Garofalo's steady state creep model was employed and the constants were taken from Ref. [34] (Table 5).

Constant	218°C	398°C
C_1	1239.5	255.95
C_2	0.053523	0.14197
C_3	3.3	3.3
C_4	6359.5	6359.5

Table 5 Constants for Garofalo model [34]

Another partitioned model was also available in the literature. Partitioned model incorporating kinematic hardening was reported in ref. [37]. The creep was modeled by a double power creep model shown in Eq. 5-6.

$$\dot{\varepsilon}_c = C_1 \sigma^{C_2} e^{-\frac{C_3}{T}} + C_4 \sigma^{C_5} e^{-\frac{C_6}{T}} \quad 5\text{-}6$$

The constants used in the model are shown in Table 6. Two power law terms were implemented into ANSYS by using parameters of a primary and a secondary creep model.

	C_1	C_2	C_3	C_4	C_5	C_6	σ	T
Unit	s^{-1}	-	K	s^{-1}	-	K	MPa	K
Value	0.4	2	5400	21	7	9500	-	-

Table 6 Parameters for double power creep model [37]

Constants for multilinear kinematic hardening are shown in Table 7.

	ε_1	ε_2	σ_1	σ_2	σ_3	E
Unit	-	-	MPa	MPa	MPa	GPa
280 K	7e-4	3e-3	21	41	600	29
320 K	7e-4	3e-3	19	31	200	

Table 7 Parameters of the elastic-plastic model [37]

5.5 Analysis: Uniformity of shear stress

The first numerical analysis was conducted to investigate the validity of the proposed specimen configuration. Figure 5-12 shows the conventional shear specimen configuration, the proposed specimen configuration and the corresponding FEM models.

The unified approach was used for the solder to incorporate time and temperature dependent deformation of the solder joint. The temperature profile shown in Figure 5-8 (b) was applied to both the specimens and the results are compared in Fig. 5-14. The shear stress distributions at the solder joints at the beginning of dwell at 100ºC and –20ºC are shown in Figure 5-13(a) and (b), respectively. More uniform shear stress was observed at the solder joint of the new specimen configuration during temperature cycling.

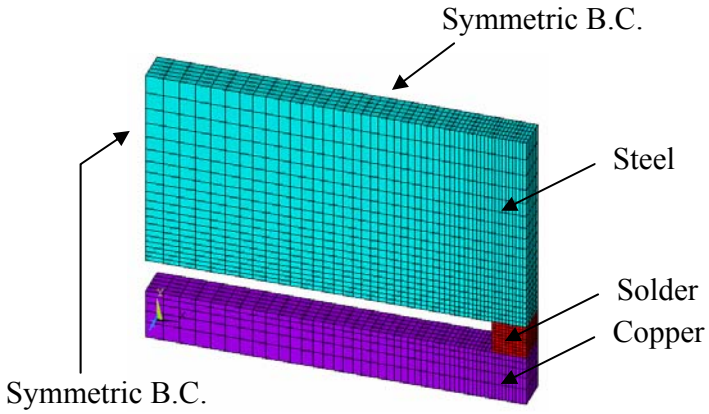

(a)

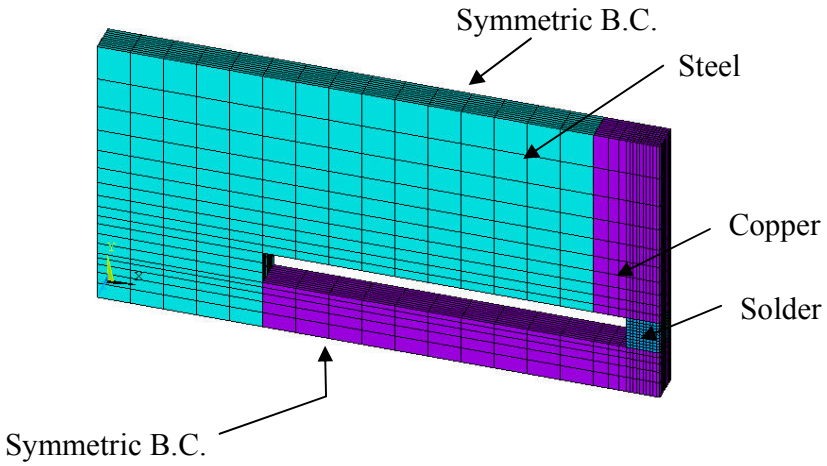

(b)

Figure 5-12 Finite element meshes for (a) symmetric specimen (b) conventional specimen

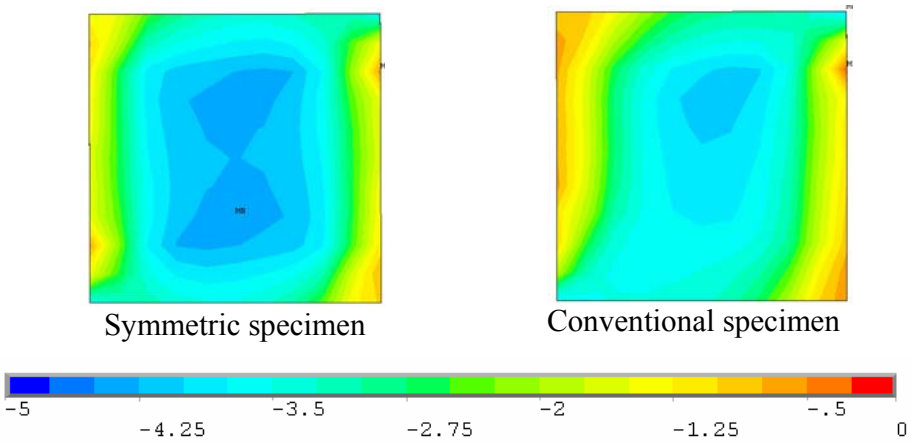

(a)

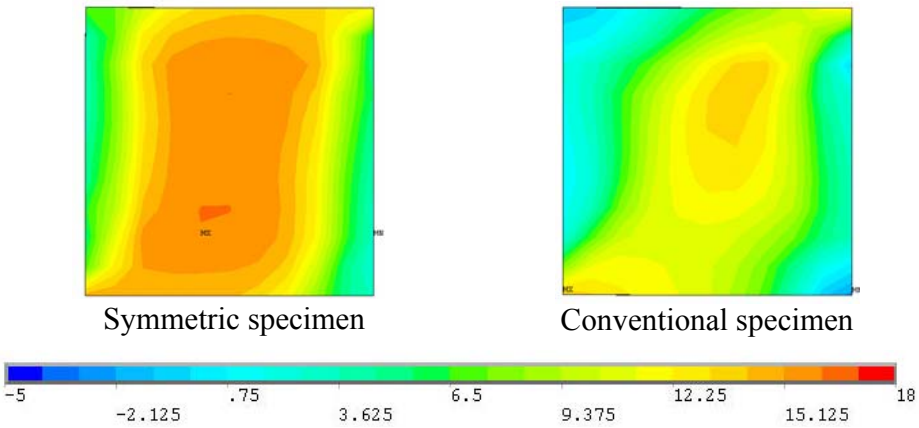

(b)

Figure 5-13 (a) Stress distribution at the start of 100 ºC dwell (b) Stress distribution at the start of -20 ºC dwell (unit: MPa)

To investigate the complexity of the stress distribution at the solder joint, stress distributions along the center of the solder joints are plotted in Figure 5-14. For the proposed specimen configuration, the shear stress was dominant and the magnitudes of other stress components were very small. In contrast, the magnitude of σ_{yy} was comparable to or even larger than the magnitude of shear stress when the conventional specimen configuration was used.

It is interesting to note that the magnitude of the maximum shear stress was nearly identical for both configurations. With the proposed, however, a uniform shear stress was observed over the large area of the solder joint. This provided a large gage length in experiments and it was another important advantage of the proposed configuration for validation of constitutive properties using moiré interferometry.

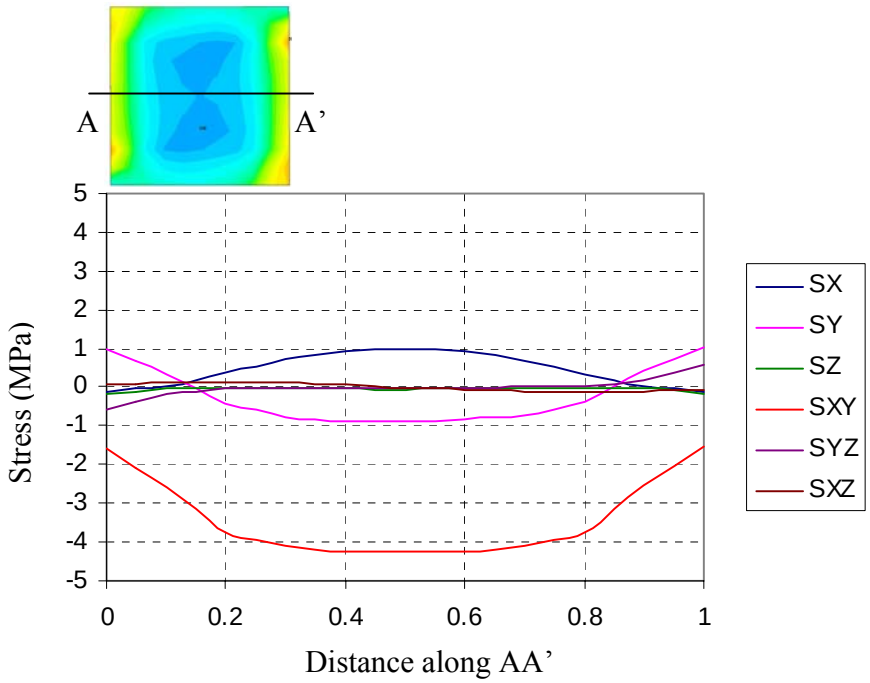

(a)

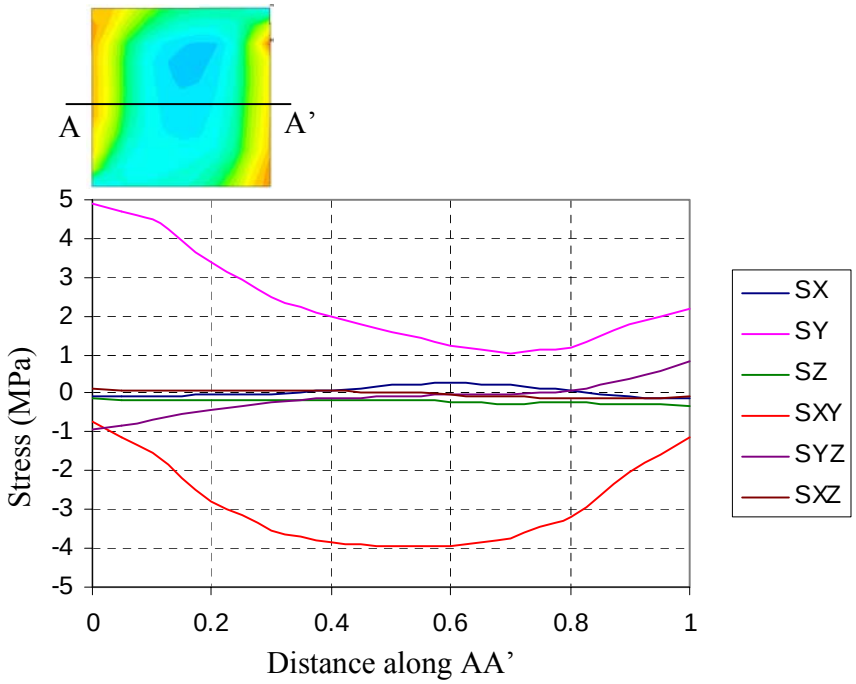

(b)

Figure 5-14 Stress distributions along AA' (a) for the symmetric specimen (b) for the conventional specimen

5.6 Analysis: verification of constitutive properties

An extensive finite element analysis was conducted to verify the validity of the existing constitutive properties of eutectic SnPb solder. Except for the model employing the double power creep model, the steel and the copper beams were modeled using element SOLID185. Element SOLID107 was used for the unified solder constitutive property. Element SOLID 185 was used for the partitioned model employing Garofalo's creep model. For the model employing the double power creep model, element SOLID45 was used to incorporate the primary and secondary creep. The temperature dependent material properties of copper and steel are shown in Table 8 [69]. The Anand constants used in the model are shown in Table 4 [43]. A quarter model was employed due to symmetry about the xz plane and the yz plane.

	AISI1018	Copper
E (GPa)	207	114.0-0.0449*T (°C)
ν	0.29	0.34
α (ppm/°C)	11.57+0.01494*T (°C)-1.739E-5*T^2 (°C)	16.28+0.01144*T (°C)-1.064E-5*T^2 (°C)

Table 8 Elastic properties used for the steel and copper [69]

The shear strain at the center of the solder joint was extracted from the experiments and they were compared with the numerical predictions. The shear strain histories are shown in Figure 5-15.

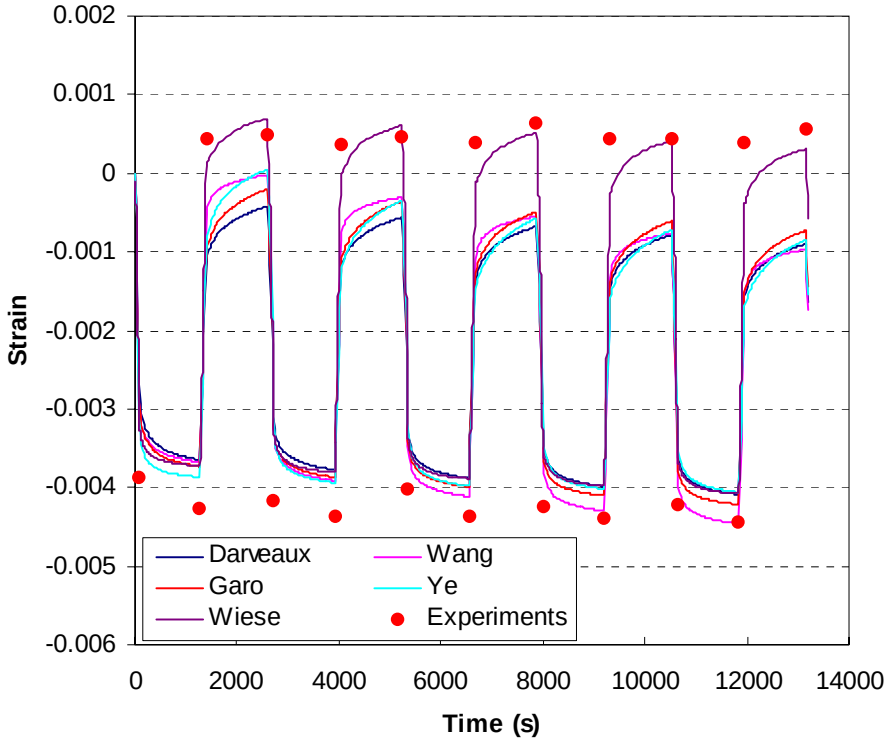

Figure 5-15 Shear strain history from the experiment and FEA

Shear strain obtained from the experiments was always larger than the shear strain obtained from the finite element analysis. It should be noted that when the temperature was cooled down to -20°C, the shear strain at the solder joint became positive as determined by the experiment. At low temperatures, shear strain obtained from Wiese's double power creep model predicted the values obtained from the experiment closely. It is interesting that as the number of cycles increase, the whole strain ranges from finite element analysis are shifted to the negative direction. However, the minimum and maximum shear strains obtained from the experiments were almost constant. As a result,

after five cycles, the minimum shear strains calculated from the finite element analysis were close to the value obtained from the experiment.

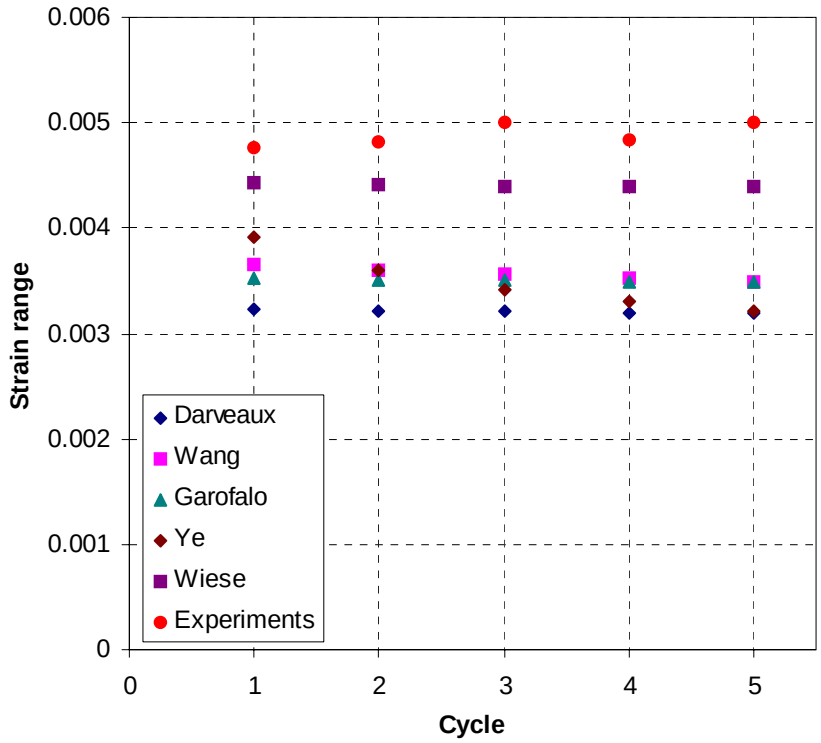

Figure 5-16 Shear strain ranges per cycle

Figure 5-16 shows the shear strain ranges per each cycle. The shear strain ranges obtained from the experiment and the FEA are almost constant in each cycle except the result employing Ye's Anand constants. It decreased as the number of cycle increased. The shear strain ranges obtained from the experiments were always bigger than the shear strain ranges calculated from the finite element analysis. The shear strain range obtained from finite element analysis employing Wiese's double power creep model was similar to the result determined from the experiment.

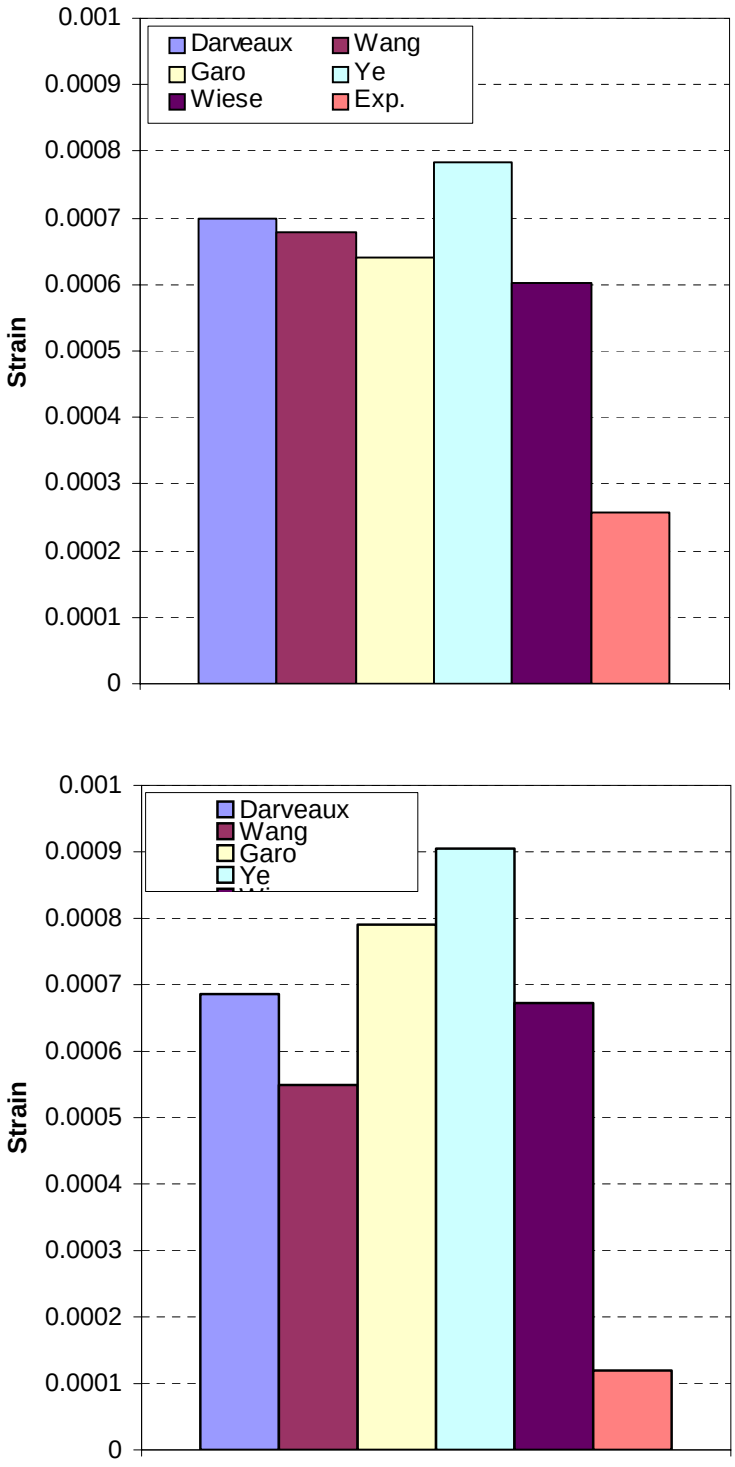

Figure 5-17 Shear increment at the dwell (a) at the maximum temperature (b) at

the minimum temperature

Figure 5-17 shows the shear strain increment at the dwell period at the maximum and minimum temperatures. The magnitude of the strain increases due to the relaxation of the solder joint during the dwell period. Finite element analysis predicts that the shear strain increment at minimum temperature is of same magnitude as that at the maximum temperature. This should be ascribed to the fact that creep strain depends on the temperature as well as the magnitude of the stress. At the low temperature dwell, stress applied to the solder joint is much higher, thus creep strain increment at the low temperature dwell is large. Finite element analysis employing solder constitutive models from Garofalo, Ye and Wang, the strain increment at the minimum temperature dwell is even larger than the strain increment at the maximum temperature. By contrast, almost no strain increment was observed from the experiment at the low temperature.

Chapter 6: Conclusions and Suggestions for Future Research

6.1 Conclusions

Two experimental apparatuses using moiré interferometry was developed to characterize the thermo-mechanical behavior of solder joints. A compact moiré interferometer was combined with environmental chambers to allow real-time observation of non-linear and time-dependent solder and solder assemblies.

The major contribution made by this thesis include:

- An apparatus based on convection heating and cooling was developed and implemented to simulate the accelerated thermal cycling condition for electronic packages.
- The temperature dependent behavior of CBGA package assembly was characterized quantitatively. The results revealed a significant nonlinear global behavior due to complete relaxation of stresses at high temperatures. The local analysis of the solder interconnection proceeded and the results indicated that large inelastic deformation was accumulated at the eutectic fillet.
- The deformation behavior of WB-PBGA package under thermal and flexural loading was characterized. The fringe patterns were similar in both cases, but the strain distributions at the solder joints were completely different.
- An apparatus based on conduction heating and cooling was developed and implemented to achieve accurate temperature profile with a higher ramp rate. A

special chamber was designed and fabricated using a high power thermoelectric cooler to achieve the desired ramp rate.

- A new specimen configuration to investigate thermomechanical behavior of solder was designed and fabricated. The deformations of solder joint were documented when subjected to a controlled temperature profile over several thermal cycles. Shear strains were obtained at the solder joint for the first five cycles.
- The shear strains at the solder joint were obtained from the finite element analysis based on the existing nonlinear constitutive properties of SnPb eutectic solder. Numerical predictions on the shear strain, the shear strain ranges and the shear strain increment at the extreme temperatures were compared with the results from the experiments.

6.2 Suggestions for Future Research

This dissertation presents two experimental setups for the extension of moiré interferometry. The first apparatus employed convection-based heating to simulate the ATC conditions, where the convectional heating/cooling with vigorous airflow around the specimen is desired to apply a uniform temperature. The setup is especially suited for determining the thermally induced deformations of the actual packages composed of diverse materials. These experimental results can be used to provide the guidelines for the modeling community.

The second apparatus is based on conduction heating and cooling to achieve a high ramp rate. A special chamber is designed and fabricated using a high power

thermoelectric cooler to achieve the desired ramp rate and more idealized temperature profile. This setup is ideal for studies on the effects of ramp rate and dwell time. The results can be extended to provide a guideline of accelerated testing conditions.

Appendix A

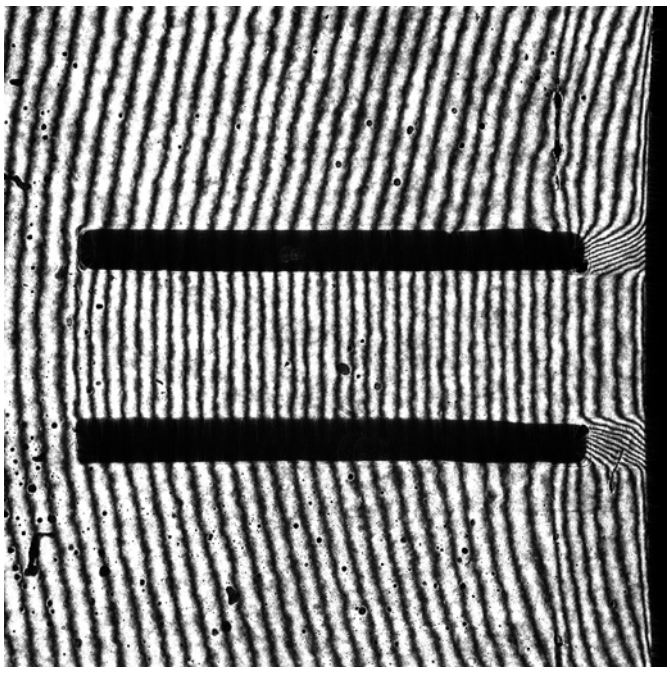

U field

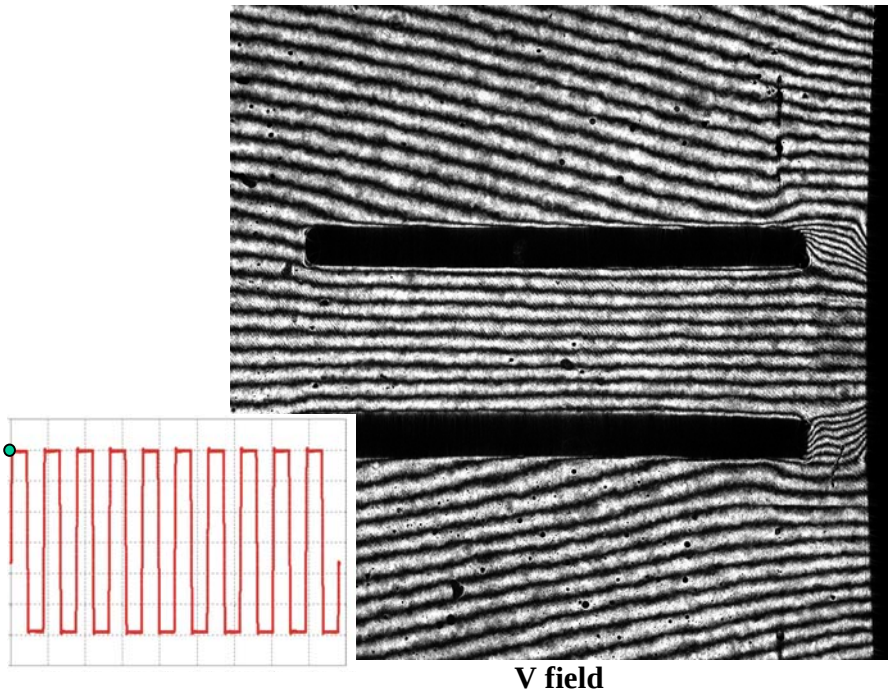

V field

Figure A-1 U and V field fringe Patterns at the start of 100 °C dwell (1st cycle)

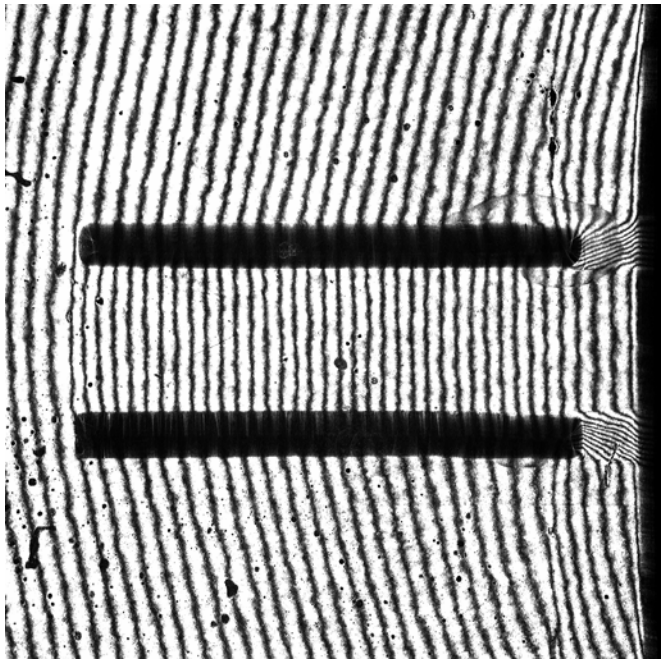

U field

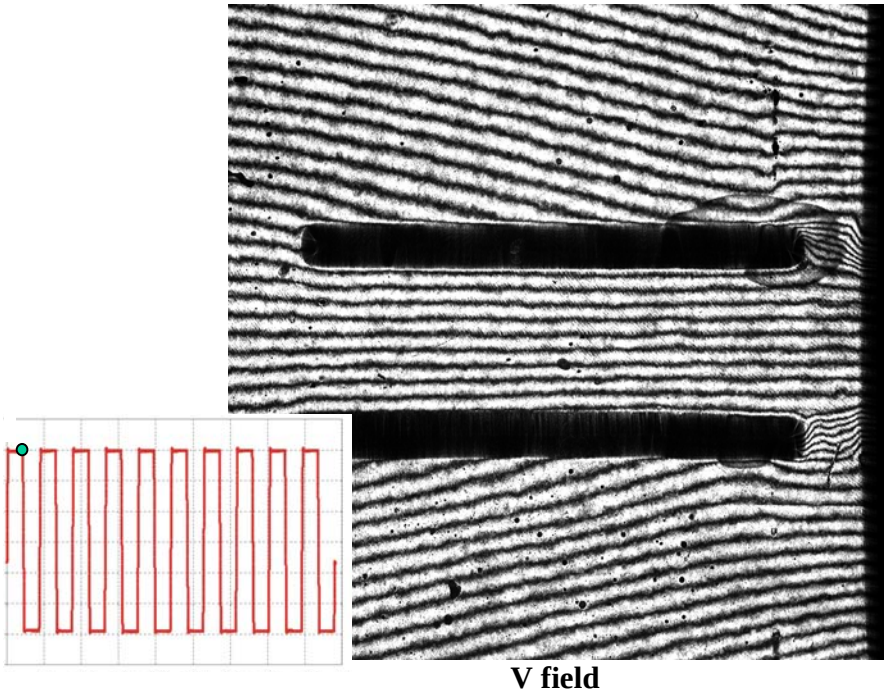

V field

Figure A-2 U and V field fringe Patterns at the end of 100 ºC dwell (1st cycle)

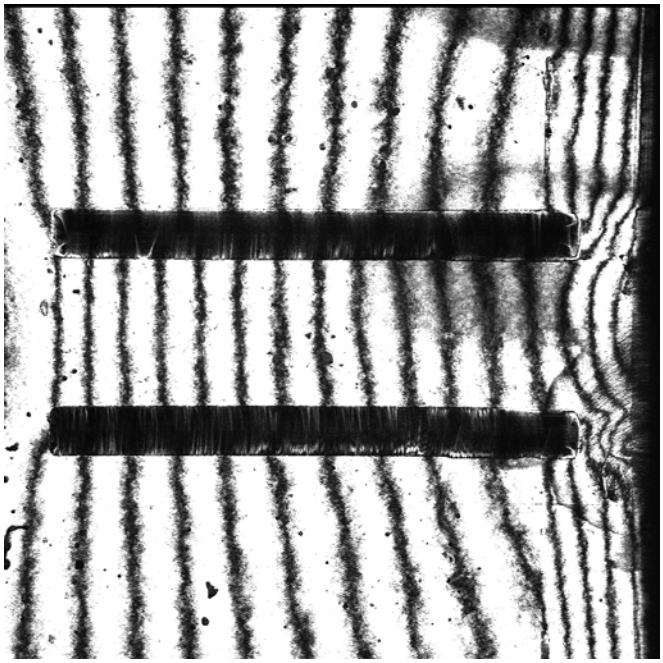

U field

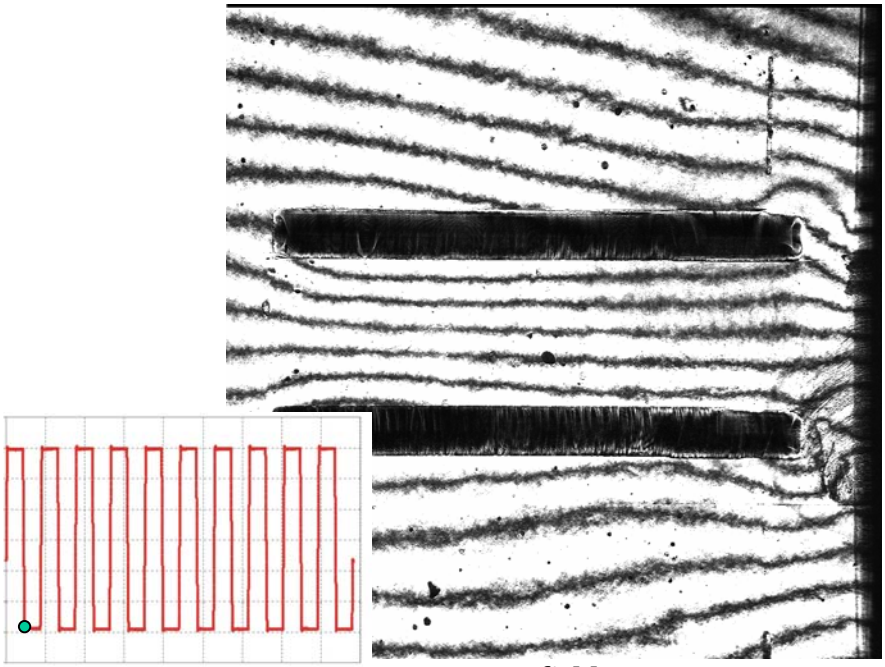

V field

Figure A-3 U and V field fringe Patterns at the start of -20 ºC dwell (1st cycle)

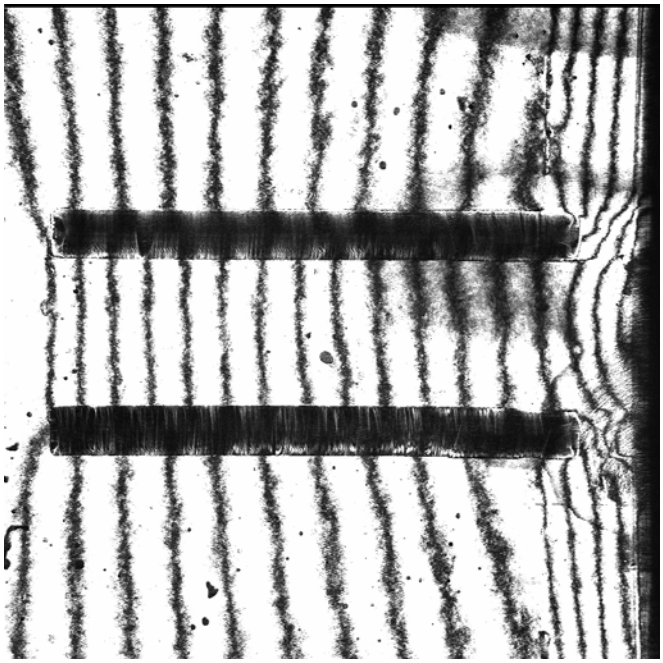

U field

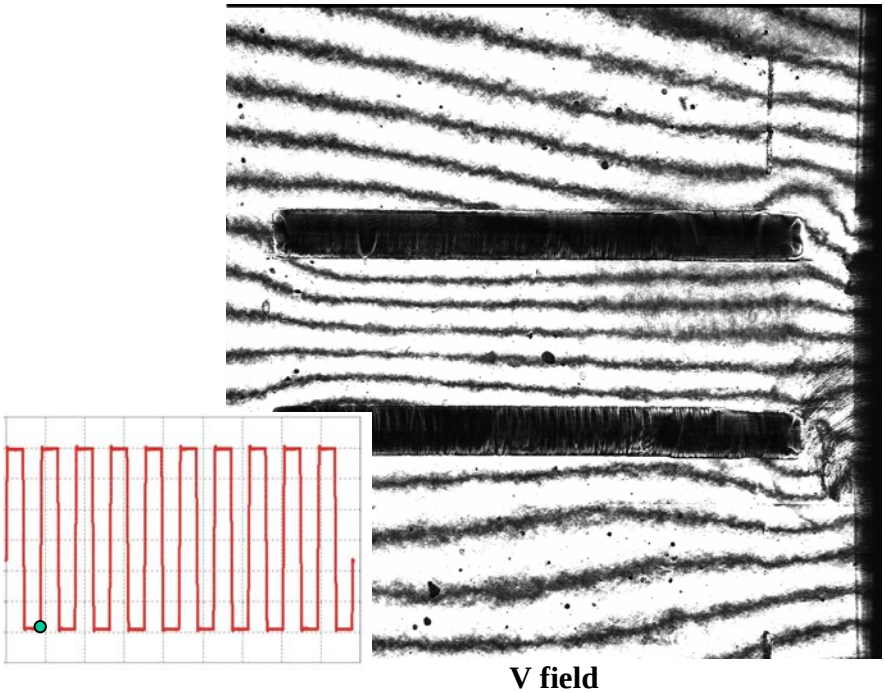

V field

Figure A-4 U and V field fringe Patterns at the end of -20 ºC dwell (1st cycle)

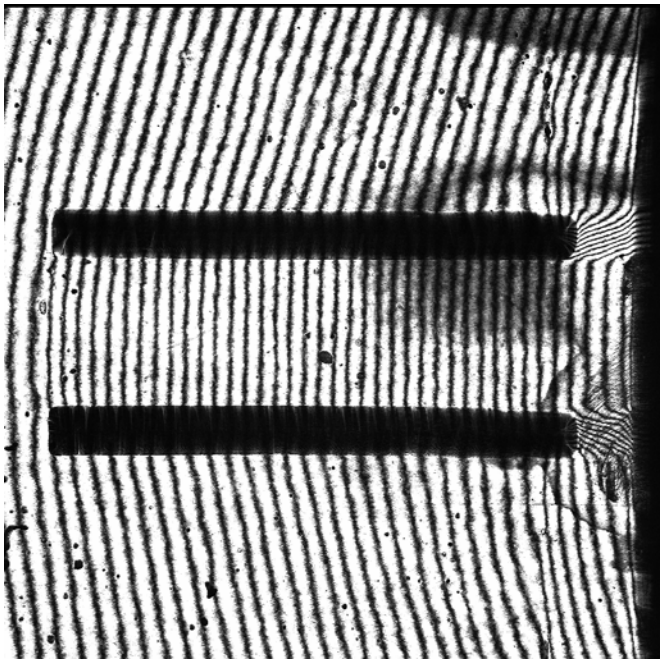

U field

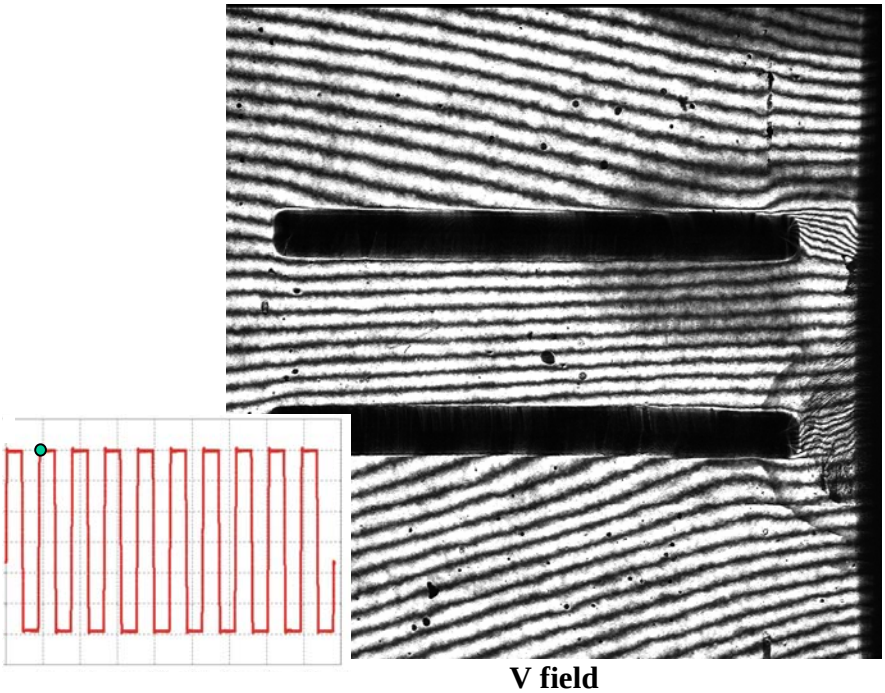

V field

Figure A-5 U and V field fringe Patterns at the start of 100 ºC dwell (2nd cycle)

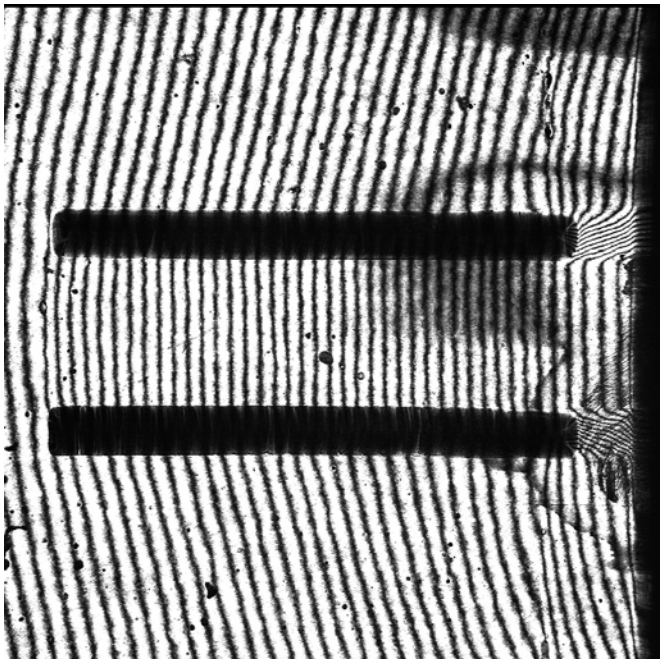

U field

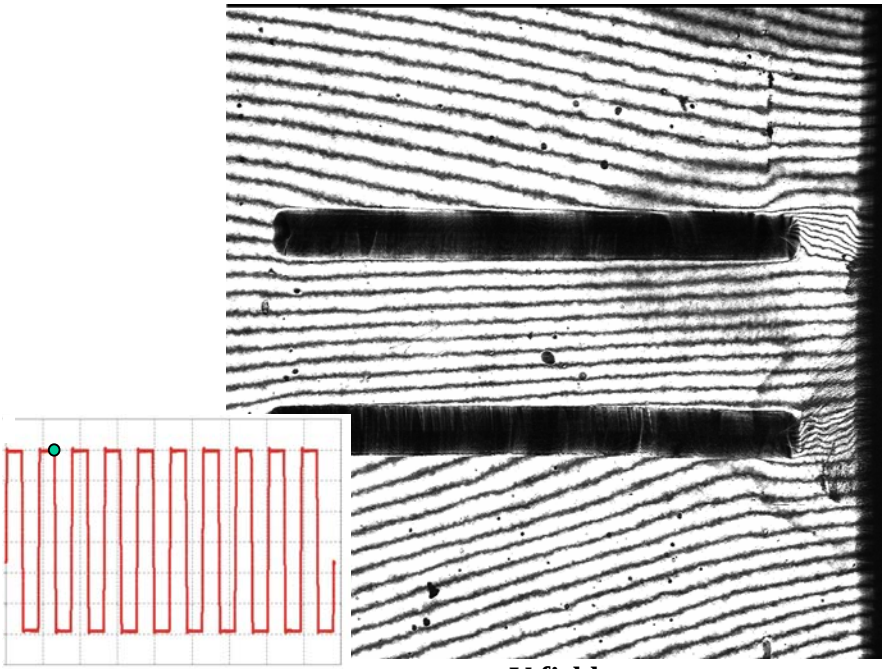

V field

Figure A-6 U and V field fringe Patterns at the end of 100 ºC dwell (2nd cycle)

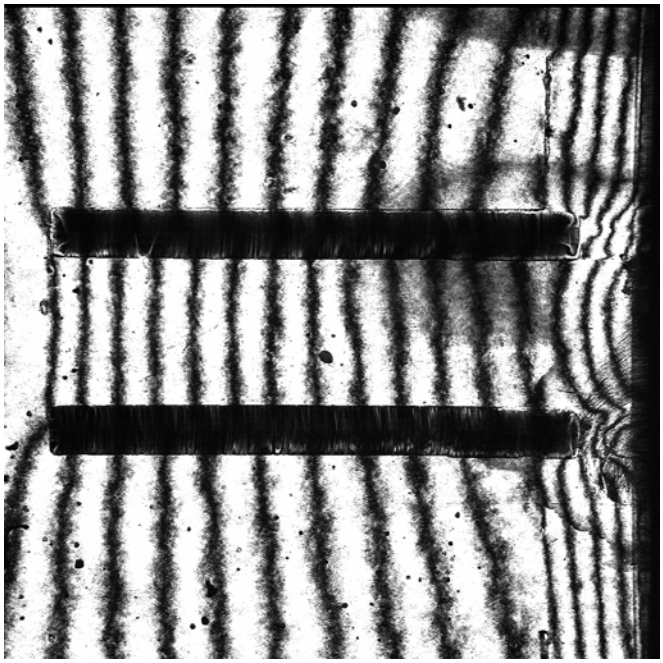

U field

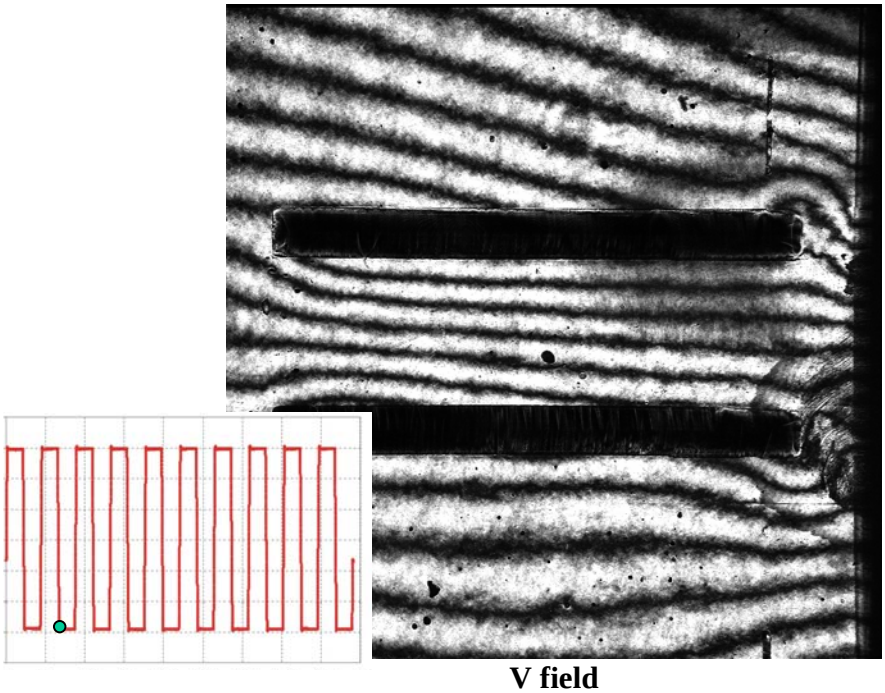

V field

Figure A-7 U and V field fringe Patterns at the start of -20 ºC dwell (2nd cycle)

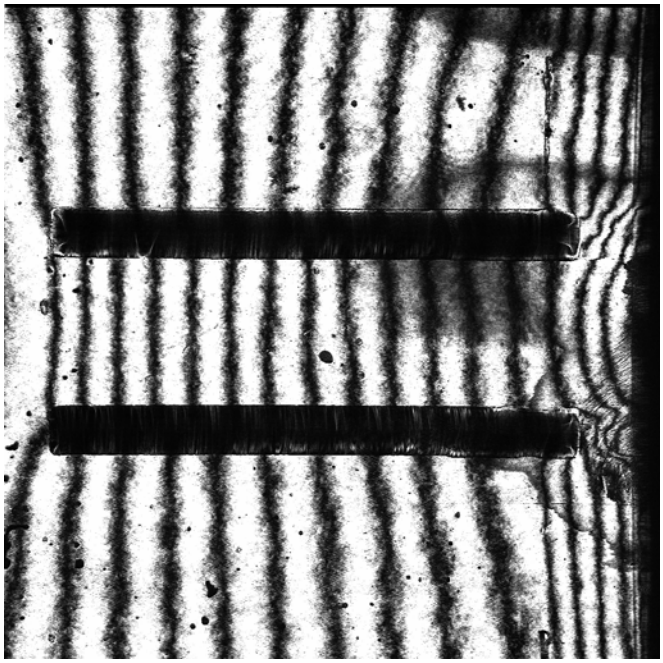

U field

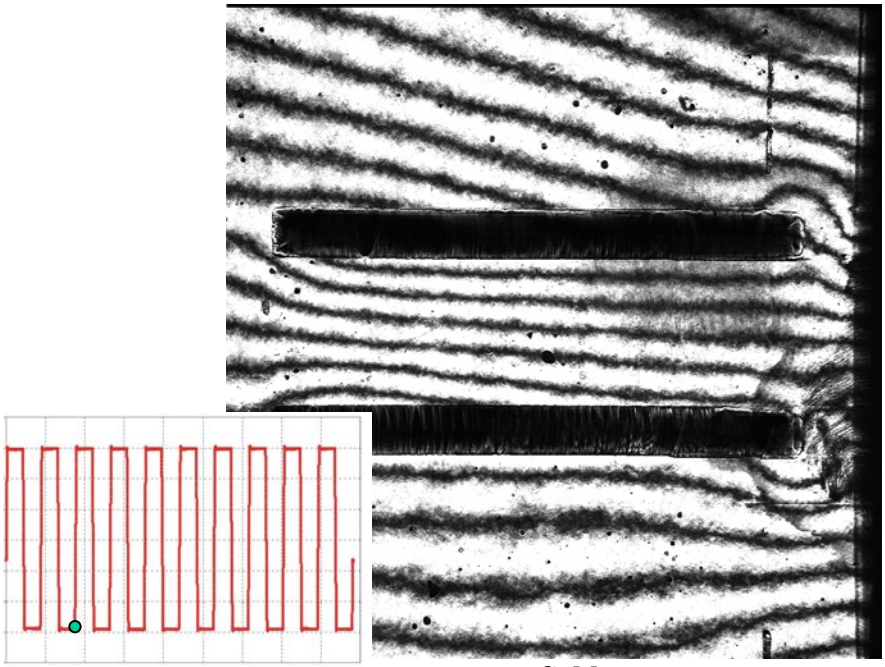

V field

Figure A-8 U and V field fringe Patterns at the end of -20 ºC dwell (2nd cycle)

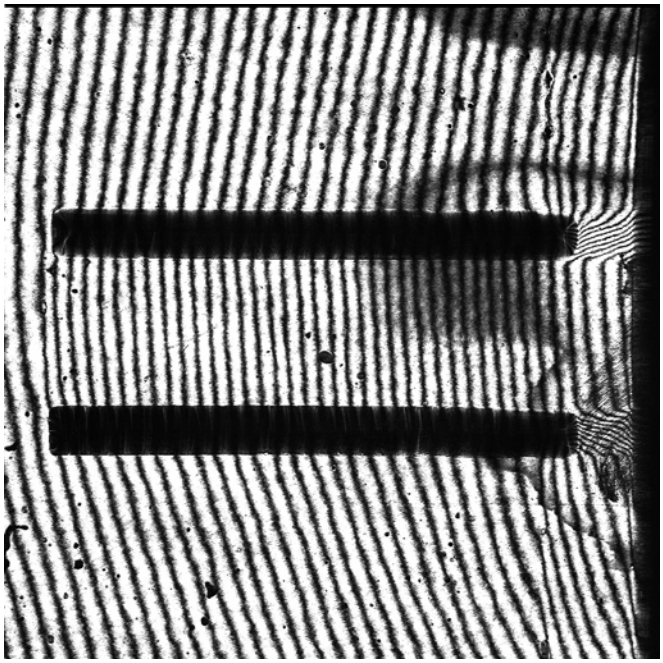

U field

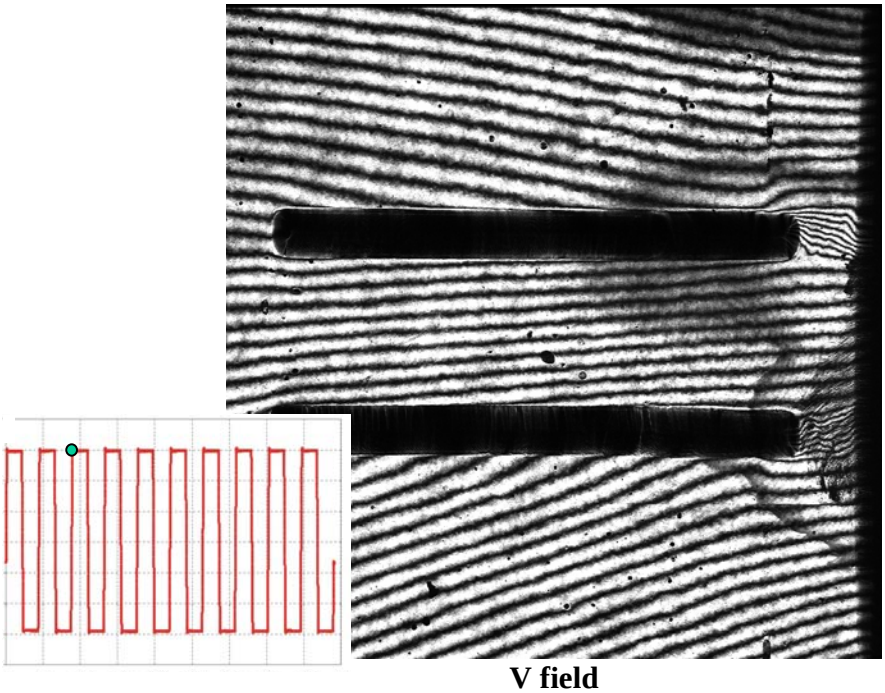

V field

Figure A-9 U and V field fringe Patterns at the start of 100 ºC dwell (3rd cycle)

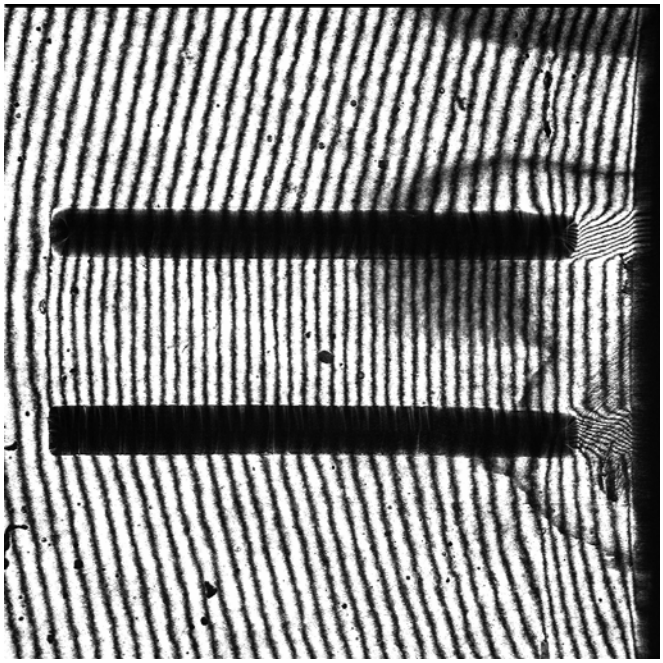

U field

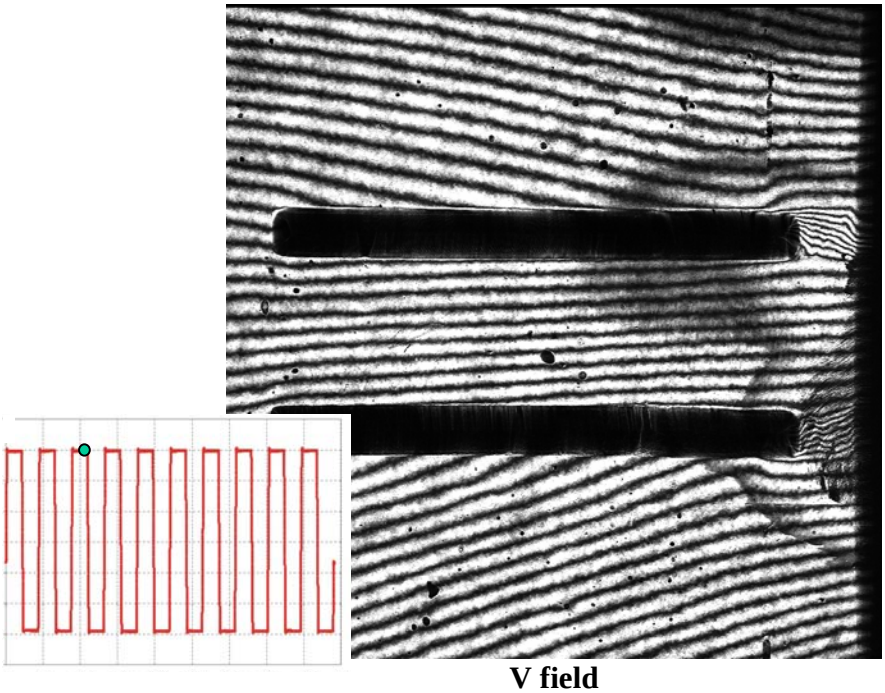

V field

Figure A-10 U and V field fringe Patterns at the end of 100 ºC dwell (3rd cycle)

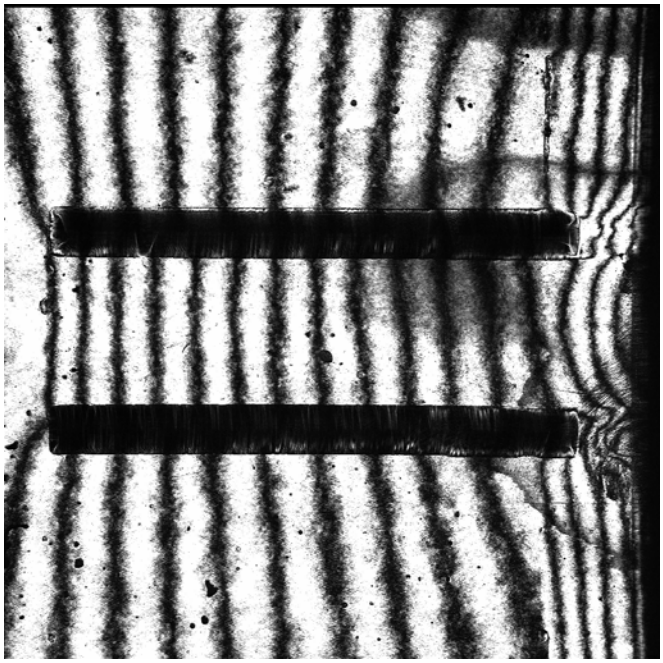

U field

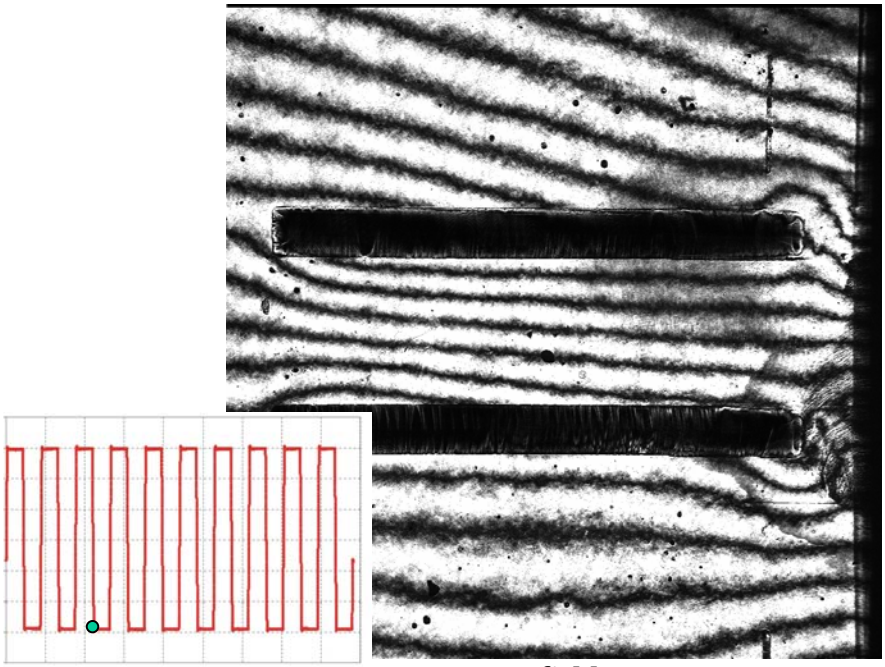

V field

Figure A-11 U and V field fringe Patterns at the start of -20 ºC dwell (3rd cycle)

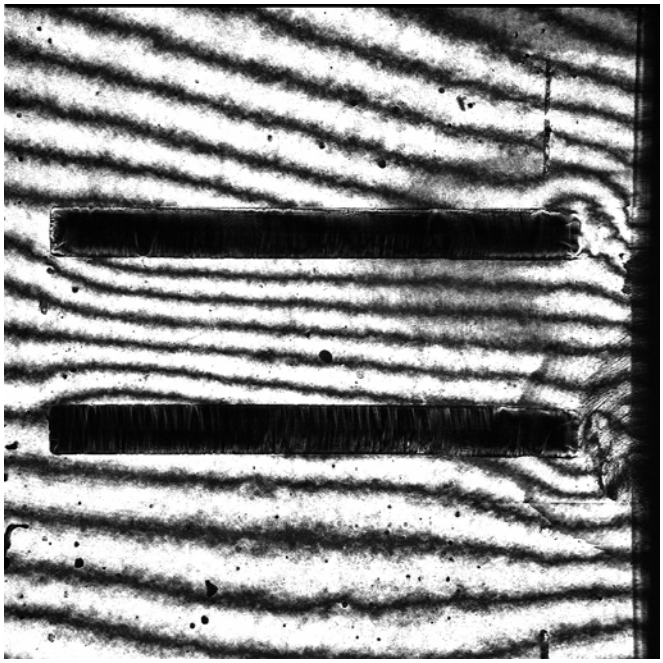

U field

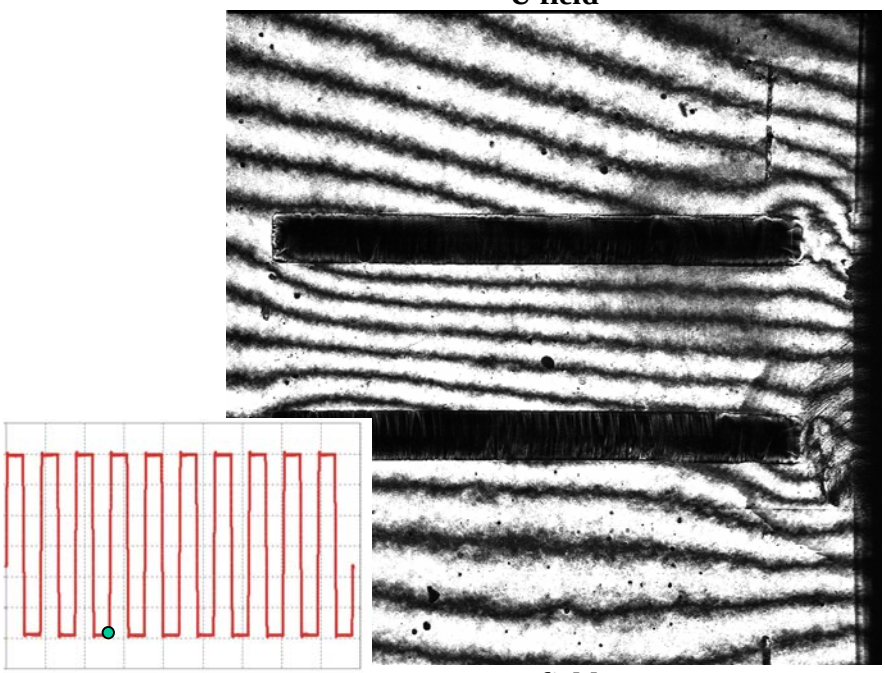

V field

Figure A-12 U and V field fringe Patterns at the end of -20 ºC dwell (3rd cycle)

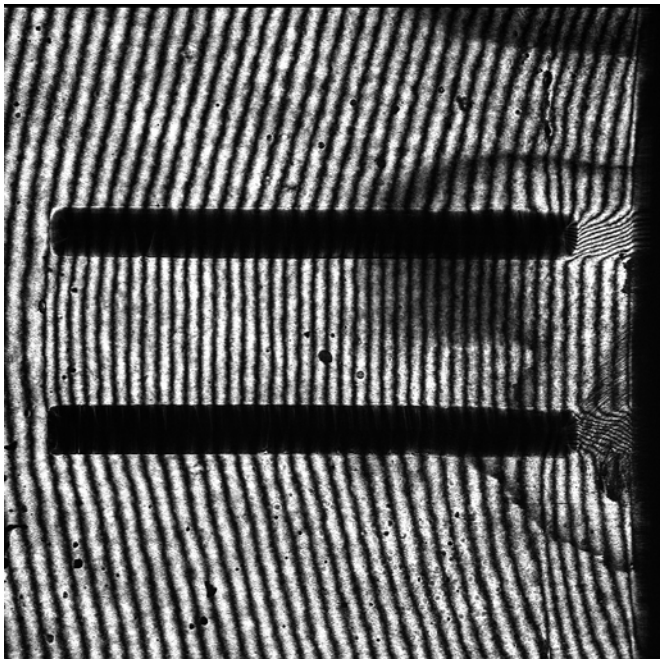

U field

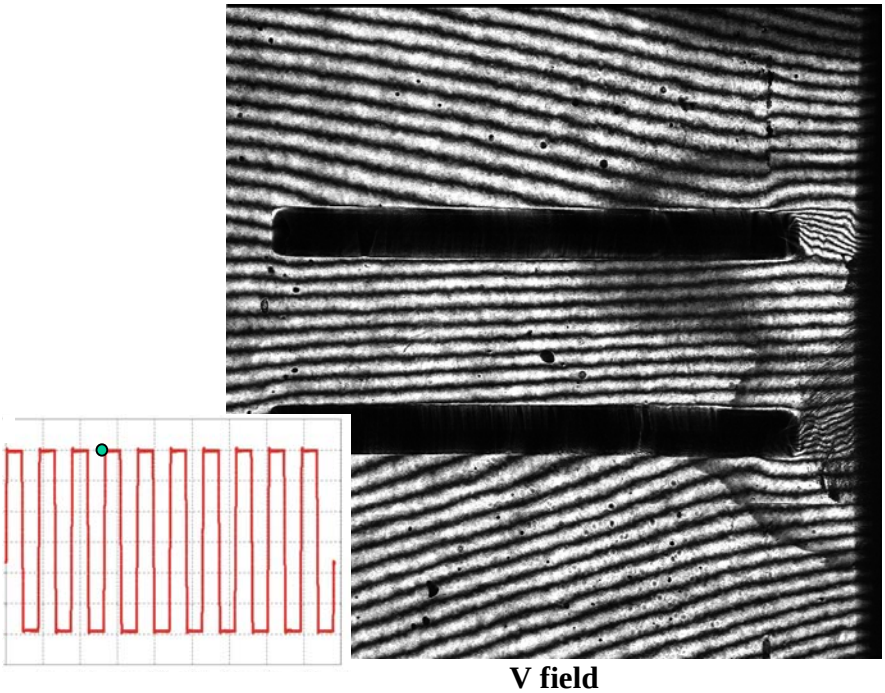

V field

Figure A-13 U and V field fringe Patterns at the start of 100 ^{o}C dwell (4th cycle)

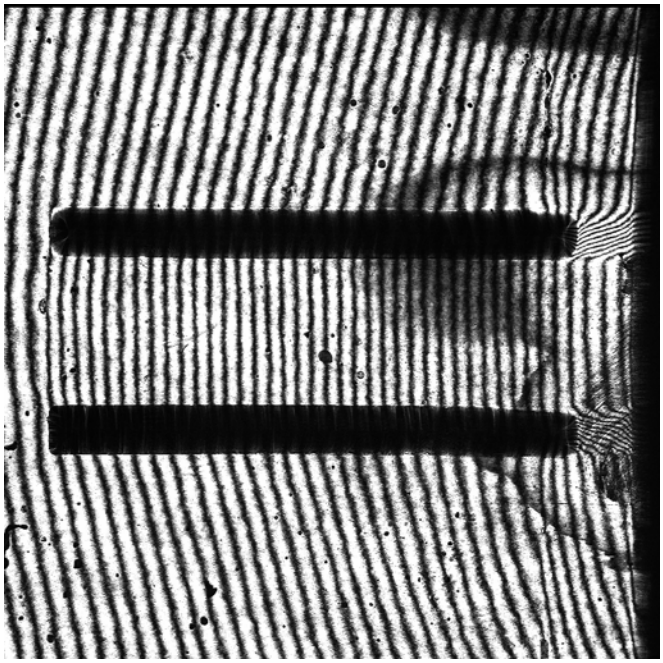

U field

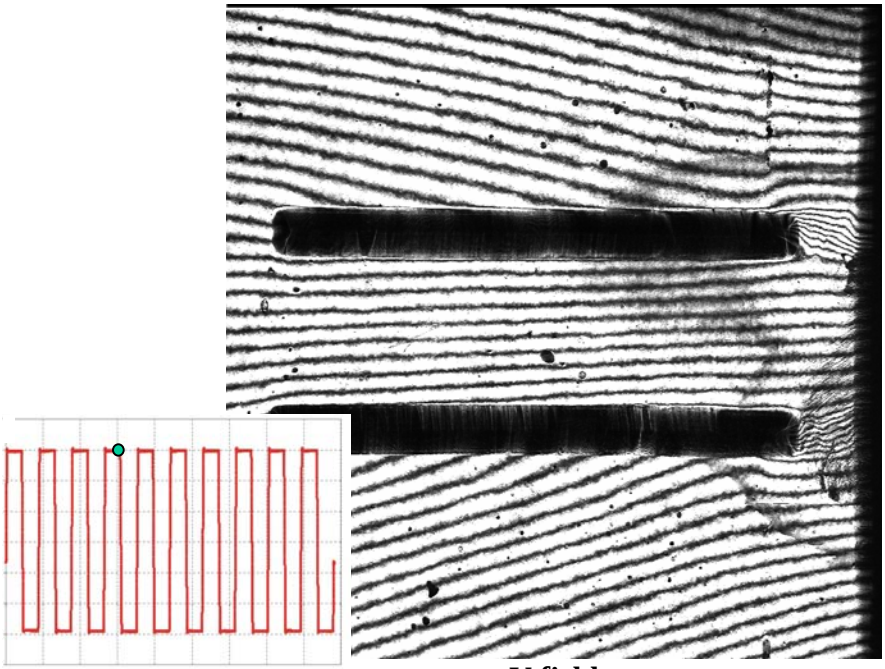

V field

Figure A-14 U and V field fringe Patterns at the end of 100 ºC dwell (4th cycle)

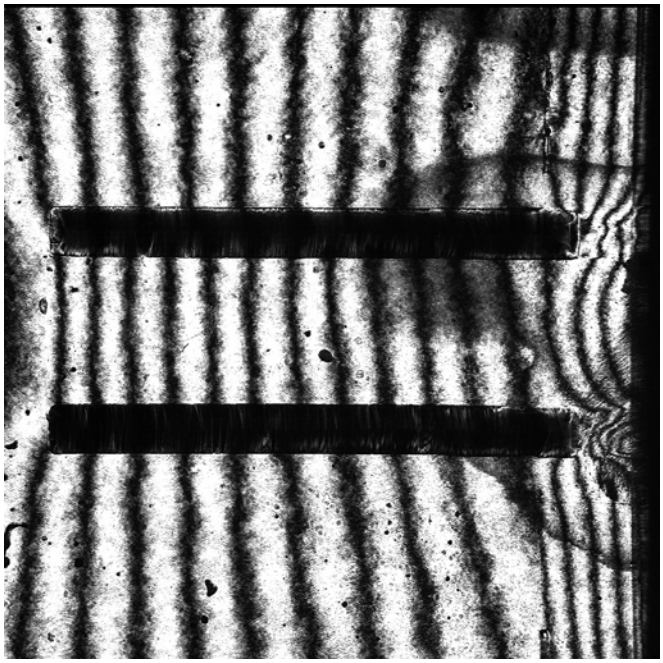

U field

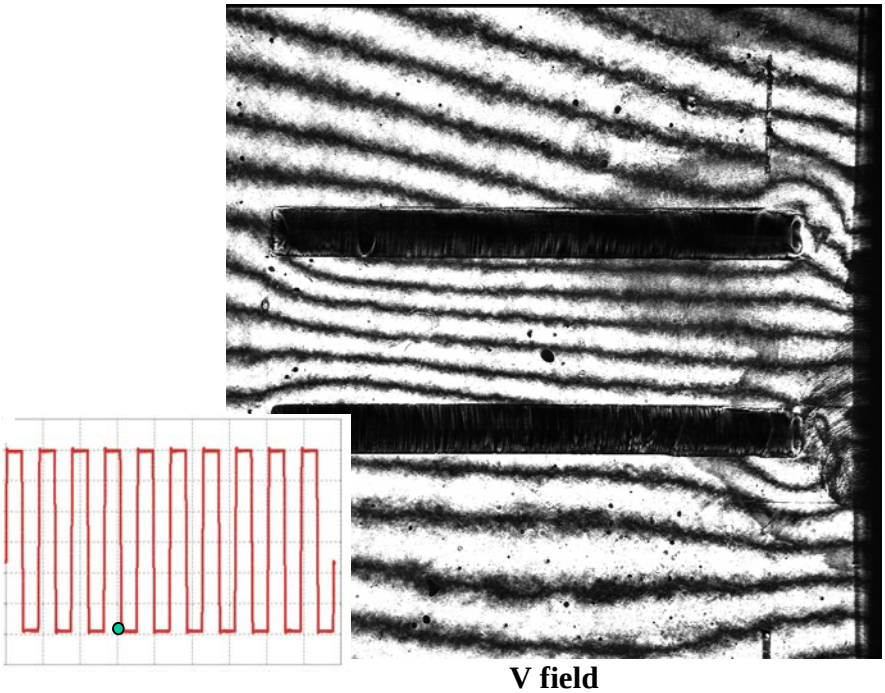

V field

Figure A-15 U and V field fringe Patterns at the start of -20 ºC dwell (4th cycle)

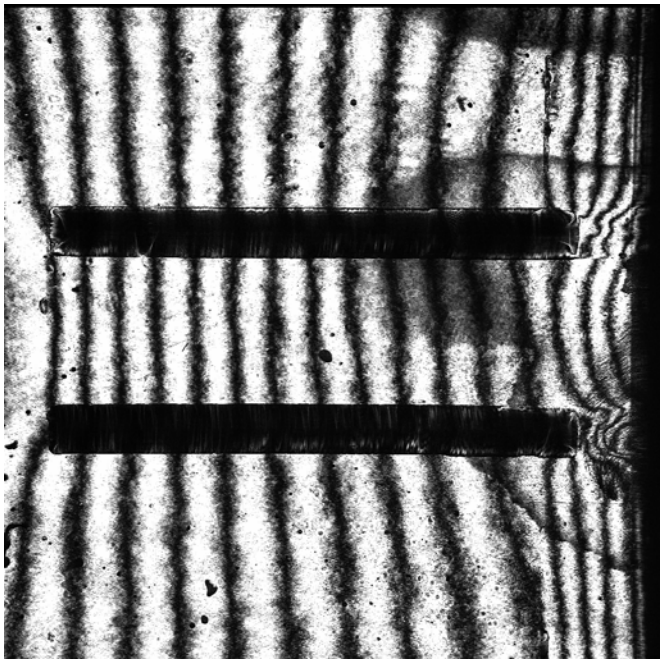

U field

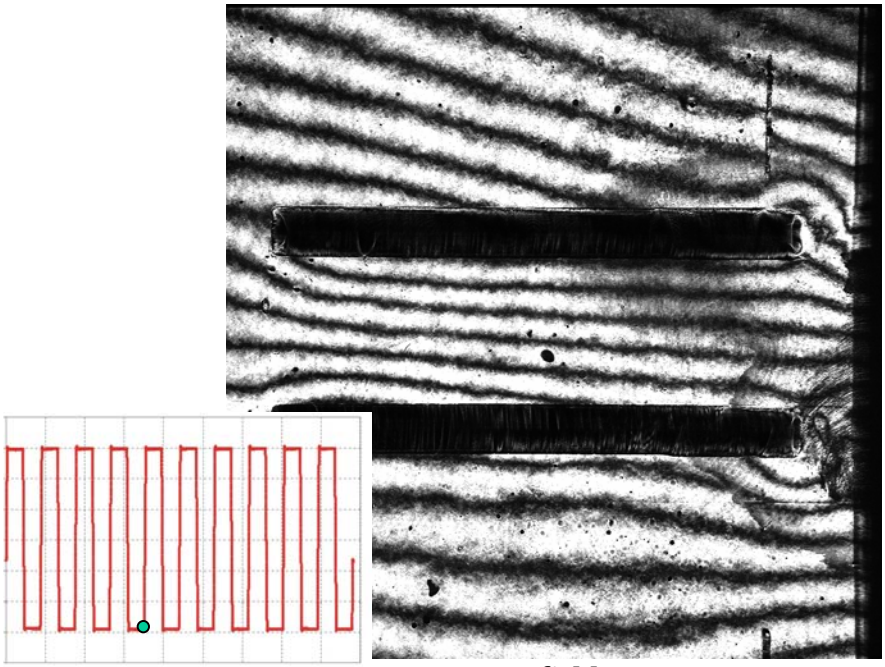

V field

Figure A-16 U and V field fringe Patterns at the end of -20 ºC dwell (4th cycle)

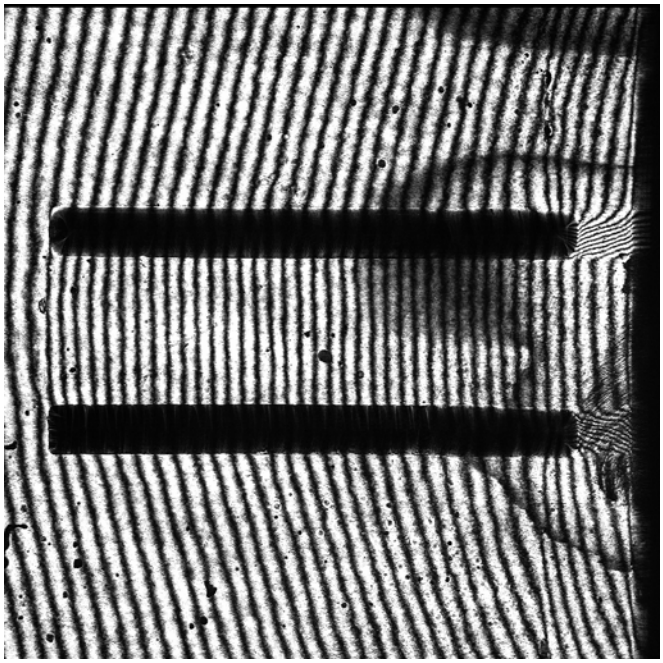

U field

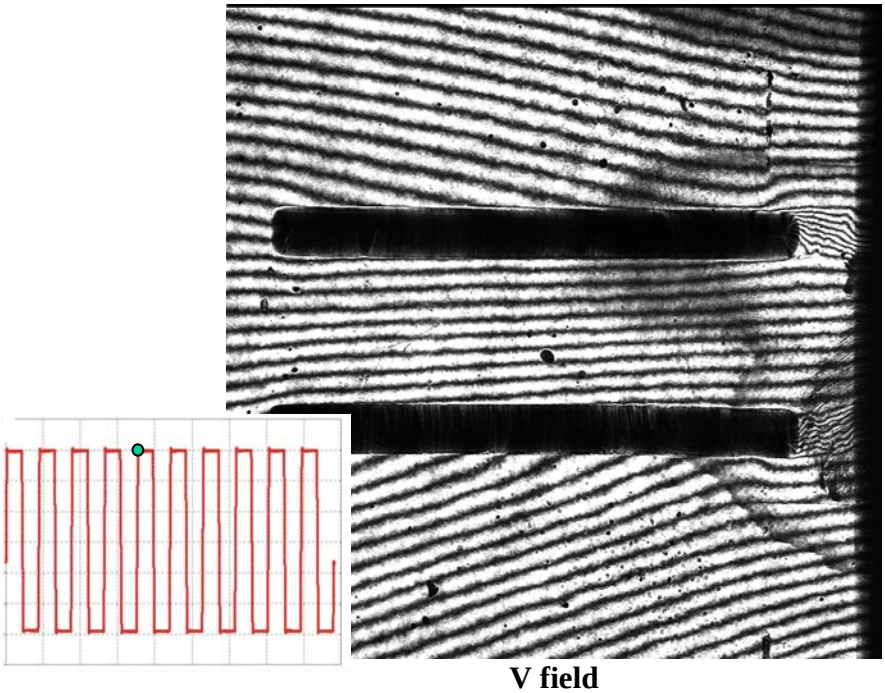

V field

Figure A-17 U and V field fringe Patterns at the start of 100 ^{o}C dwell (5th cycle)

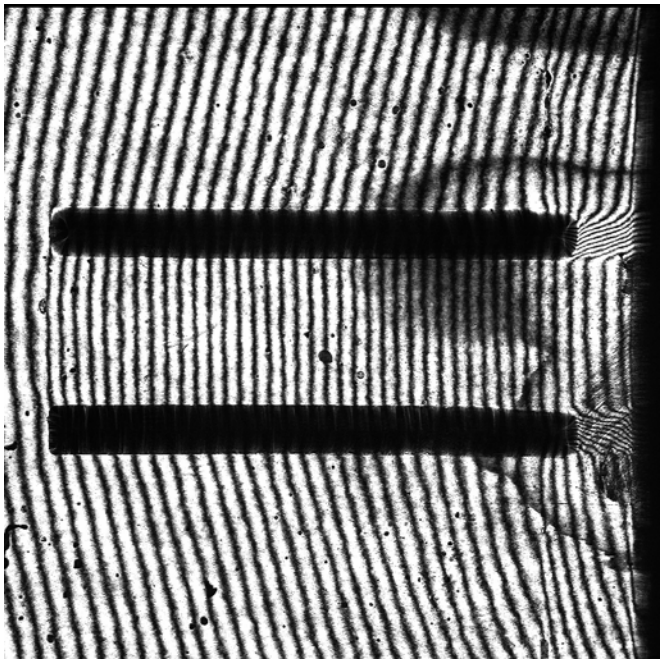

U field

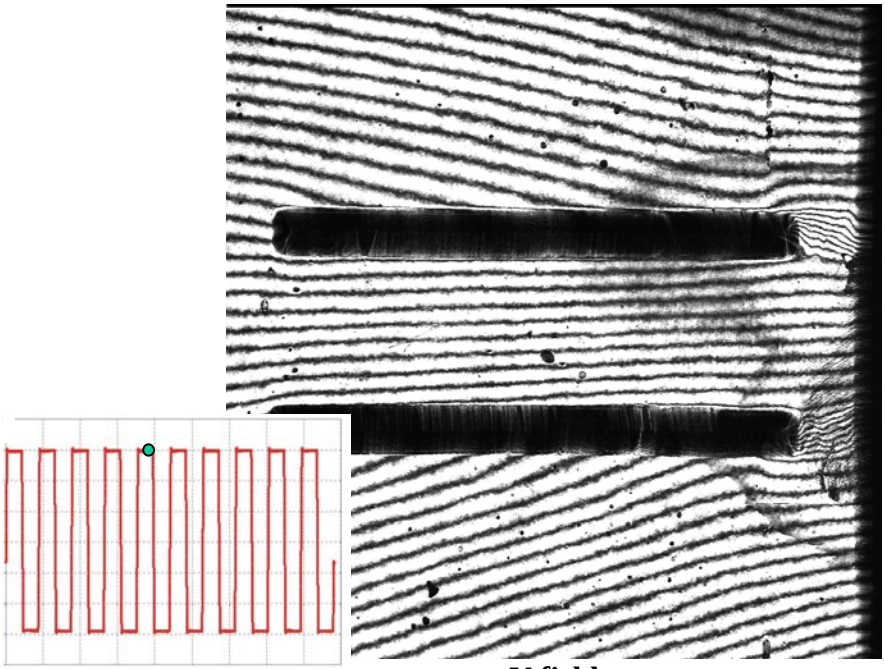

V field

Figure A-18 U and V field fringe Patterns at the end of 100 ºC dwell (5th cycle)

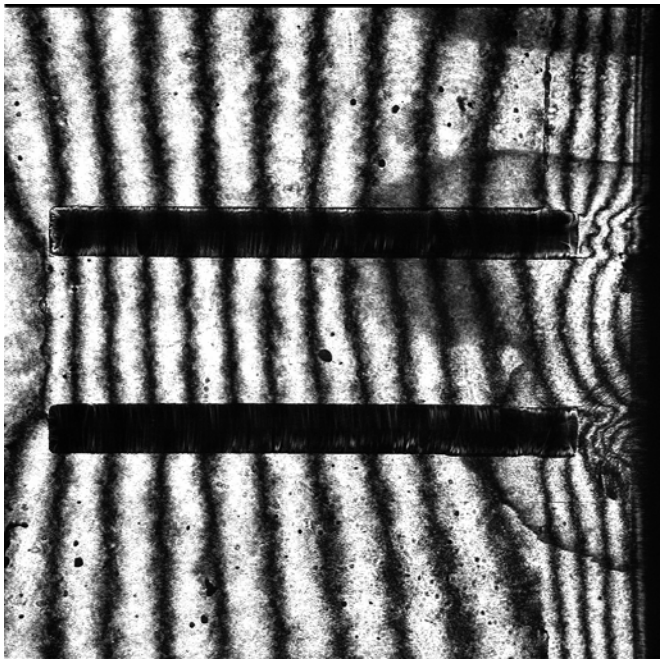

U field

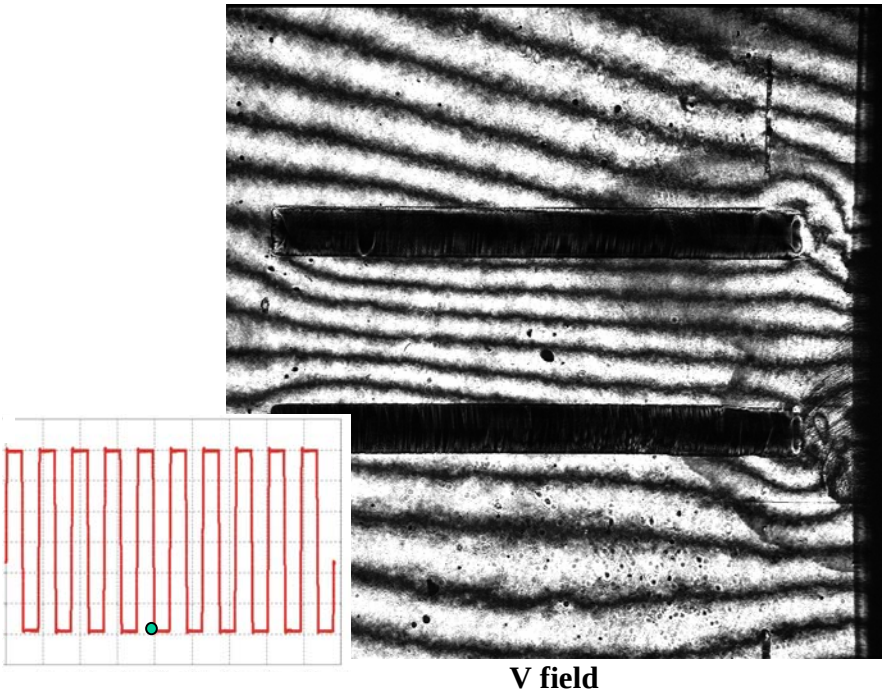

V field

Figure A-19 U and V field fringe Patterns at the start of -20 ºC dwell (5th cycle)

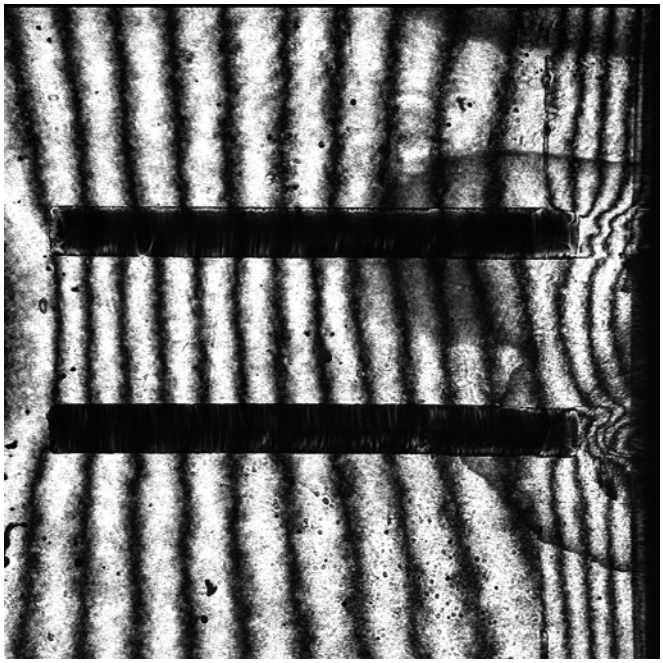

U field

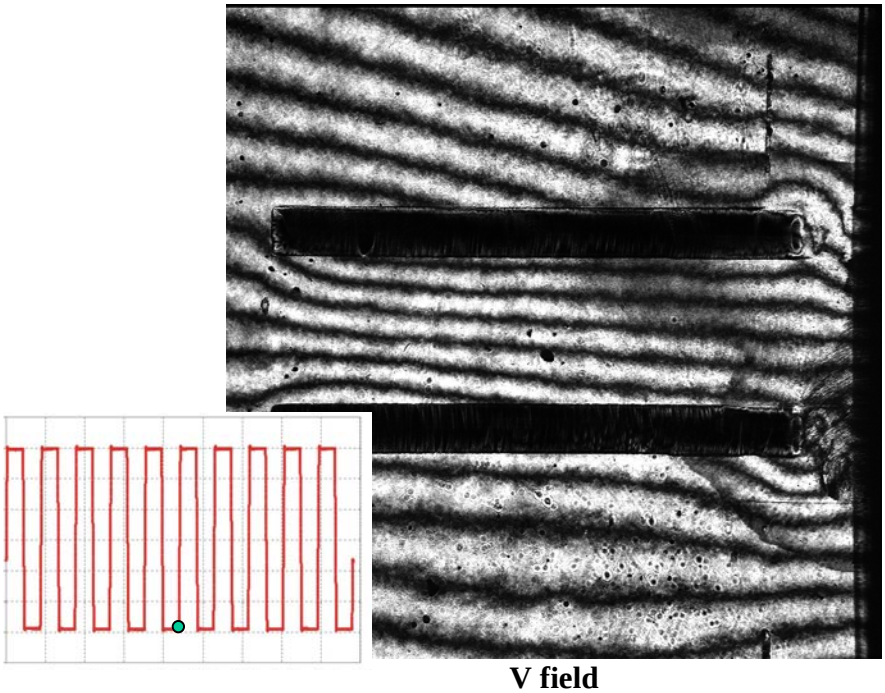

V field

Figure A-20 U and V field fringe Patterns at the end of -20 ºC dwell (5th cycle)

References

1. Hecht, E., *Optics*, 4th edition, Addison Wesley Longman, Inc., 2002
2. Darveaux, R., and Mawer, A., "Thermal and Power Cycling Limits of Plastic Ball Grid Array (PBGA)," *Proceedings of Surface Mount International*, pp. 315-325, 1995.
3. Darveaux, R., Banerji, K., Mawer, A., and Doddy, G., "Chap. 13 Reliability of Ball Grid Array Solder Joints," *Ball Grid Array Technology,* ed. J. H. Lau, McGraw-Hill, 1994.
4. Syed, A., "A Review of Finite Element Methods for Solder Joint Analysis," B. Han, R. Mahajan and D. Barker, ed., *Experimental/Numerical Mechanics in Electronics Packaging*, Vol. 1, Society for Experimental Mechanics, Bethel, CT, 1997.
5. Post, D., Han, B., and Ifju, P., *High Sensitivity Moiré: Experimental Analysis for Mechanics and Materials*, Mechanical Engineering Series, Springer-Verlag, New York, 1994.
6. Post, D., Han, B., and Ifju, P., "Moiré Interferometry for Engineering Mechanics: Current Practice and Future Development," *Journal of Strain Analysis*, Vol. 36, No. 1, pp. 101-117, 2001.
7. Hong, B.Z., Yuan, T.D., "Integrated Flow-Thermomechanical and Reliability Analysis of a Low Air Cooled Flip Chip-PBGA Package," Proceedings of Electronic Components and Technology Conference, pp. 1354-1360, 1998.
8. Mawer, A., Koschmieder, T., Popps, D., "Board Mounted Reliability Characteristics of Flip-Chip PBGA," Proceedings of 2001 SMTA International, 2001.
9. Kuang, J., Sheen, M., Hsu, Y., "The effect of residual stress on the stress distribution of an IC solder joint", Proceedings of InterPACK '99, pp. 1047-1051, 1999.
10. Darveaux, R., "Solder Joint Fatigue Life Model," Design and Reliability of Solder and Solder Interconnections, pp.213-218, 1997.
11. Pao, Y.-H., Badgley, S., Govila, R., Baumgartner, L., Allor, R., and Cooper, R. "Measurements of Mechanical Behavior of High Lead Lead-Tin Solder Joints Subjected to Thermal Cycling," *Journal of Electronic Packaging, Trans. Of ASME,* 111, pp. 135-145, 1992.

12. Pao, Y.-H., Badgley, S., Jih, E., Govila, R., and Browning, J. “Constitutive Behavior and Low Cycle Thermal Fatigue of 97Sn-3Cu Solder Joints”, *Journal of Electronic Packaging, Trans. Of ASME*, 115, pp. 147-152, 1993.
13. Upadhyayula, K., *Ph. D. Dissertation*, Dept. of Mechanical Engineering, University of Maryland, College Park, MD, 2000.
14. Bastawros, A. F., and Voloshin, A. S., "Transient Thermal Strain Measurements in Electronic Packages," *IEEE Transactions on Components, Hybrids and Manufacturing Technology*, Vol. 13, No. 4, pp. 961-966, 1990.
15. Bastawros, A. F., and Voloshin, A. S., "In Situ Calibration of Stress Chips," *IEEE Transactions on Components, Hybrids and Manufacturing Technology*, Vol. 13, No. 4, pp. 888-892, 1990.
16. Bastawros, A. F., and Voloshin, A. S., "Thermal Strain Measurements in Electronic Packages through Fractional Fringe Moiré Interferometry," *Journal of Electronic Packaging, Transaction of the ASME*, Vol. 112, No. 4, pp. 303-308, 1990.
17. Guo, Y., Chen, W. T., and Lim, C. K., "Experimental Determination of Thermal Strains in Semiconductor Packaging Using Moiré Interferometry," *Proceedings of 1992 Joint ASME/JSME Conference on Electronic Packaging*, American Society of Mechanical Engineers, New York, pp. 779-784, 1992.
18. Guo, Y., Lim, C. K., Chen, W. T., and Woychik, C. G., "Solder Ball Connect (SBC) Assemblies under Thermal Loading: I. Deformation Measurement via Moiré Interferometry, and Its Interpretation," *IBM Journal of Research and Development*, Vol. 37, No. 5, pp. 635-648, 1993.
19. Wu, T. Y., Guo, Y., and Chen, W. T., "Thermal-Mechanical Strain Characterization for Printed Wiring Boards," *IBM Journal of Research and Development*, Vol. 37, No. 5, pp. 621-634, 1993.
20. Han, B., and Guo, Y., "Thermal Deformation Analysis of Various Electronic Packaging Products by Moiré and Microscopic Moiré Interferometry," *Journal of Electronic Packaging, Transaction of the ASME*, Vol. 117, pp. 185-191, 1995.
21. Han, B., Guo, Y., Lim, C.K., and Caletka, D., "Verification of Numerical Models Used in Microelectronics Packaging Design by Interferometric Displacement

Measurement Methods," *Journal of Electronic Packaging, Transaction of the ASME*, Vol. 118, pp. 157-163, 1996.

22. Han, B., Guo, Y., Lim, C. K., and Caletka, D., "Verification of Numerical Models Used in Microelectronics Packaging Design by Interferometric Displacement Measurement Methods," *Journal of Electronic Packaging, Transaction of the ASME*, Vol. 118, pp. 157-163, 1996.
23. Han, B., and Guo, Y., "Determination of Effective Coefficient of Thermal Expansion of Electronic Packaging Components: A Whole-field Approach," *IEEE Transactions on Components, Packaging and Manufacturing Technology-Part A*, Vol. 19, No. 2, pp. 240-247, 1996.
24. Tsao, P. H., and Voloshin, A. S., "Manufacturing Stresses in the Die due to Die-Attach Process," *IEEE Transactions on Components, Packaging and Manufacturing Technology - Part A*, Vol. 18, No. 1, pp. 201-205, 1995.
25. Han, B., Chopra, M., Park, S., Li, L., and Verma, K., "Effect of Substrate CTE on Solder Ball Reliability of Flip-Chip PBGA Package Assembly," *Journal of Surface Mount Technology*, Vol. 9., pp. 43-52, 1996.
26. Han, B., "Deformation Mechanism of Two-Phase Solder Column Interconnections under Highly Accelerated Thermal Cycling Condition: An Experimental Study," *Journal of Electronic Packaging, Transaction of the ASME*, Vol. 119, pp. 189-196, 1997.
27. Han, B., and Guo, Y., "Photomechanics Tools as Applied to Electronic Packaging Product Development," B. Han, R. Mahajan and D. Barker, ed., *Experimental/Numerical Mechanics in Electronics Packaging*, Vol. 1, Society for Experimental Mechanics, Bethel, CT, 1997.
28. Han, B., "Recent Advancement of Moiré and Microscopic Moiré Interferometry for Thermal Deformation Analyses of Microelectronics Devices," *Experimental Mechanics*, Vol. 38, No. 4, pp. 278-288, 1998.
29. Zhao, J.-H., Dai, X., and Ho, P. S., "Analysis and Modeling Verification for Thermal-mechanical Deformation in Flip-Chip Packages," *Proceedings of 48th Electronic Components and Technology Conference*, May 25-28, Seattle, WA, pp. 336-344, 1998.

30. Ham, S. and Lee, S., " Measurement of Creep and Relaxation Behaviors of Wafer-Level CSP Assembly Using Moiré Interferometry," *Journal of Electronic Packaging, Transaction of the ASME*, Vol. 125, No. 2, pp. 282-288, 2003.
31. Wang, J.,Qian, Z., Zou, D.; and Liu, S., "Creep behavior of a flip-chip package by both FEM modeling and real time moiré interferometry," Proceedings of *48th Electronic Components and Technology Conference*, IEEE, New York, pp. 1438 – 1445, 1998.
32. Wang, J., Ren, W., Zou, D., and Liu, S., "Effect of cleaning and non-cleaning situations on the reliability of flip-chip packages", *IEEE Transactions on Components, Packaging and Manufacturing Technology-Part A*, Vol. 22, No. 2, pp. 221-228, 1999.
33. Voloshin, A. S., Tsao, P. H., and Pearson, R. A., "In situ Evaluation of Residual Stresses in an Organic Die-Attach Adhesive," *Journal of Electronic Packaging, Transaction of the ASME*, Vol. 120, No. 3, pp. 314-318, 1998.
34. Calce Internal Report, "Thermal-mechanical Fatigue Modeling Using ANSYS", 2003.
35. Skipor, A. F., Harren, S. V., and Botsis, J., "On the Constitutive Response of 63/37 Sn/Pb Eutectic Solder," Journal of Engineering Materials and Technology, Vol. 118, p. 1-11, 1996
36. Dasgupta, A., Clark, D., Darbha, K., Haswell, P., Okura, J., Ray, C. and Shetty, S., "Creep Constitutive Properties Literature Survey", CALCE internal report, 1999.
37. Feustel, F., Wiese, S., and Meusel, E., " Time-Dependent material Modeling for Finite Element Analyses of Flip Chips", Proceedings of *50th Electronic Components and Technology Conference*, IEEE, New York, pp. 1548 – 1553, 2000.
38. Han, B. and Kunthong, P., "Micro-mechanical Deformation Analysis of Surface Laminar Circuit in Organic Flip-chip Package: An Experimental Study," *Journal of Electronic Packaging, Transaction of the ASME*, Vol. 122, No. 3, pp. 294-300, 2000.
39. Caulfield, T., Cole, M. S., Cappo, F., Zitz, J and Benenati, J., "An Overview of Ceramic Ball and Column Grid Array Packaging" in *Ball Grid Array Technology*, ed. J. Lau, McGraw-Hill, New York, NY, Chap. 5, pp. 131-169, 1995.
40. Caulfield T., Benenati, J. A. and Acocella, J, "Surface Mount Array Interconnections for High I/O MCM-C to Card Assemblies," *Proceedings of 1993 ISHM/MCM*, pp. 320-325, 1993.

41. Corbin, J. S., "Finite Element Analysis for Solder Ball Connect (SBC) Structural Design Optimization," *IBM Journal of Research and Development*, Vol. 37, No. 5, pp. 585-596, 1993.
42. Darveaux, R. “Solder joint fatigue life model,” *Proceedings of 1997 TMS Annual Meeting*, pp. 213–218,1997.
43. Wang, G.Z., Cheng, Z.N., Becker, K., and Wilde, J., “Applying Anand Model to Represent the Viscoplastic Deformation Behavior of Solder Alloys”, *Journal of Electronic Packaging, Transaction of the ASME*, Vol. 123, No. 3, pp. 247-253, 2001.
44. Cheng, Z.N., Cheng, Z.N., Chen, L., Wilde, J., and Becker, K., “Viscoplastic Anand Model for Solder Alloys and Its Application”, *Soldering and Surface Mount Technology*, Vol. 12, No. 2, pp. 31-36, 2000.
45. Ye, H., Lin, M., and Basaran, C., “Failure Modes and FEM analysis of power electronic packaging,” *Finite Elements in Analysis and Design*, Vol. 38, Issue 7, 601-612, 2002.
46. Raghunathan, R., Pucha, R. V., and Sitaraman, S. K., "Thermal Cycling Guidelines for Automotive, Computer, Portable, and Implantable Medical Device Applications," 12th Symposium on Mechanics of SMT and Photonic Structures, Packaging of Electronic and Photonic Devices, ASME IMECE, EEP-Vol. 28, pp. 51-62, 2000.
47. Hall, P.M., “Forces, Moments, and Displacements During Thermal Chamber Cycling of Leadless Ceramic Chip Carriers Soldered to Printed Boards,” IEEE transactions on Components, Hybrids, and Manufacturing Technology, Dec., Vol. 7, No.4, pp. 314-327, 1984.
48. Chanchani, R., Hall, P.M., “Temperature Dependence of Thermal Expansion of Ceramics and Metals for Electronic Packages”, IEEE Transactions of components, Hybrids, and Manufacturing Technology, Vol. 13, No. 4, pp. 743-750, 1990.
49. Wood, J.D., “Determination of Thermal Strains in a Bimaterial Joints,” Ph.D. Dissertation, Virginia Polytechnic Institute and State University, Blacksburg, VA, 1992.
50. Frear, D., Grivas, D., Morris, J.W., “A Microstructural Study of the Thermal Fatigue Failures of 60Sn-40Pb Solder Joints,” Journal of Electronic Materials, Vol. 17, No. 2, pp. 171-180, 1988.

51. Frear, D., Grivas, D., Morris, J.W., “Parameters Affecting Thermal Fatigue of 60Sn-40Pb Solder Joints,” Journal of Electronic Materials, Vol. 18, No. 6, pp.670-680, 1989.
52. Norris, K. C., and Landzberg, A. H., "Reliability of Controlled Collapse Interconnections," *IBM Journal of Research and Development*, Vol. 13, No. 3, pp. 266-271, 1969.
53. Lin, P., Lee, J., and Im, S., "Design Considerations for a Flip-Chip Joining Technique," *Solid State Technology*, pp. 48-54, 1970.
54. Engelmaier, W., “Fatigue Life of Leadless Chip Carrier Solder Joints During Power Cycling,” *IEEE Transactions on Parts, Hybrids and Packaging*, pp. 232-237, 1983.
55. Verma, K., Han, B., Park, S.-B. and Ackerman, W., “On the Design Parameters of Flip-chip PBGA Package Assembly for Optimum Solder Ball Reliability,” *IEEE Transactions on Components, Packaging and Manufacturing Technology-Part A*, Vol. 24, No. 2, pp. 300-307, 2001.
56. Han, B., Caletka, D., and Guo, Y., "On the Effect of Moiré Specimen Preparation on Solder Ball Strains of Ball Grid Array Package Assembly," *Proceedings of the 1995 SEM Spring Conference on Experimental Mechanics*, Grand Rapid, MI (June 1995).
57. Liu, X. and Plumbridge, W, “Thermomechanical Fatigue of Sn-37 wt.% Pb Model Solder Joints,” *Material Science and Engineering A362*, pp. 309-321, 2003
58. Wang, Z., “Development and Application of Computer-Aided Fringe Analysis”, Ph.D thesis, University of Maryland, MD, College Park, 2003.
59. Dudek, R., Vogel, D., and Michel, B.“Mechanical failure in COB Technology Using Glob-top Encapsulation,” *IEEE Transactions on Components, Packaging and Manufacturing Technology-Part A*, vol. 19, no. 4, pp. 232–240, 1996.
60. Dudek, R., Scherzer, M., Schubert, A., and Michel, B. “FE-Simulation for Polymeric Packaging Materials,” *IEEE Transactions on Components, Packaging and Manufacturing Technology-Part A*, vol. 21, no. 2, pp. 301–309, 1998.
61. Stewart, J., *The Welder’s Handbook*, Reston Publishing Company, Inc., 1981.
62. Frear, D.R., Jones, W.B., Kinsman, K.R., ed., *Solder Mechanics – A State of the Art Assessment*, Santa Fe, New Mexico, 1990.

63. Frear, D., Grivas, D., Morris, J.W., "A Microsturctural Study of the Thermal Fatigue Failures of 60Sn-40 Pb Solder Joints", Journal of Electronic Materials, Vol. 17, No. 2, pp. 171-180, 1988.
64. Frear, D., Grivas, D., Morris, J.W., "Parameters Affecting Thermal Fatigue Behavior of 60Sn-40 Pb Solder Joints", Journal of Electronic Materials, Vol. 18, No. 6, pp. 671-680, 1989.
65. Dishongh, T., Basaran, C., Cartwright, A., "Impact of Temperature Cycle Profile on Fatigue Life of Solder Joints", *IEEE Transactions on Advanced Packaging*, Vol. 25, No. 3, pp. 433-438, 2002.
66. Liu, H., Basaran, C., Cartwright, A., and Casey, W., "Application of Moiré Interferometry to Determine Strain Fields and Debonding of Solder Joints in BGA Packages", *IEEE Transactions on Advanced Packaging*, Vol. 27, No. 1, pp. 217-223, 2004.
67. Knecht, S., Fox, L., "Constitutive Relation and Creep-Fatigue Life Model for Eutectic Tin-lead Solder", *IEEE Transactions on Components, Packaging and Manufacturing Technology-Part A*, Vol. 13, No. 2, pp. 424-433, 1990.
68. Lau, J., Rice, D., and Avery, P., "Elastoplastic Analysis of Surface-Mount Solder Joints*", IEEE Transactions on Component, Hybrids, and Manufacturing Technology*, Vol. 10, No. 3, pp. 346-357, 1987.
69. Lau, J. and Pao, Y., *Solder Joint Reliability of BGA, CSP, Flip Chip and Fine Pitch SMT Assemblies*, McGraw-Hill, New York, 1997.
70. Anand, L. "Constitutive Equations for the Rate-Dependent Deformation of Metals at Elevated Temperatures," *ASME Journal of Engineering Material Technology,* Vol. 104, pp. 12-17, 1982.
71. Pecht, M., *Handbook of Electronic Package Design*, Marcel Dekker, Inc., New York, 1991.
72. Madenci, E., Guven, I. and Kilic, B., *Fatigue Life Predictions of Solder Joints in Electronic Packages with Ansys*, Kluwer Academic Publishers, 2003
73. Pollack, D., "Validity Of Constitutive Properties Of Anand Model As Applied To Thermo-Mechanical Deformation Analysis Of Eutectic Solder", M.S. thesis, University of Maryland, MD, College Park, 2003.

74. Haswell, P., “Durability Assessment And Microstructural Observations Of Selected Solder Alloys”, Ph. D. thesis, University of Maryland, MD, College Park, 2001.
75. Figliola, R. S., and Beasley, D. E., Chap 5 Uncertainty Analysis, *Theory and Design for Mechanical Measurement* 2nd Edition, John Wiley & Sons, Inc., New York, 1995.
76. Han, B., Wu, Z., and Cho, S., “Measurement of Thermal Expansion Coefficient of Flexible Substrate by Moiré Interferometry,” *Experimental Techniques*, Vol. 25, No. 3, pp. 22-25, 2001.